Università degli Studi di Napoli Federico II

Ph.D. Thesis
in
Information Technology and Electrical Engineering

Arrayed Waveguide Grating-based Interrogation System for Safety Applications and High-Speed Measurements

Vincenzo Romano Marrazzo

Tutor: Prof. Giovanni Breglio

Coordinator: Prof. Daniele Riccio

XXXIII Ciclo

Scuola Politecnica e delle Scienze di Base
Dipartimento di Ingegneria Elettrica e Tecnologie dell'Informazione

to all the people who believe in me

Abstract

This thesis is focused on the design of two interrogation systems for Fiber Bragg Grating (FBG) sensors based on the Wavelength Domain Multiplexing (WDM) by means of the Arrayed Waveguide Grating (AWG) device. The FBG sensors have been employed in a large number of environments thanks to their intrinsic characteristics. To design a measurement system based on the Fiber Optic Sensor (FOS) technology, it is mandatory to make use of an optoelectronic system with the aim to "read" the wavelength shifting performed by the sensors. This latter is named interrogation system and, actually, sets a limit on the employability of the FBG sensors, due to its cost, design complexity and low reliability in some contests. For this reasons, the researchers are constantly looking on new technologies for the design of innovative interrogation systems. The AWG device seems to provide characteristics which cannot be reached with other devices and, due to its passivity, gives the possibility to increase the system speed to let the FBG sensors to be employed also for the detection of high-speed phenomena. Furthermore, thanks to the robustness and reliability of AWG device, is possible to turn an interrogation system into a full analog monitoring system employable in a safety scenario, such as industrial processes or other kind of environments, in which digital processing does not ensure enough reliability.

Acknowledgments

Index of contents

List of Abbreviations

FBG	Fiber Bragg Grating
FOS	Fiber Optic Sensor
AWG	Arrayed Waveguide grating
SMF	Single-Mode optical Fiber
FWHM	Full Width at Half Maximum
FSR	Free Spectral Range
FP	Fabry-Perot
TDM	Time Division Multiplexing
WDM	Wavelength Division Multiplexing
KLT	Karhunen-Loeve Transform
PHASAR	Phased Array
WGR	Waveguide Grating Router
SoS	Silica-on-Silicon
FPR	Free Propagation Region
EDFA	Erbium-Doped Fiber Amplifiers
ASE	Amplified Spontaneous Emission
MMI	Multi-Mode Interferometer
MZI	Mach-Zender Interferometer
SLD/SLED	Super Luminescent Diode
FPI	Fabry-Perot Interferometer
EFPI	Extrinsic Fabry-Perot Interferometer
DAQ	Digital AcQuisition board
GUI	Graphical User Interface
MOI	Micron Optics Interrogator
PLC	Programmable Logic Controller

PFRC	Power Fluctuation Rejection Circuit
TIA	TransImpedance Amplifier
GBP	Gain Bandwidth Product
CME	Common Electrical Module
CMS	Compact Muon Solenoid
LHC	Large Hadron Collider
CERN	European Center for the Nuclear Research
DSS	Detection Safety System
USC	Underground Service Cavern
UXC	Underground Experimental Cavern
BSS	Broad band Spectrum Source
ASIC	Application Specific Integrated Circuit

Introduction

Despite the benefits presented by electrical sensors, which have been for decades the standard mechanism for the monitoring of physical phenomena, they exhibit intrinsic limitations (e.g., transmission loss and susceptibility to electromagnetic interference) making their usage challenging or impractical in many applications.

Fiber Optic Sensor (FOS) technology, whose advantages are well explained in the following discussion, is an excellent solution to these challenges: it takes advantage of using light signal rather than electricity and standard optical fiber in place of copper wire. One of the most commonly used and broadly employed optical sensor is the fiber Bragg grating (FBG), which reflects a wavelength of a light signal that shifts in response to variations in temperature and strain. Typically, recovery of strain and/or temperature information is accomplished by means of an optical instrumentation (i.e., the interrogation system) to convert the well-known temperature/strain-induced wavelength response of an FBG sensor, to an output electrical signal directly proportional to the physical quantity detected. However, the cost of implementing a FOS system is often prohibitive, limiting the usage of this technology in many environments. This is due to the complex design from which an interrogator is made, requiring precision optical components, such as scanning filters or tunable lasers, to perform a high accuracy wavelength detection. For this reason, although different kinds of interrogation techniques have been studied, the majority of interrogation systems requires expansive components and equipment to measurements.

With the aim to mitigate the disadvantages of the state-of-art interrogation systems and open the world of FBG sensors in other measurement environment, this thesis is presented. The main finding of this thesis is the design and characterization of two different interrogation systems which are based on the Arrayed Waveguide Grating (AWG) device, working as an optical prism with the aim to separate a polychromatic input in many monochromatic outputs in function of its output channel wavelength:

- The first one takes the advantages presented by the AWG device (working as a passive device above all), to be the core of an interrogation system which is characterized by a high-speed response and a modular dynamic range in function of the AWG output channels.
- The second one takes advantage of the robustness and the reliability of the AWG device connected to a full analog modular PCB, turning a FOS interrogation system in a safety monitoring system without employing digital processing and with an output in current variation compatible with 4-20mA standard.

The thesis is organized as follows:

- Chapter 1 is dedicated to the FBG theoretical model, focusing on its working principle and its dependence with the temperature, strain and radiation, as well as an overview of the most important interrogation system.
- Chapter 2 has the goal to introduce the AWG device through its theoretical model, in order to give an explanation of the state of art AWG-based interrogation systems, compared to the non-AWG one. The theoretical model of both FBG and AWG devices are needed to have a comprehensive view of the proposed systems working principle which are clarified in chapter 3 and 4.
- Chapter 3 is about the design, simulation and experimental results of the proposed high frequency with modular dynamic range AWG-based interrogation system. Focusing on both optical and electrical part. This latter comprises a series of simulations to justify the choice of the devices employed. Many considerations about the optical working principle in respect of the other AWG-based systems are present.
- Chapter 4 is devoted to an innovative full analog AWG-based interrogation system for safety monitoring application. In this chapter a description of the optoelectronic system is contained with numerical simulation about the analog section. Some measurements about the reliability and the repeatability of the proposed concept are conducted as well.

- The conclusion recapitulates the achievements of the thesis, underlying the results obtained and the possible improvements to do as future work.

Chapter 1: Fiber Bragg Grating Sensor

Fiber Bragg Grating structures are designed affecting the optical fiber core with a periodic (or quasi-periodic) modulation of the refractive index. They are created by exposing the fiber core to an interference pattern of UV energy. The fixed index modulation obtained according to the exposure is called grating [1] and a small amount of light is reflected at each period. All the reflected light signals combine coherently to one large reflection at a particular wavelength. This is referred to as the Bragg condition, and the wavelength at which this reflection occurs is called the Bragg wavelength [2], [3]. The first formation of grating structure within an optical fiber was demonstrated in 1978 [4], [5]: after the exposure of a germanium doped fiber with a high intensity Argon-ion laser, a permanent narrowband Bragg grating filter was created. The Bragg grating is named after William Lawrence Bragg, who formulated the conditions for X-ray diffraction (Bragg's Law). The gratings first written, initially referred to as "Hill gratings", were actually a result of research on the nonlinear properties of germanium-doped silica fiber. Almost a decade later, in 1989, Meltz and co-workers showed that it was possible to write gratings from outside the optical fiber using a wavelength of 244nm [6]. This proved to be a significant achievement as it made possible future low-cost fabrication methods of FBG. Since the discovery of photosensitivity in optical fiber by Hill and the developments of the holographic writing method by Meltz, hundreds of articles have been published concerning photosensitivity of FBG.

To overcome the limitations of two-beam holographic technique, phase mask technique for fabricating gratings was reported by Hill et al. [7] in 1993. This new technique has removed the complexity in the manufacturing process of FBGs, making them reproducible at lower costs. The commercial products of FBG have been available since early 1995. Today, FBGs have become almost synonymous with the field itself and most fiber optic sensor systems make use of Bragg grating technology.

1.1   Theoretical Model of FBG

An FBG, as already said, is composed by a periodic modulation of the refractive index. In Figure 1.1 it is shown the working principle: when a broadband source irradiates a signal towards the FBG, a particular wavelength which satisfies Bragg condition will be reflected, while the remaining part is transmitted without losses. This happens since the periodic refractive index variation reflects the incoming light forming, with constructive interference, a back reflected peak signal with the grating characteristics. The aforementioned wavelength characterized by the maximum efficiency of reflectance is called Bragg wavelength [8], [9].

Within an optical fiber, the phase matching condition is given by:

$$\beta_1 - \beta_2 = \Delta\beta = \frac{2\pi}{\Lambda} \qquad (1.1)$$

where β_1 and β_2 are the propagation constants of the modes being coupled and Λ is the grating period. In the case study of the FBG structure, the propagating core mode towards the FBG (LP_{01}) couples to the reflected one. Hence the propagation constants remain the same but with negative sign.

$$\beta_1 = -\beta_2 = \beta \qquad (1.2)$$

thus, the phase matching becomes

$$\beta - (-\beta) = \frac{2\pi}{\Lambda} \qquad (1.3)$$

$$2\beta = \Delta\beta = \frac{2\pi}{\Lambda} \qquad (1.4)$$

Since the grating periodicity will be small (hundreds of nm), $\Delta\beta$ is large. But

$$\beta = \frac{2\pi}{\lambda} n_{eff} \qquad (1.5)$$
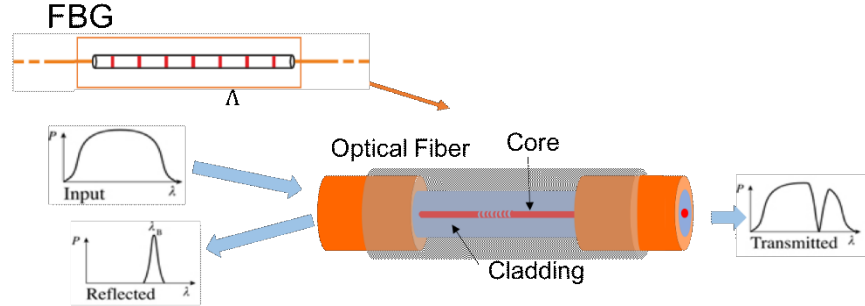
Figure 1.1: Working principle of a Fiber Bragg grating structure.

with n_{eff} the effective refractive index of the core propagating inside the optical fiber. The equation (1.4) becomes

$$2\left(\frac{2\pi}{\lambda}n_{eff}\right) = \frac{2\pi}{\Lambda} \tag{1.6}$$

from which the Bragg wavelength can be extrapolated

$$\lambda_B = 2n_{eff}\Lambda \tag{1.7}$$

where, as said before, n_{eff} is the effective refractive index of the fiber core and Λ is the pitch of the grating.

The equation (1.7) implicates that every variation in either the effective refractive index or in the grating period will cause a change in the Bragg wavelength reflected from the structure.

The Bragg condition can also be calculated considering the energy and momentum conservation: the energy conservation ($hw_i = hw_f$) means that the frequency of the reflected radiation is the same as the incident one. The momentum conservation requires that the sum of incident wave vector $\overrightarrow{k_i}$ and the grating wave vector $\vec{K}$, must be equal to the wave vector of the scattered radiation $\overrightarrow{k_f}$. $\vec{K}$ is directed normal to the grating plane with a magnitude $2\pi/\Lambda$, with Λ the grating pitch [10]. The diffracted wave vector is equal and opposite to the incident wave vector, so the momentum conservation can be written as:

$$2\left(\frac{2\pi}{\lambda_B}n_{eff}\right) = \frac{2\pi}{\Lambda} \tag{1.8}$$

that simplifies to the first order the Bragg condition of equation (1.7). If the Bragg condition is not satisfied, the reflected light from each plane becomes out of phase and gradually canceled. Light which is not coincident with the Bragg wavelength will get transmitted with very low losses.

1.1.1 Refractive Index Change

The easiest way to describe a Bragg grating structure within an optical fiber is an axial and periodic change of the refractive index with a profile described by the next formula [10]:

$$n_{eff}(x) = n_0 + \Delta n \cos\left(\frac{2\pi x}{\Lambda}\right) \tag{1.9}$$

where Δn is the amplitude of the refractive index variation and n_0 is the average index of the fiber core. The axial distance is described by x, while Λ is the grating period.

1.1.2 Bragg Grating Reflectivity

The reflectivity of a generic grating can be expressed with the coupled-mode theory of Lam and Garside [11]:

$$R(l, \lambda) = \frac{\Omega^2 \sinh^2(sl)}{\Delta k^2 \sinh^2(sl) + s^2 \cosh^2(sl)} \tag{1.10}$$

where $R(l, \lambda)$ is a number between 0 and 1 depending on the optical power reflected by a grating of length l at a wavelength λ. $\Delta k = k - \frac{\pi}{\lambda}$ is the detuning wave vector, while $k = \frac{2\pi n_0}{\lambda}$ is the propagation constant. $s = \sqrt{\Omega^2 - \Delta k^2}$ and the coupling coefficient (Ω) for a sinusoidal index modulation along the fiber axis is:

$$\Omega = \frac{\pi \Delta n \eta(V)}{\lambda} \tag{1.11}$$

where $\eta(V)$ is a function of the normalized frequency V for the fiber, representing the fraction of the fiber mode power contained within the core. $\eta(V) \approx 1 - 1/V^2$. The normalized frequency V can be expressed as:

$$V = \frac{2\pi}{\lambda} a (n_{co}^2 - n_{cl}^2)^{\frac{1}{2}} \tag{1.12}$$

where a is the core radius, n_{co} and n_{cl} are the core and cladding refractive indices. At the Bragg wavelength, there is no wave vector and $\Delta k = 0$. Therefore:

$$R(l, \lambda) = \tanh^2(\Omega l) \tag{1.13}$$

according to the equation (1.13), the Bragg grating reflectivity (showed in Figure 1.2) depends on the grating strength. This means that it can be increased by increasing the magnitude of the refractive index change. A typical value of the index modulation is 10^{-3} in silica fibers. The reflectivity is also dependent on the size of the fabrication system and is typically a few of centimeters. To achieve an FBG close to 100% reflection, the length of the gating must be increased.

1.1.3 Bragg Grating Full Width at Half Maximum (FWHM)

The Full Width at Half Maximum (FWHM) of a Bragg grating is calculated as the difference between two wavelengths on the reflectance spectrum, where the reflectivity drops at the half of its maximum [12][13]. Increasing the length, the reflectivity will increase as well, while the FWHM get reduced. An approximated expression is given by:

$$\Delta \lambda_{FWHM} = \lambda_B \alpha \sqrt{\left(\frac{1}{2}\frac{\Delta n}{n}\right)^2 + \left(\frac{1}{N}\right)^2} \tag{1.14}$$

where N is the number of grating planes from which the structure is composed; $\alpha \approx 1$ for gratings with almost 100% of reflectance while $\alpha \approx 0.5$ for weaker [14].

1.2   FBG as Sensor

Fiber gratings are mainly employed as sensors as is shown in this thesis during experimental analysis. The basic principle is to monitor the Bragg wavelength shifting of an FBG which changes with the measurand. As described by the equation (1.7), the Bragg wavelength is depending on the grating period and the effective refractive index. This means that any change in the refractive index or the grating period due to external variation of the measurand, will lead to a change in the Bragg wavelength of the sensor that can be detected either with the reflected or with the transmitted spectrum. The basic parameters which cause the FBG central wavelength are strain (ϵ) and
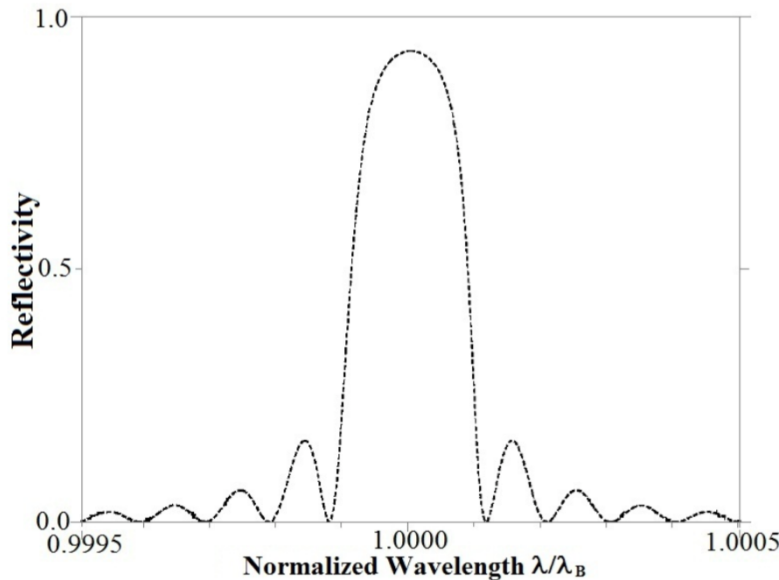
Figure 1.2: Fiber Bragg grating reflectivity spectrum with $\Omega l = 2$ [9].

temperature (T). This means that the Bragg wavelength is function of both temperature and strain ($\lambda_B = \lambda_B(\epsilon, T)$) considered as independent variables [15], [16]. Since the measurement induces a differential change in the wavelength, the differential of λ_B is calculated as:

$$
\begin{aligned}
d\lambda_B &= \frac{\partial \lambda_B}{\partial \epsilon} d\epsilon + \frac{\partial \lambda_B}{\partial T} dT \\
&= \left[\frac{\partial}{\partial \epsilon} \left(2n_{eff}\Lambda \right) \right] d\epsilon + \left[\frac{\partial}{\partial T} \left(2n_{eff}\Lambda \right) \right] dT \\
&= \left[\frac{2n_{eff}\partial \Lambda}{\partial \epsilon} + \frac{2\partial n_{eff}}{\partial \epsilon} \Lambda \right] d\epsilon + \left[\frac{2n_{eff}\partial \Lambda}{\partial T} + \frac{2\partial n_{eff}}{\partial T} \Lambda \right] dT
\end{aligned}
\tag{1.15}
$$

dividing the equation by $\lambda_B = 2n_{eff}\Lambda$,

$$
\frac{d\lambda_B}{\lambda_B} = \left[\frac{1}{\Lambda} \frac{\partial \Lambda}{\partial \epsilon} + \frac{1}{n_{eff}} \frac{\partial n_{eff}}{\partial \epsilon} \right] d\epsilon + \left[\frac{1}{\Lambda} \frac{\partial \Lambda}{\partial T} + \frac{1}{n_{eff}} \frac{\partial n_{eff}}{\partial T} \right] dT
\tag{1.16}
$$

it is clear from the last equation that the Bragg wavelength is shifted by both temperature (by the second term) and strain (by the first one) variations.

1.2.1 Strain sensitivity of FBG

The applied strain experiences a peak wavelength shift of the FBG sensor: this is the basic operation for an FBG strain sensor [19]. These sensors are widely employed since they are extremely sensitive for various materials and structures. Strain sensing plays a significative role in the health monitoring system for civil, mechanical and aerospace applications. The first application of FBG for this kind of measurements was first introduced in 1988 [17]. The equation 1.16 shows two former parts which cause strain and temperature induced shifting of the Bragg grating structures: the physical elongation of the optical fiber represented by a change in the grating spacing and the change in the effective refractive index due to the photo elastic effect [18]–[20]. The only strain optic effect can be expressed as:

$$
\Delta \lambda_B = (1 - p_e)\lambda_B \epsilon
\tag{1.17}
$$

where the term ϵ is the axial strain caused by the fiber micro-strain, $\Delta \lambda_B$
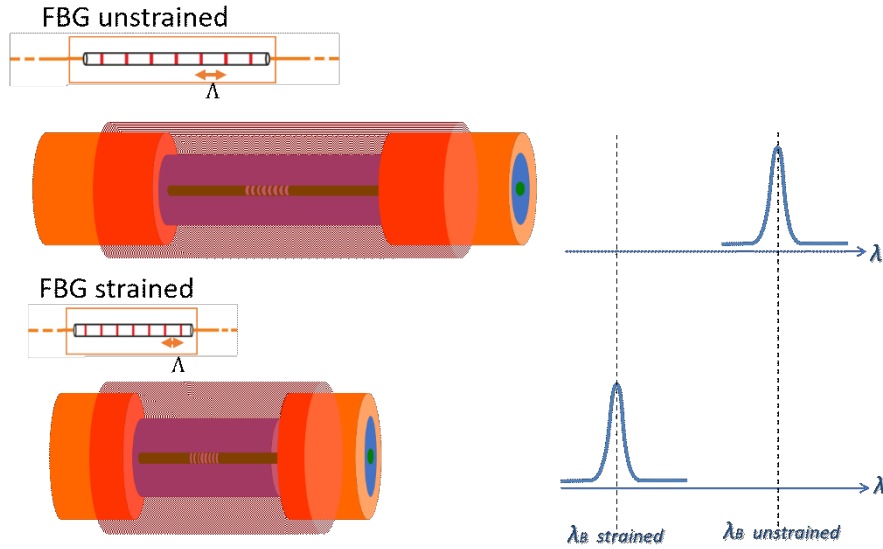
Figure 1.3: Bragg wavelength shifting comparison between unstrained structure and strained.

is the shift in wavelength (in nm) and p_e is the photoelastic coefficient of the fiber described by

$$p_e = \left(\frac{n_{eff}^2}{2}\right)[p_{12} - v(p_{11} + p_{12})] \tag{1.18}$$

where p_{11} and p_{12} are the components of photoelastic strain tensor and v is Poisson's ratio. Figure 1.3 shows the wavelength shifting in case of the grating structure get compressed, compared with a normal case.

FBG measurement system for strain application is an active field due to its performance accuracy and versatility and, nowadays, is getting more and more used for structural monitoring and other smart applications [21]–[27].

1.2.2 Temperature sensitivity of FBG

The temperature response, as in the case of the strain, is given by the sum of two factors: the thermal expansion of the fiber which results in a change of the grating pitch and the change of the effective

refractive index due to the thermo-optic effect. Hence, the Bragg wavelength shift due to temperature variation can be calculated as

$$\Delta\lambda_B = (\alpha + \xi)\lambda_B\Delta T \tag{1.17}$$

where $\alpha = \left(\frac{1}{\Lambda}\right)\left(\frac{\partial\Lambda}{\partial T}\right)$ is the coefficient of thermal expansion, while $\xi = \left(\frac{1}{n_{eff}}\right)\left(\frac{\partial n_{eff}}{\partial T}\right)$ is the thermo-optic coefficient which characterizes the fiber and ΔT is the temperature variation. The parameters α and ξ are functions of temperature and are not linear for high temperature value as showed in [19]–[21]. If the fiber stretch due to a temperature increment, the grating pitch increases and the Bragg wavelength shift towards higher values. For the silica fibers the thermo-optic coefficient is a dominant factor with the 95% of the observed shifting. the thermal expansion accounts only for 5%. Nowadays, the FBG is employed in a high number of applications for temperature monitoring, substituting the electrical PT sensors which are invasive and not suitable for harsh environments.

1.2.3 Temperature compensation during strain measurement

As previously discussed, an FBG sensor produces a wavelength shifting both for strain and temperature variation. The strain affects the grating in a direct way compressing or stretching the pitch, while the temperature sensitivity depends mainly on the effective refractive index change. Hence, the FBG sensor is simultaneously affected by strain and temperature variations.

The combined Bragg wavelength can be written as follows

$$\Delta\lambda_B = [(1 - p_e)\epsilon + (\alpha + \xi)\Delta T]\lambda_B \tag{1.18}$$

using the aforementioned variables, the equation becomes

$$\Delta\lambda_B = \left(\left\{1 - \left(\frac{n_{eff}^2}{2}\right)[p_{12} - v(p_{11} + p_{12})]\right\}\epsilon \right.$$
$$\left. + \left\{\left(\frac{1}{\Lambda}\right)\left(\frac{\partial\Lambda}{\partial T}\right) + \left(\frac{1}{n}\right)\left(\frac{\partial n}{\partial T}\right)\right\}\Delta T\right)\lambda_B \qquad (1.19)$$

implicating the need of a discrimination between the strain and temperature effects in order to disentangle the two physical parameters. Various methods were proposed [28]–[33]. In a method proposed in [34] a pair of FBGs are involved, both sensing temperature variations, with one of them protected from strain. A constrain requires that both FBGs are characterized by the same sensitivity to temperature. Another method is to employ two FBG sensors with a significant change in the central wavelength, showing a different response over the same measurement [35]. FBGs written on different fiber diameters were proposed as well, which give different strain responses with the same temperature sensitivity [36], [37]. Also writing close wavelengths FBG within an undoped and boron co-doped fibers, a different temperature sensitivity is obtained while the strain sensitivity remains the same for both [38]. in these reported papers, special fibers are needed or normal fibers with special spectroscopic techniques in order to discriminate temperature and strain simultaneously [38]–[40]. A different method using nonlinear effect as the Brillouin scattering is presented in [41], while an approach to resolve the cross sensitivity is reported in [42] in which acrylate and polyimide polymers were used as coating for different FBGs achieving synchronized sensing of axial strain and temperature changes.

Is reported in what follows an elegant way with analytical approach described in [43]. The solution consists of using, for a given FBG for strain measurements, another FBG on the same fiber at the same temperature to the one close to it. The two FBGs, on the same optical fiber, will experience two different Bragg wavelength variations: one dependent on strain and the other dependent on temperature. For the first FBG the equation describing the wavelength deviation is

$$\Delta\lambda_{B1} = K_{\epsilon1}\Delta\epsilon + K_{T1}\Delta T \qquad (1.20)$$

where

$$K_{\epsilon 1} = (1 - p_e)\lambda_{B1} \qquad (1.21)$$
$$K_{T1} = (\alpha + \xi)\lambda_{B1} \qquad (1.22)$$

while for the other FBG

$$\Delta\lambda_{B2} = K_{\epsilon 2}\Delta\epsilon + K_{T2}\Delta T \qquad (1.23)$$

where

$$K_{\epsilon 2} = (1 - p_e)\lambda_{B2} \qquad (1.24)$$
$$K_{T2} = (\alpha + \xi)\lambda_{B2} \qquad (1.25)$$

Equations (1.20) and (1.23) can be written as matrix in the form

$$\begin{bmatrix} \Delta\lambda_{B1} \\ \Delta\lambda_{B2} \end{bmatrix} = \begin{bmatrix} K_{\epsilon 1} & K_{T1} \\ K_{\epsilon 2} & K_{T2} \end{bmatrix} \times \begin{bmatrix} \Delta\epsilon \\ \Delta T \end{bmatrix} \qquad (1.26)$$

Equation (1.26) is called wavelength shift matrix since by its solution the wavelength displacement of both FBGs can be obtained as a function of temperature and strain. By the way, what is needed is to find the sensing matrix calculating the strain and temperature as function of the wavelength displacement, that is the inverse matrix of (1.26).

$$\begin{bmatrix} \Delta\epsilon \\ \Delta T \end{bmatrix} = \begin{bmatrix} K_{\epsilon 1} & K_{T1} \\ K_{\epsilon 2} & K_{T2} \end{bmatrix}^{-1} \times \begin{bmatrix} \Delta\lambda_{B1} \\ \Delta\lambda_{B2} \end{bmatrix} \qquad (1.27)$$

inverting it becomes

$$\begin{bmatrix} \Delta\epsilon \\ \Delta T \end{bmatrix} = \frac{1}{K_{\epsilon 1}K_{T2} - K_{\epsilon 2}K_{T1}} \begin{bmatrix} K_{T2} & -K_{T1} \\ -K_{\epsilon 2} & K_{\epsilon 1} \end{bmatrix}^{-1} \times \begin{bmatrix} \Delta\lambda_{B1} \\ \Delta\lambda_{B2} \end{bmatrix} \qquad (1.27)$$

Approximating $K_{\epsilon 1}K_{T2} \approx K_{\epsilon 2}K_{T1}$ will give no solution for equation (1.27) since (1.20) and (1.23) will become two almost parallel lines. This happens if the FBGs exhibit the same coefficients and central wavelength reflection. It's worth to note that eq. (1.21) and eq. (1.24)

as well as eq. (1.22) and eq. (1.25) differ only from the Bragg wavelength, so, to avoid a possible redundancy, Bragg reflections wide apart are required for the two FBGs. Solving the previous equation are obtained two equations

$$\Delta\epsilon = \frac{1}{K_{\epsilon1}K_{T2} - K_{\epsilon2}K_{T1}} \left(K_{T2}\Delta\lambda_{B1} - K_{T1}\Delta\lambda_{B2}\right) \qquad (1.28)$$

$$\Delta T = \frac{1}{K_{\epsilon1}K_{T2} - K_{\epsilon2}K_{T1}} \left(K_{\epsilon1}\Delta\lambda_{B2} - K_{\epsilon2}\Delta\lambda_{B1}\right) \qquad (1.29)$$

Supposing that the FBG2 is strain free, the eq. (1.28) gives the real strain of FBG1 measured by $\Delta\lambda_{B1}$, compensated in temperature by $\Delta\lambda_{B2}$. Eq. (1.29) gives the temperature of both sensors.

1.2.4 Refractive Index Sensitivity

In standard SMF the propagating mode is strongly confined within the core and protected by the cladding layer avoiding any influence by the medium refractive index on the guiding properties. Thus, the effective refractive index is not affected by the external conditions, leading to no sensitivity to the bordering medium refractive index. If the cladding diameter is reduced along the grating region, the effective refractive index will be affected by the surrounding medium [44]–[46]. As consequence, in etched optical fibers, a strong spectral response may occur in the FBG. This effect is useful in chemical and in bio sensing applications [47]–[50]. The first demonstration was done by [51] in 1997, it was based on the application of chemical etching to the grating region within the fiber.

1.2.5 Effect of γ-Radiation on FBG

As demonstrated in the last two decades, in which several experiments were investigated on the FBG behavior in ionizing radiation environment [52], the Bragg structure is affected by the phenomena of ionizing radiation. This latter induces a change in both refractive index and grating pitch resulting in a Bragg wavelength shift:

$$\frac{\Delta\lambda_B}{\lambda_B} = \frac{\Delta n_{eff}}{n_{eff}} + \frac{\Delta\Lambda}{\Lambda} \qquad\qquad (1.30)$$

From the state of art, it is noted that under γ-radiation the central wavelength shifts towards the red with a saturated spectrum. The Bragg wavelength saturation values and the doses absorbed depend on the fiber composition and the grating inscription. This constrain does not apply for N-doped silica in which the Bragg wavelength does not exhibit a saturation effect up to a 1.5MGy dose [53]. Recent studies showed that the FBGs written in fluorine-doped fibers are the most resistant under γ-radiation. In [54] the authors present a $\Delta\lambda_B$ with a saturation around 5pm at low γ-dose (5kGy). The goal of the cited experimental investigation is to apply this technology to the monitoring of radiation environment, e.g. nuclear power plants [55].

In another work [57], for the germanosilicate fibers, the γ-radiation can be considered as a further UV-light exposure due to the generation of same paramagnetic defects as the UV-light. Furthermore,
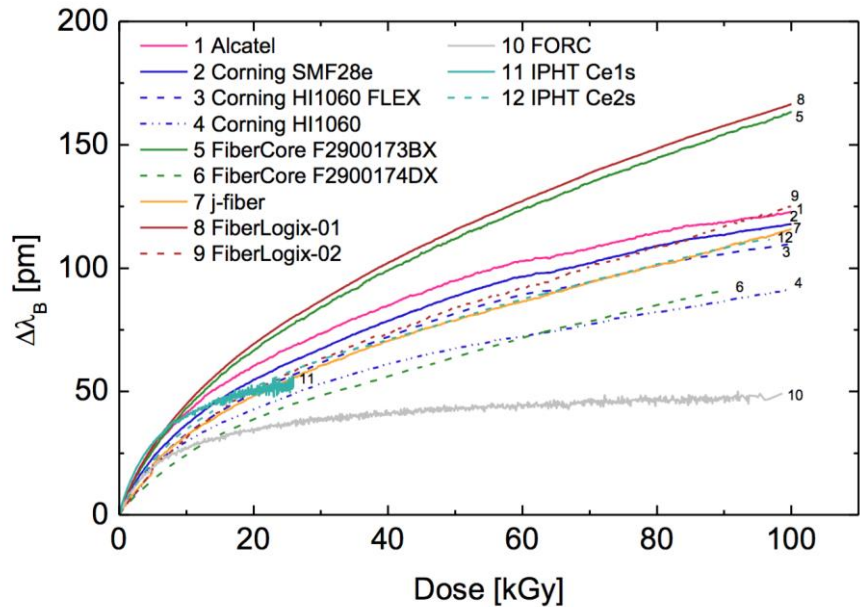
Figure 1.4: Wavelength shifting of many gratins made of different fibers, during an irradiationup to 0.1MGy with a rate of 0.9Gy/s [56].

the γ-radiation should affect only the mean value of the effective refractive index and
not the modulation amplitude [58]. The saturating behavior can be explained through two main reasons [59]: the limited concentrations of precursor defects, affecting with the refractive index change and the competition between the annealing and the generation of the defects [56], depending on the radiation dose-rate and the annealing rate. In conclusion, the Bragg wavelength shifting is function of the manufacturing parameters [60] such as: composition of the fiber, irradiation parameters, temperature and so on. In Figure 1.4 it can be noticed that a wavelength shifting with identical manufacturing and irradiation conditions of many gratings produced with different doping. The plot shows that it is not possible to find a clear correlation between the observed radiation sensitivity and the fiber composition.

1.3   FBG Interrogation Systems

Typical interrogation systems detect the spectrum reflected by the sensing structure on a wavelength interval ranging from 40nm to 80nm. Many FBG interrogator such as Fabry-Perot interferometer [16], Mach-Zehnder interferometer [61], holographic fiber grating based spectroscopic charge coupled device [62], discriminator using the power ratio of optical filters have been reported in literature [63]. Most systems are based on a broadband light source and a spectrometer for detection; this approach provides long-term stability and is relatively inexpensive, but the spectrum is sampled with a coarse wavelength resolution, typically 512 samples over 40 nm or 80 nm interval [64], [65]. However, none of them are enough to satisfy main characteristics such as: response speed, precision, accuracy, cost and sensor multiplexability.
Although a wide variety of techniques are demonstrated in literature for monitoring Bragg wavelength shifts, only certain techniques appear to have the potential for being reduced to a practical, cost-effective instrumentation systems for use in real-world applications. As already said the FBGs are the most popular technology for the measurement of temperature, deformations, strains and vibrations using photonics. The high cost offered by many FBG interrogation technique severely limits the range of potential application [66].
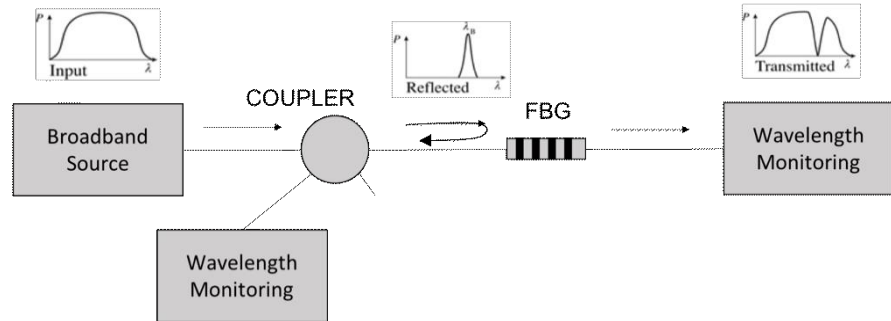
Figure 1.5: A typical method for the wavelength detection composed by an input spectrum, an optical circulator, the FBG under interrogation and a wavelength monitoring for the reflected and transmitted signal.

The basic working principle of an FBG sensor system is to monitor the shift in wavelength of the reflected signal with the changes in temperature or strain, as depicted in Figure 1.5. For instance, to detect either a temperature change of 0.1°C or a variation of 1μstrain, a wavelength resolution of 1pm is required (at λB of ~1300nm). Although this wavelength resolution is attainable using laboratory instrumentation, the ability to resolve changes on this order is a challenge and this was the focus of a considerable amount of research work in the grating sensor field. The most frequently utilized method for the interrogation of FBG sensors is based on passive broadband illumination of the device. In this section follows a briefly description of the most important interrogation techniques for wavelength detection.

1.3.1 Scanning Filter Method

This method allows the shift in the FBG wavelength of the sensor element to be assessed by comparing the FBG reflected light to that propagated through a direct reference path. One of the most successful techniques for interrogating FBG sensor is based on the use of a tunable passband filter for tracking the signal. The most commonly used technique is based on the use of Fabry-Perot (FP) filters [67] as depicted in Figure 1.6. Here, light reflected from an array of Bragg grating sensors is passed through a FP filter which passes one narrowband wavelength component depending on the spacing between
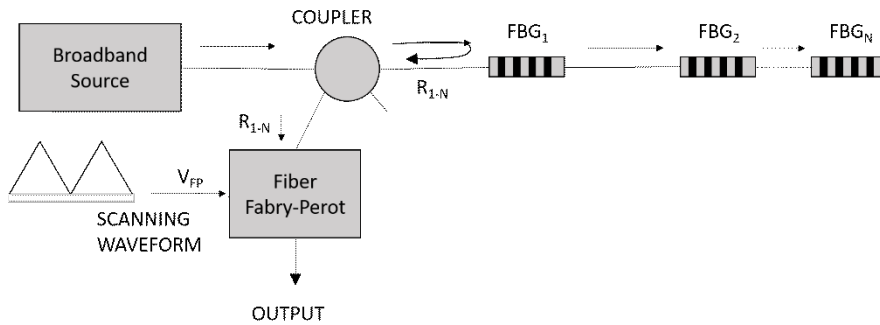
Figure 1.6: Scanning filter FBG interrogation technique.

the mirrors in the device that are controlled electrically via piezoelectric stack. As the filter is tuned, the passband scans over the return signals from the FBG and the wavelengths can be determined and recorded from the voltage applied to the filter as the return signals are detected. Typical characteristics of the type of FP used are a free spectral range (FSR) of 50nm and a bandwidth of 0.3nm. This allows as many as 16 individual sensors spaced by 3nm. For this FSR value, generation of the scanning voltage for the FP filter via a 16-bit DAC produces a minimum resolvable wavelength shift of approximately 0.8 pm (or an equivalent strain resolution of 0.8μstrain).

currently available FP filters can be scanned at more than 300Hz, although scan rate to 1kHz should be possible.

1.3.2 Time and Wavelength Division Multiplexing (T-WDM) Method

A primary advantage of using FBGs for distributed sensing is that large number of sensors may be interrogated along a single fiber. WDM provides for tens of sensors per fiber, but TDM can multiply this number several times re-using the source spectrum. Considering the WDM/TDM of Figure 1.7, several stepped arrays are concatenated, each at a greater distance along the fiber. Launching a short pulse of light from the source, the reflections from FBG's at successively more distant positions along the fiber, will return to the detector at successively later times. The detection instrumentation is configured to respond to the reflected signals only during a selected window of time
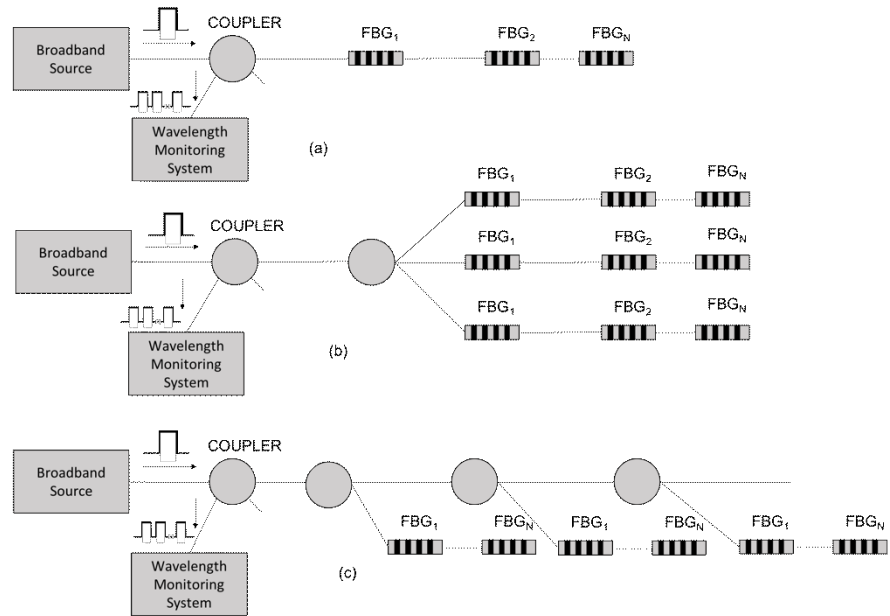
Figure 1.7: WDM and TDM for FBG arrays: (a) serial system; (b) parallel system; (c) branching network [16].

after the pulse is launched, so only a single WDM set of sensors is selected for detection. Multiple-reflection crosstalk arises due to light reflected from one grating which arrives in the time window allotted to the detection of a downstream grating, because multiple reflection paths have delayed some of the first grating's signal. The effect is, obviously, strongly dependent on the reflectivity of the gratings, and can be

minimized by the use of low reflectivity gratings. Another issue is given by the Spectral-shadowing crosstalk: If the two gratings' center wavelengths are slightly offset, it appears as though the downstream FBG is shifted further in the direction of the actual offset. The worst-case distortion, with two FBG's equal in width and reflectivity, occurs approximately when they are spectrally offset by their FWHM. The error will vary with the detection method, but errors >1 μstrain are projected for a pair of interfering FBGs with reflectivity >5% [68].

1.3.3 Interferometer Technique Method

The use of interferometric configuration as FBG interrogator has been described in several groups. An unbalanced interferometer is an optical filter with a transfer function in the form 1+cosϕ, where the phase term depends on the input wavelength. As depicted in Figure 1.8, the light reflected from a grating is directed through an interferometer which has unequal paths. Due to the wavelength dependence of the phase, shifts in Bragg wavelength are converted into phase shifts. One warning with this approach is given by the effective coherence

length of the light reflected from the grating. Various phase-reading techniques can be applied to determine the phase modulation $\Delta\phi$ induced by the wavelength shift $\Delta\lambda$ through the formula:

$$\Delta\phi = \frac{2\pi nd}{\lambda^2}\Delta\lambda \qquad (1.31)$$

By appropriate choice of the interferometer OPD, this technique can be made to be extremely sensitive to weak dynamic Bragg wavelength shifts: for example, with an OPD of 1cm (6.7 mm fiber length), using the grating strain response of approximation
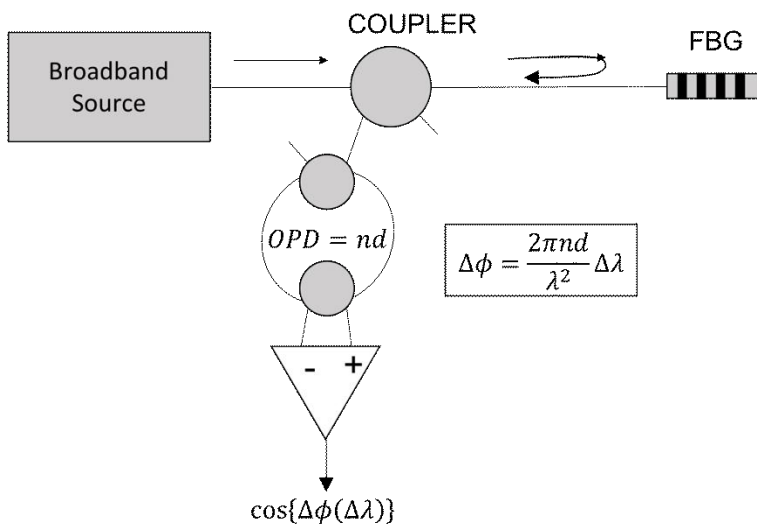
Figure 1.8: Interferometric technique for the detection of FBG sensors.

1nm/1000μstrain (at 1300nm), the strain-to-phase response of the system is 0.037rad/μstrain. Although this sensitivity has yet to be demonstrated, a sensor with an equivalent wavelength shift corresponding to a strain change on the order of 10^{-6}nm at 1300nm (or 100kHz shift in optical frequency), has been demonstrated [16].

1.3.4 Charge Coupled Device Method

A more rugged method involves the use of a charge-coupled device and a fixed dispersive element (shown in Figure 1.9). With this method, a broadband source illuminates the FBG, then a reflected light wave is passed through a dispersive element that distributes the various wavelength components to different locations on a linear CCD sensor. This method can yield fast with simultaneous measurements of all FBGs in the array, but it offers limited resolution and SNR. For example, detecting an FBG peak shift of 1pm over an 80nm range requires a linear CCD with at least 20,000 pixels. This is more than 3 times the pixel amount of the linear CCDs currently available on the market. Additionally, the power of a broadband source is spread across a wide wavelength range producing low energy FBG reflections that can be difficult to detect [69].
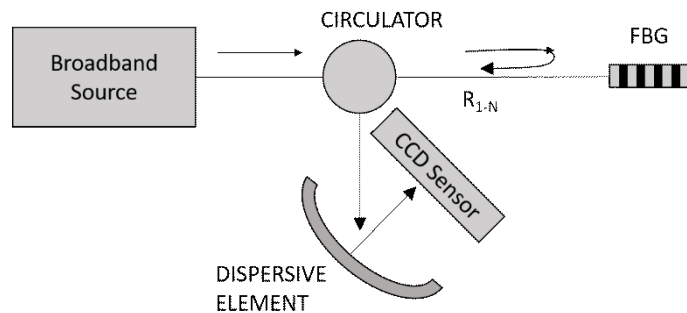
Figure 1.9: Wavelength position conversion method for the interrogation of FBG sensors.

1.3.5 Optical Spectrum Analyzer Method

At the state of art, the most powerful interrogation can be obtained using an Optical Spectrum Analyzer. The OSA is an

instrument that is used to measure the spectral density of a light signal at different wavelengths (an example is depicted in Figure 1.10). It is one of the most useful instruments in fiber-optic systems and device measurements, especially when wavelength division multiplexing is introduced into the systems where
different data channels are carried by different wavelengths. An OSA is often used to find optical signal power level at each wavelength channel, evaluate optical SNR and optical crosstalk, and check the optical bandwidth when an optical carrier is modulated. The most important parameter that an OSA provides is the optical spectral density versus wavelength; the unit is expressed in watts per Hertz and is defined as the optical power within a bandwidth at a certain wavelength. The OSA presents a typical wavelength range from 400nm to 1700nm and a wavelength accuracy of less than 0.1nm but has the disadvantages of a limited speed and with a low resolution compared the other technique. Furthermore, it is expansive and have a large size [70].

1.3.6 Tunable Laser Method

In this application, the main component is a tunable laser source which is a wavelength-tunable laser with a narrow optical bandwidth that is used for recording spectrum with very high frequency resolution [71]. As shown in Figure 1.11, in order to measure the Bragg wavelength value of the connected FBG, the laser is swept over the relevant range of the spectrum, while a detector measures the optical power reflected from the sensor. The processing and control electronics
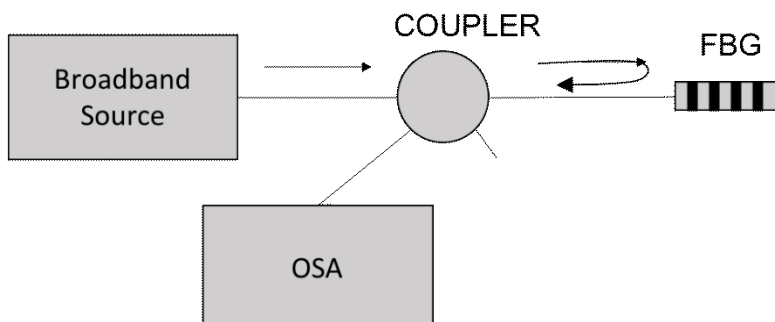
Figure 1.10: Wavelength interrogation with OSA.
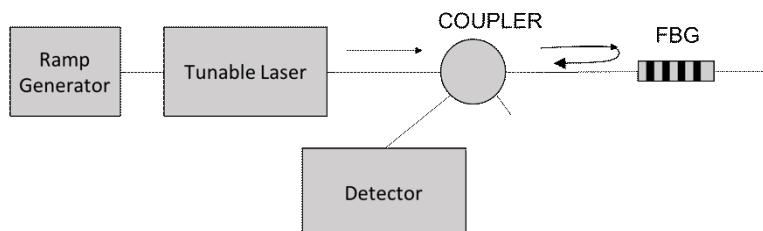
Figure 1.11: Interrogation technique based on tunable laser as source.

record the power correlated with the set wavelength of the laser and then calculate the peaks in the recorded data. Regarding the power budget, the FBG interrogator of the tunable laser type has advantages over a wideband source interrogator, moreover all optical energy is focused into the very narrow spectrum of the laser source and thus no power is wasted. The performance of such an interrogator depends on the tuning speed and precision of the laser. Commercially available interrogators using this measuring principle currently employ External Cavity Laser (ECL), which are mechanically tuned. This causes significant costs and due to the mechanical tuning, interrogation speed is limited [72].

1.3.7 KLT Analysis Method

As shown above, most systems are based on a broadband light source and a spectrometer for detection. This approach provides long-term stability and is relatively inexpensive; on the other hand, the spectrum is sampled with a coarse wavelength resolution. A main alternative is represented by an interrogation system based on a scanning laser (or a scanning filter) and a photodetector: with this method, it is possible to have a denser sampling but it requires stable and isolated laser source, resulting in a more expensive system operating in a lower SNR. A method that estimates spectral shifts of FBG (FP and similar sensors as well) is needed in order to estimate the measurand. In literature, there are many papers introducing a new demodulation technique based on Karhunen-Loeve Transform (KLT) applied to the sensor spectrum [73]. The KLT is effective when in decoding the energy of the input signal and encoding the key information in its high eigenvalues [74].

Assuming an interrogation device based on a spectrometer, the latter discretizes the optical spectrum on wavelength and amplitude axes. The spectrum becomes a digital signal $S[\lambda]$ sampled with a uniform step $\delta\lambda$, the same for the amplitude. Adding the noise, it can be written:

$$S[\lambda] = R[\lambda] + N[\lambda] \tag{1.32}$$

where $R[\lambda]$ is the reflection spectrum of cascade of sensors, and $N[\lambda]$ is the noise defined as the ratio between R and N variances. Following Lamberti's approach, the next step is computing the FFT of the spectrum $S[\lambda]$:

$$G(f_1, \dots, f_N) = FFT\{S[\lambda_1, \dots, \lambda_N]\} \tag{1.33}$$

$G(\text{f})$ is then transformed into its symmetric Toeplits matrix $\overline{M}$. Taking $\overline{M}$ as input, the KLT is finally performed:

$$\overline{\overline{M}} = \overline{\overline{V}} x \overline{\overline{D}} x \overline{\overline{V}}^{-1} \tag{1.34}$$

where $\overline{\overline{D}}$ is a diagonal matrix containing all the eigenvalues of $\overline{\overline{M}}$ on its main diagonal, while $\overline{\overline{V}}$ is the corresponding orthonormal basis that contains on its lines the eigenvectors. The matrix $\overline{\overline{D}}$ contains the N eigenvalues that are real numbers since $\overline{\overline{M}}$ is symmetric. The eigenvalue array is called ξ and is sorted in ascending order. With this eigendecomposition it is possible to separate signal from noise: low-range eigenvalues, and their correspondent eigenvectors, are mostly affected by noise; high-range eigenvalues contain most of the signal energy [75].

Chapter 2: Arrayed Waveguide Grating

AWGs were already reported in late 80s by [76]–[78], known under other names: Phased Arrays (PHASAR), Waveguide Grating Routers (WGR) or the name used today Arrayed Waveguide Grating. Together with FBGs, these thin-film filters are the most commonly used in WDM networks. Nowadays the most employed technology for the realization of AWGs is silica-on-silicon (SoS) and Indiumphosphide (InP)-based technology. Furthermore, also study on Lithium Niobate and polymer technology are reported in literature [79], [80]. SoS AWGs have been holding the largest slice of market since 1994, due to the modal expansion which matches the one of a fiber, leading to an easier way to couple them into a fiber. They are characterized by low propagation loss (<0.05dB/cm) with a high fiber-coupling efficiency (losses in the order of 0.1dB) but are relatively large because of the fiber matched waveguide properties which impose the use of long bends as will be shown in next section. The latter disadvantage is being improved by using higher index contrast

AWGs can be employed to achieve many functionalities either in WDM networks for telecommunications environments, or as optical filter in signal processing, measurements and sensing as it was employed for the aim of this thesis.

The semiconductor-based devices show a great potential to integrate a huge variety of functions in a single chip, suitable for the integration of passive devices, as the AWGs, with active devices, also non-linear. In the field of telecom, the dominant technology is based on InP: the InP-based AWGs are very compact since the index-contrast is high. The market of optical integrated chips is expected to become increasingly important in the next decade.

2.1   AWG Working Principle

To an easier understanding of the working principle [81], the Figure 2.1 shows the schematic of an AWG. When a polychromatic light propagates through the transmitter waveguide entering into the first Free Propagation Region (FPR), it is no longer laterally confined and becomes a divergent beam. Arriving at the input aperture, the beam gets coupled into the waveguide array, propagating through the single waveguides towards the output aperture. The waveguide length is chosen in such a way that the optical path length difference between two adjacent waveguides is equal to an integer multiple of the central wavelength of the demultiplexer λ_C. For λ_C, the fields within the single waveguides arrive at the output aperture with the same phase and hence the field distribution at the input aperture is reproduced at the output aperture. The divergent beam into the FPR is thus transformed into a convergent beam with equal amplitude and phase distribution. Moreover, the input field at the object plane generates a corresponding image at the center of the image plane. The separation path length among different waveguides is given by linearly increasing the lengths of the arrayed waveguides, introducing a tilt of the output beam, function of the wavelength and linked to a shift of the focal point along the image plane. In a nutshell: if receiver waveguides are placed at a certain position along the image plane, different wavelengths will propagate towards different output ports.

2.1.1 The Free Spectral Range

The aim of this subsection is to give a theoretical model describing the characteristics of an AWG. As written before, the focusing phenomena of the fields propagating in the AWG structure, is achieved if the length difference ΔL between two adjacent waveguides is equal to an integer number m of wavelengths within the AWG:

$$\Delta L = \frac{m\lambda_c}{n_{eff}} \tag{2.1}$$
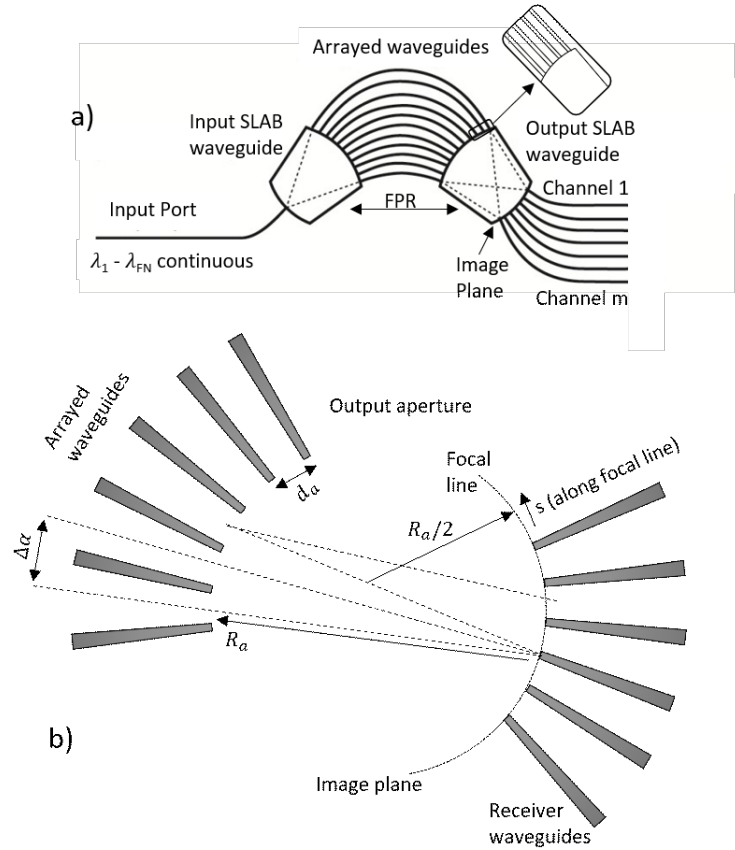
Figure 2.1: (a) illustration of an AWG, (b) beam propagation and focusing into the free propagation region.

where m is called the order of the array, λ_c is the central wavelength (in vacuum) of the AWG, n_{eff} is the effective refractive index of the modes propagating inside the structure (linked to the phase) and λ_c/n_{eff} gives information about the wavelength inside the arrayed waveguides. As depicted in this case study, the array works as a lens with image and object planes at a distance R_a of the array apertures. Furthermore, the focal line (defining the image plain) follows a circle with radius $R_a/2$ and transmitter and receiver waveguides must be located on this line.

The length increment ΔL of the array produces a phase difference

$$\Delta\phi = \beta\Delta L \tag{2.2}$$

where

$$\beta = \frac{2\pi v n_{eff}}{c} \tag{2.3}$$

is the propagation constant in the waveguides, $v = c/\lambda$ is the frequency of the wave propagating inside it and c is the speed of light in vacuum. The phase difference $\Delta\phi$ has a dependence on wavelength and introduces the wavelength-dependent tilt of the output wavefront associated with a wavelength-dependent shift of the correlated image.

The lateral displacement ds of the focal spot along the image plane per frequency change dv is called spatial dispersion D_{sp} of the AWG and can be obtained as [83]

$$D_{sp} = \frac{ds}{dv} = \frac{1}{v_C}\frac{n_g}{n_{FPR}}\frac{\Delta L}{\Delta\alpha} \tag{2.4}$$

where n_{FRP} is the slab mode index into the FPR, $\Delta\alpha$ is the divergence angle between the waveguides in the fan-in and fan-out sections, while n_g is the group index of the mode propagating inside the waveguide

$$n_g = n_{eff} + v\frac{dn_{eff}}{dv} \tag{2.5}$$

If the input wavelength variation is so that the phase difference $\Delta\phi$ between two adjacent waveguides increases by 2π, the propagation will be the same as before, that is, the operation of the AWG is periodic and the period is called Free Spectral Range. Imposing $\Delta\beta\Delta L = 2\pi$ in combination with (2.1) it can be calculated as

$$FSR = \frac{v_c}{n}\left(\frac{n_{eff}}{n_g}\right) \tag{2.6}$$

This is a very important parameter during the design of an AWG: to avoid crosstalk among the waveguides which may affects the working principle, the FSR should be larger than the whole spectrum range composed by the span of all channels. As an example, for a structure with 8 channels and 200GHz of spacing, the FSR should be 1600GHz at least. If the $\lambda_c = 1550nm$, the array order has to be about 120. Moreover, if the device is employed with the usage of Erbium-Doped Fiber Amplifiers (EDFA), the FSR has to be designed so that adjacent orders don't coincide with the peak of the EDFA, avoiding accumulation of Amplified Spontaneous Emission (ASE).

2.1.2 Non-Uniformity

Many loss phenomena are present, affecting the light propagating within the AWG. The highest contribution comes from the junctions between the FPRs and the arrayed waveguide. To get a lower loss, the fan-in and fan-out sections should work in such a way that a smooth transition from the propagation in the array to the FPRs is present and vice versa. This happens if $\Delta\alpha$ is small enough and the vertex among the waveguides is sharp in the right way. In the AWG production, since a finite resolution is present, the lithographical process blunting of the vertex will occur. For typical devices the junction losses are about 1 or 2dB per junction (between 2 and 4 dB for the total device). Losses due to a mismatch between the image field and the receiver waveguide, exhibiting a propagation loss and a coupling loss, are usually much smaller than the aforementioned one.

If T_c is the transmission coefficient of the central channel, the attenuation is given by

$$A_0 = -10logT_c \qquad\qquad (2.7)$$

Looking on Figure 2.2, it is shown how the other output channels present a higher loss value than the central ones. This is because the far field of the relative arrayed waveguide propagates in a different direction from the optical axis and the envelope is mainly determined by the far field radiation pattern. The non-uniformity ΔT_{AWG} is defined as
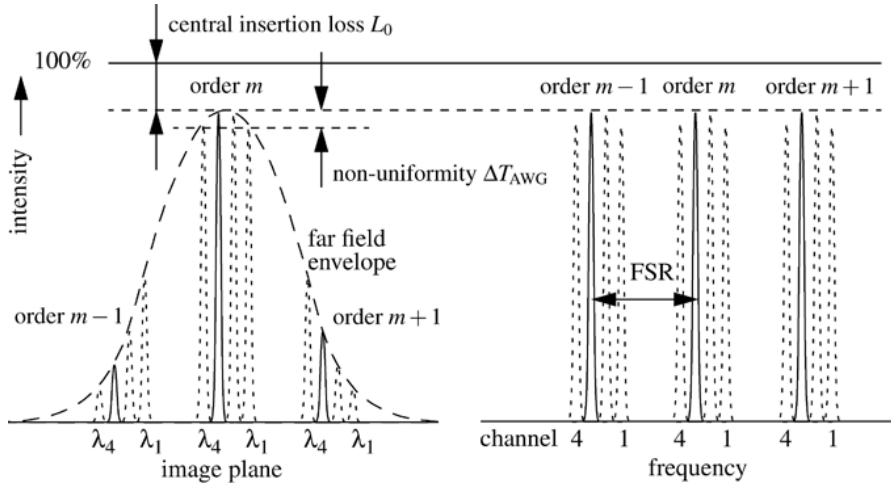
Figure 2.2: (left) affection of the far-field pattern into the image plane for different wavelengths; (right) representation of the Free Spectral Range [82].

$$\Delta T_{AWG} = -10 \log\left(\frac{T_{1,N}}{T_c}\right) \tag{2.8}$$

that is the difference in log between the farthest channels and the central one. The power lost from the main lobe is transmitted in adjacent orders as shown in Figure 2.2. If the FSR is N times the channel spacing, the external channels will exhibit 3dB more loss than the central channels. Hence, in this case, the non-uniformity is close to 3dB. This happens since at a deflection angle which corresponds to half of the angular distance between the orders of the array, the power over the image plane is reduced. From the foregoing, the non-uniformity of an AWG can be reduced increasing the FSR obtaining a larger device.

2.1.3 Coupling Behaviour

The AWG device works as a sort of lens, forming an image of the field pattern present into the object plane at the image plane. Due to its working principle it's unavoidable the exhibition of the dispersion phenomena: if the wavelength changes, the image will shift along the image plane without changing shape. AWG properties can be explained considering the coupling behavior of the focal field pattern in the image

$$U_r(s) \quad U_f(s - \Delta s)$$

$$\Delta s$$
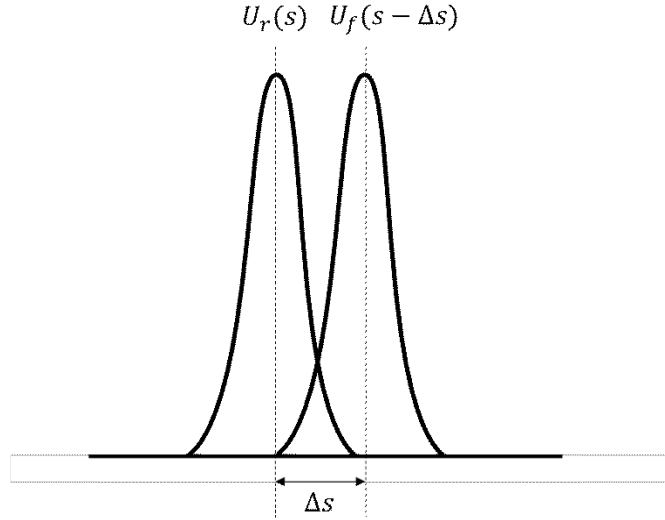
Figure 2.3: Superposition between a receiver waveguide profile Ur(s) and the focal field Uf(s).

plane to the receiver waveguide: the coupling is described by the convolution of the normalized receiver waveguide mode $U_r(s)$ and the normalized focal field $U_f(s)$ in the image plane (Figure 2.3):

$$\eta(\Delta s) = \left| \int U_f(s - \Delta s) U_r(s) ds \right|^2 \tag{2.9}$$

where Δs is the displacement of the focal field correlated to the receiver waveguide center. If $U_r(s)$ and $U_f(s)$ exhibit the same spectrum (if the same waveguides are used as transmitter and receiver) the coupling

$$\Delta s = D_{sp}(v - v_i) \tag{2.10}$$

in (2.9), obtaining

$$T_i(v) = T_c \eta D_{sp}(v - v_i) \tag{2.11}$$

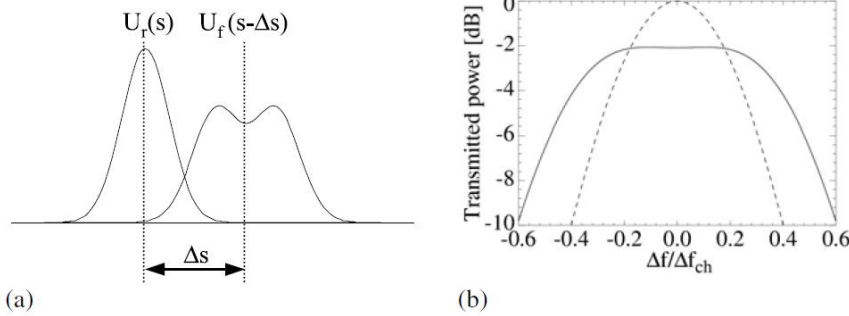**Figure 2.4:** Depiction of a method to get a flattening wavelength response: (a) superposition between the focal field Uf with the receiver mode Ur; (b) wavelength response obtained applying a camel-shaped focal field, while in dashed is indicated the response obtained with a normal focal field (Uf = Ur) [82].

where v_i is the frequency relative to the i-th channel. The power transmission T_c of the central channel is smaller than 1 since transmission losses are present in the AWG and it's worth to note that if an even channel number is present, there will not be present a waveguide at the center of the image plane. A more detailed analysis of the array imaging properties is reported in [84].

2.1.4 Flat Passband Shape

The passband shape is an important characteristic among the AWG features. The channel response has a Gaussian spectrum because of the mode profiles of the transmitter and receiver waveguides which can be well approximated by a Gaussian function. The overlap described by equation (2.9) is Gaussian as well. When employed into an optical system, the Gaussian shape may impose constrains on the wavelength tolerance of the input signal and requires an accurate temperature control for both AWG and the source (e.g. a laser diode). Furthermore, if signals are transmitted by means of WDM network, the passband width for the single channel becomes very narrow. Hence, flattened channel transmissions are an important feature for AWG when employed in de/multiplexer mode. Different studies were published, the easiest method is to use multimode waveguides at the receiver side. If the focal plane moves at the output of AWG along a wide waveguide, almost the whole amount of the light is coupled into the receiver to get

a flat region [85]. This latter approach is, on the other hand, adverse for single-mode systems. Another interesting approach is to convert the field at the transmitter or receiver into a double image (as depicted in Figure 2.4) obtaining a flat region given by the wavelength response which follows from the superposition of this field with the normal mode. The double image is created with a short MMI coupler [86], with a Y-junction [87] or a non-adiabatic parabolic horn [88]. Other studies are based on spatial filtering inside the AWG exciting a sinc-like field distribution at the grating exit producing, via Fourier transform, a rectangular shape [89], [90]. Also using interleaved gratings or phase-dithering [91], [92] it is possible to obtain the same result. As disadvantage, these techniques increase the insertion loss (of about 3dB) since only a portion of the image is focused onto each waveguide output. This effect can be mitigated combining the AWG with a MZI-duplexer at the input [93], [94]. This is the most important characteristic about the AWG for the discussion of this thesis: the flat part of the AWG spectrum, employed as demultiplexer/filter into the proposed interrogation system, may affect the Bragg wavelength detection when this latter shifts from an AWG channel to another. Further details will be given in chapter 3.

2.1.5 Crosstalk

An inter-channel crosstalk is present: it is represented by the contribution of unwanted signals (e.g., adjacent channels) plus the contribution of signal at a frequency (i+1) next to the channel (i) detected. The theoretical explanation behind this phenomenon is that the adjacent-channel crosstalk A_x is dependent on the superposition between the focal field and the unwanted mode
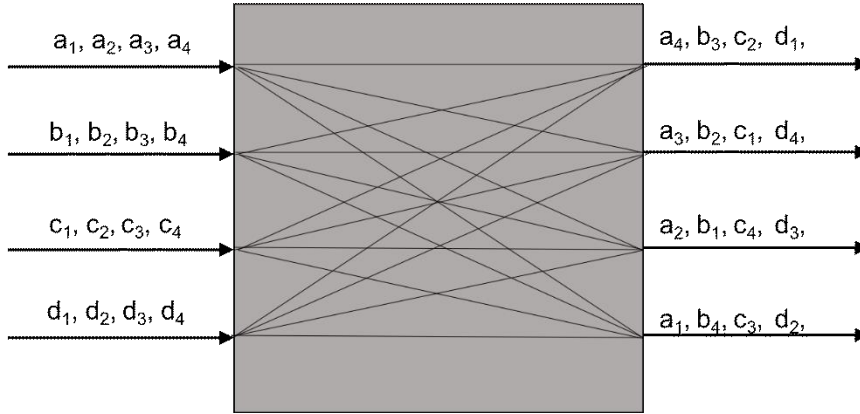
Figure 2.5: Working principle of a wavelength router.

$$A_x = \eta(d) \tag{2.11}$$

where d is the distance between adjacent waveguides. Hence, from the formula (2.11), it is possible to attenuate the crosstalk positioning the receiver waveguides far apart. Two times the wavelength width is typically enough for 40dB crosstalk attenuation. Other mechanisms are present limiting the crosstalk attenuation: due to non-uniformities in layer thickness, waveguide width and refractive index, causing a noise floor better than 35dB for good devices. Other considerations on the AWG crosstalk are discussed in [95].

2.1.6 AWG as Wavelength Router

Is now reported an application of employment for the AWG device as a wavelength router. If the AWG is designed with NxN input/output waveguides and with an FSR equal to N times the channel spacing, the device behaves cyclical: a signal entering into the input channel N will appear at the output 1. This is called cyclical wavelength router [78] and plays a key role in add-drop multiplexer systems or wavelength switches in telecom environment. Figure 2.5 shows the working principle: the N frequencies carried by input 1 are propagated among output channels 1 to N in a way that the output channel 1 is the image of frequency N and channel N gives the image of frequency 1. From the input 2, signals are distributed in the same way but shifted by 1 channel.

2.1.7 Thermal Behaviour and Athermal AWGs

Since the AWG is composed by a few arrayed waveguides, the center wavelength of each channel is depending on the temperature. The main effect due to temperature variation is the change of wavelength response. InP-based AWGs have a temperature coefficient of 0.12nm/°C, implying few nanometers of wavelength shifting for a change of 30-40°C; SoS-AWGs exhibit a temperature dependence which is smaller than the previous one (order of one magnitude) but still too high for uncooled operations. A way to obtain temperature insensitivity is by acting at the process level inserting a triangular region with different temperature sensitivity material into the FPR. The same technique is used for polarization insensitivity [96].

It's worth to introduce the Athermal AWG as case study since the experimental analysis conducted in the next chapters, were done employing a temperature insensitive AWG. In SoS-based AWGs, the relation between center wavelength and temperature is

$$\frac{d\lambda}{dT} = 1.2 \ 10^{-2} nm/K \tag{2.12}$$

which can also be written as $dv/dT = -1.5\text{GHz/K}$ in terms of frequency at 1550nm. This number is determined by the temperature variation of the refractive index in the silica glass which is $\frac{dn}{dT} = 1.1 \ 10^{-5} K^{-1}$. In typical applications, AWGs are stabilized with temperature control (e.g., Peltier element) but the control adds additional circuitry, hence complexity, at the system. The idea is to avoid the extra effort employing athermal AWG exhibiting flat filter response over a temperature range of 0-85°C. The realization of an athermal AWG relies on the substitution of a standard waveguides section with waveguides made of negative dn/dt material in order to compensate the total temperature dependence [97]. A material usually employed for this purpose is silicon which is characterized by $\frac{dn}{dT} = -37 \ 10^{-5} K^{-1}$. With this high number, only the 3% of silica waveguide path has to be replaced by silicon. Due to the scattering interface between silica and silicon. the insertion loss get raised by 2dB which can be reduced at 0.4dB by segmenting a trapezoidal silicon region into

multiple groove regions [98]. Polymer are utilized as well for the compensation of temperature-induced variation, while other approaches based on tracking the AWG focal points are presented [99]–[101].

2.2   AWG-Based Interrogation Technique

Due to its intrinsic characteristics, the AWGs seems to be the right choice, during the design of an interrogation system, to have a fully passive, without movable part and solid optical circuit for the wavelength detection of the FOS. As mentioned before, the AWG exhibits a Gaussian spectrum at the output channels, with the possibility to discriminate the sensor wavelength just monitoring the right channel which is related to a certain central wavelength. The AWG is able to discretize a spectrum and easily reveals what is the wavelength position of the sensor under test. Thanks to this kind of working principle, this device is not only employable as demultiplexer in telecom environment, but it is more and more used for sophisticated solution in the field of wavelength detection, not only for FBG sensors, but for every FOS whose spectrum is contained within that of the AWG. In this paragraph many solutions are reported, focusing on the AWG-based interrogation system for FBG sensors, with the aim to give an introduction to the analysis conducted in this thesis.

2.2.1 Extrinsic Fabry-Perot Interferometer Sensor Interrogation

One of the first papers employing AWG as key device for the interrogation of FOS was published in 2002 by P.Niewczas [102]. A solid-state interrogation system based on a 16-channel AWG was used as a spectrometer to detect the back reflected light from the sensor which, in this case, is an Extrinsic Fabry-Perot Interferometer (EFPI). The measurement points are then fitted reconstructing the original spectrum of the sensor.
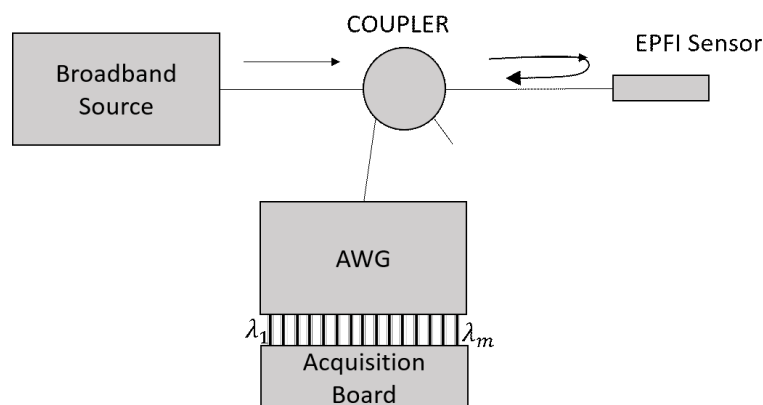
Figure 2.6: Block diagram of the EFPI-AWG interrogation system.

The proposed concept is depicted in Figure 2.6 and is composed by: a Super Luminescent Diode (SLD) as source; the FPI sensor; an optical circulator and the AWG connected to a photodetector array and a data acquisition board. Knowing the expression of the EFPI reflectance, it is possible to calculate the optical power detected by means of the single photodetector at the generic monitored AWG output channel by integrating the AWG transmittance with the sensor reflectance and the source spectrum. Through the data acquisition preceded by a calibration procedure, a linear sensor response was acquired, validating also numerical simulations.

2.2.2 Space-to-Wavelength Mapping with AWG for Wavelength Detection

In a more recent work published by H. Guo in [103], [104] a novel technique for the FBG interrogation is presented. The technique is based on a space-to-wavelength mapping employing an AWG device by controlling the beam position along the AWG with a piezoelectric motor. The experimental setup is shown in Figure 2.7 can be described
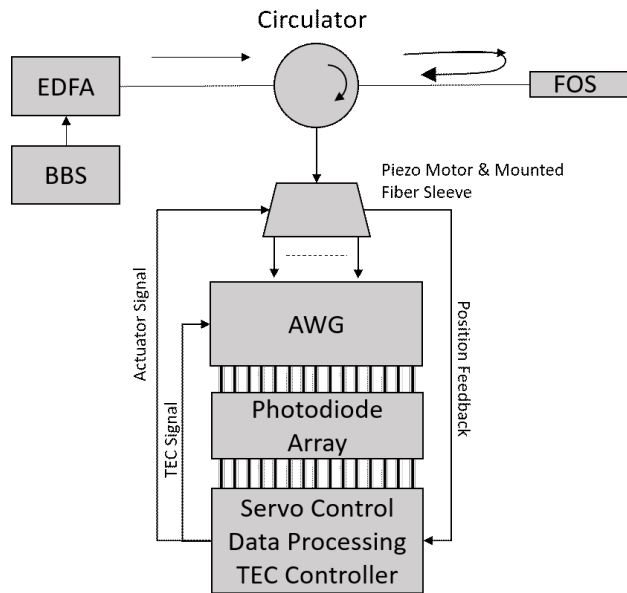
Figure 2.7: Setup of the interrogation technique proposed in [104] based on a space-to-wavelength mapping employing a piezo motor and an AWG device.

as follows: a BBS generating the light beam, amplified with an EDFA, propagates towards the FBG by means of an optical circulator. The circulator output is mounted on top of a closed-loop piezo motor pre-aligned with the input coupler of the AWG with the help of a positioning stage. A capacitive position encoder is embedded into the close-loop piezo motor to get information about the position feedback, when the motor moves horizontally driving the fiber tail and scanning the input coupler. With a position feedback, the piezo motor is set to reach the specified position. A thermal electrical cooler is also employed to mitigate the AWG temperature dependence. The output channel provides to the photodetector array a signal which can be manipulated via software to measure the Bragg wavelength shifting at a maximum speed of 16kHz. The proposed technique needs no additional wavelength reference and has a high potential to be competitive on the market since is easy to miniaturize it in a light and cost-efficient system.
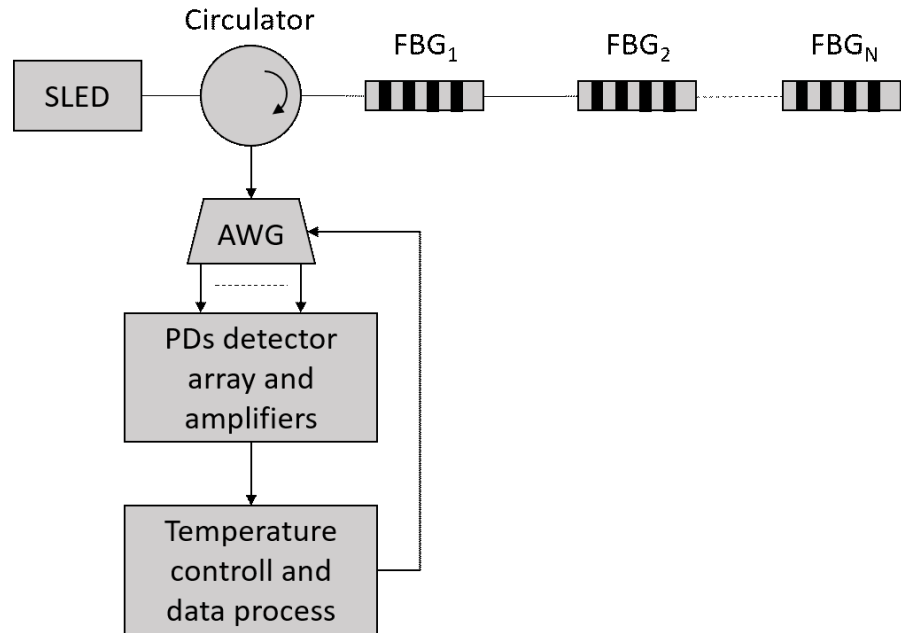
Figure 2.8: AWG-based interrogation system using a tunable temperature control.

2.2.3 AWG Temperature Tuning for FBG Interrogation

In a study presented by W. WU [105], the temperature dependence affecting AWG devices is used as modulator for the interrogation of FBG sensors. As widely discussed in this chapter, the AWG center wavelength increases monotonically with the silica waveguide temperature. This means that, tuning the device temperature, is possible to change opportunely the AWG center wavelength. With the proper schematic depicted in Figure 2.8 it is possible, designing an FBG array with each response peak close or equal to those of AWG output channel, to measure the Bragg wavelength shifting by using the wavelength tunability. The interrogation technique is based on the spectrum overlapping: if at a temperature T1 the peak wavelength of the generic output channel does not overlap the FBG spectrum, the optical power detected at the output channel will be low. If the AWG temperature raises, the peak wavelength of the monitored channel shifts towards the FBG wavelength until, a certain temperature T2, the two spectra perfectly

overlap obtaining the maximum optical power in output. From experimental analysis the technique is promising and may obtain a resolution in the pm range. The number of FBG under interrogation depends on the AWG characteristics.

2.2.4 Output Power Ratio Interrogation Algorithm

On the same line of the work reported in section 2.2.1, in literature are present few works [106]–[108] in which an algorithm is used for the Bragg wavelength detection. The algorithm is based on an analytical approach of the devices composing the system which is very light, employing only passive and rough devices: a SLED source, an optical circulator, an FBG array and the AWG connected to the electrical/digital section (Figure 2.9).

Since the FBG has a Gaussian spectrum, as well as the output channels composing the AWG device, the output optical power is given by the integration within the generic AWG output channel spectrum between FBG reflectance and the AWG output channel transmittance. The integral argument is, hence, the multiplication of two Gaussian functions, which is another Gaussian function of the two originals. The resultant Gaussian function get maximum if the Bragg wavelength is positioned at the peak wavelength of the related output channel and get minimum if the Bragg wavelength is far away. Taking into account the same function relative to the adjacent channel, is possible to combine the optical power of the two adjacent output channels, called interrogation function, and calculate the Bragg wavelength in linear dependence with it.

As illustrated in [106], when the Bragg wavelength is exactly at the middle between two AWG output channels, the interrogation function get null. Increasing or decreasing in function of the FBG shifting. The dynamic range of interrogation is given by the AWG channel spacing and it is clear that, to get the maximum possible, the FBG interrogated has to lie where the interrogation function is zero. If an AWG has a channel spacing of 800pm, the maximum achievable dynamic range is 400pm (400pm if Bragg wavelength increase and other 400 if decreases). It's clear that the AWG channel spacing imposes a certain dynamic range while the AWG bandwidth is related to the sensitivity, as reported in [108].
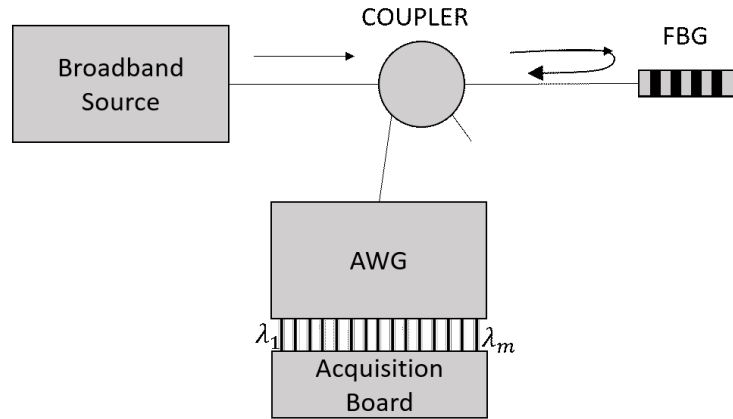
Figure 2.9:Schematic of an AWG-based interrogation system for FBG sensors employing adjacent channels power ratio algorithm.

The interrogation function has a slope depending on the AWG channel bandwidth: the lower is the AWG channel bandwidth value, the higher is the sensitivity of the system. By what just written it appears as a trade-off between the dynamic range and the system sensitivity exists, that will be well explained in chapter 3. In another work reported in [110], [111] a multichannel algorithm may be employed with a lower AWG channel bandwidth to overcome the aforementioned trade-off and get higher sensitivity.

The theoretical approach is based on many assumptions which are very difficult to meet in the real cases: the Gaussian spectrum about AWG and FBG is an example. In the real scenario, the devices are not perfectly Gaussian and the AWG parameters are not equal for every output channel.

As will be shown in the next chapter, many non-ideality errors affect the result of this interrogation system, further decreasing the dynamic range (due to non-linearity effect) and increasing the measurement error. In [109], [112] a look-up table approach, to increase the measurement accuracy, and also a performance analysis with simulations on measurement process are presented; while in [113] it is illustrated a method to increase the capability of FBG interrogated with a single AWG-based interrogation system.

The strength of the algorithm is that the ratio between the optical power of two adjacent output channels totally neglects every loss

affecting the system: source fluctuation, attenuation by connectors, noises and so on. The system presents many features that can be further improved in order to design an interrogator which is attractive on the market, being low cost, highly maintainable, reliable (all passive devices are employed), without control signal or movable part. In the next chapter a detailed section on the algorithm will be dedicated, as well as numerical and experimental analysis, from the optical and electrical point of view, on a proposed technique to overcome the limitation of the interrogation technique and exploit the main characteristics of the AWG to get an interrogation concept performing a high frequency wavelength detection with a multichannel algorithm approach.
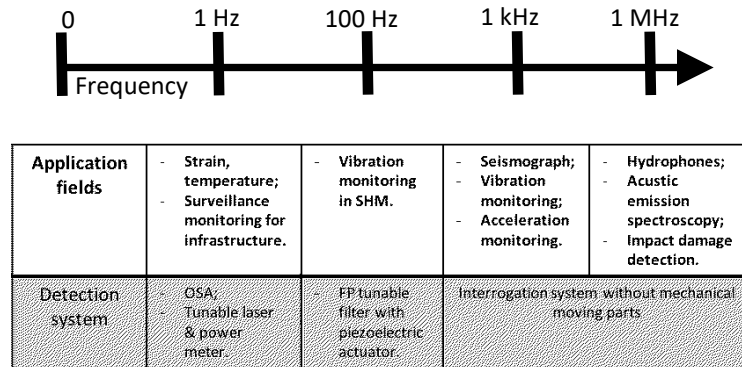
Chapter 3: High Speed Multichannel AWG-based Interrogator

The advancement in technology is based on different physical phenomena that are possible to monitor due to specific sensors. Among a large number of different technologies, in the last decades, the research is focusing more and more on Fiber Optic Sensors technology (FOS). Particularly on Fiber Bragg Grating sensors (FBG) which, as already discussed in chapter 1, work as an optical filter with a Gaussian reflectance characterized by a central wavelength called Bragg wavelength [14], [16], [114] which changes with temperature or strain variation. As passive and dielectric they are characterized by electromagnetic immunity that, together with other advantages, make them very suitable in a wide range of environments where other kind of sensors cannot be employed.

At the state of art, since the FBG is small and with the possibility to have plenty of sensors on the same optical fiber, many studies are reported in the field of Structure Health Monitoring (SHM) [115]–[118] for example the vibration monitoring of high building or bridges to name a few. In a more recent work [119] some FBG were used in microsurgery field since the material from which they are made is biocompatibility and there is no presence of electrical current flowing through the sensor (passive element). The key strength of this sensor is the possibility to manipulate the temperature and strain dependence to many other physical quantities. Manipulating the fiber coating and with a calibration fit it is possible to employ a simple FBG as a humidity sensor [120], for radiation monitoring [121] and for cryogenic measurements in superconducting accelerators [122]. It's worth to name other important work in the field of high energy physics: where other kind of sensors may result invasive, or exhibiting low reliability and sensitivity, the employment of FBG seems to be the right choice [123]–[125]. As already said a FBG sensor can be installed in environments with harsh boundary condition and/or hard to reach for other kind of sensors, this is possible since the interrogation system is installed in a safe place also very far to the sensor section (up to

kilometers). The interrogation apparatus, actually, is the true fulcrum of a monitoring system based on FOS technology: the system sensitivity, speed, reliability and the robustness as well are characteristics about the optoelectronic circuit interrogating one or multiplexed FOS. An interrogation system is, usually, composed by a light source, passive elements for the irradiation of the signal, one or more optical devices for the reflected wavelength discrimination, an electrical section for the acquisition and an algorithm for the manipulation of data. The light source can be a broadband spectrum or a tunable laser. In this latter case the light source is modulated in time leading to change in in wavelength and the detection algorithm is based on the span time when the wavelength reflection occurs. This kind of interrogation has high accuracy but also a higher cost, with a limit on the speed (best performances on static measurement).

In a lot of works [126]–[129] many changes in either the optoelectronic section or the detection algorithm were conducted, in some cases employing filter which needs a control signal limiting the speed and the robustness. Among the innovations, the Arrayed Waveguide Device (AWG) seems to well substitute any kind of active optical filter leading to have better performances. The AWG is mainly produced for fiber optic telecommunication since it offers an important Dense Wavelength Division Demultiplexing (DWDM) increasing the communication system capacity. Furthermore, with specific fabrication techniques, it is possible to achieve a device completely insensitive to the temperature variation (Athermal AWGs) avoiding the usage of external temperature controller [101]. As written in the previous chapter, the working principle is to split an incoming light into its constituent colors playing the role of an integrated prism and can be employed as filter in an interrogation system since it is a robust and reliable device, detecting the FOS central wavelength if contained within its spectrum. Since it is passive, it is possible to increase the operation frequency of the designed system, which will be dependent only on the electronics and the data processing employed, allowing the monitoring of physical phenomena in the range of MHz with a competitive price on the market. Many papers were published on the AWG-based interrogation system[105]–[108], [130], [131] that, in a way or another, highlight the disadvantages of employing this device: the FOS (the FBG in these case studies) has to

| Application fields	- Strain, temperature; - Surveillance monitoring for infrastructure.	- Vibration monitoring in SHM.	- Seismograph; - Vibration monitoring; - Acceleration monitoring.	- Hydrophones; - Acustic emission spectroscopy; - Impact damage detection.
Detection system	- OSA; - Tunable laser & power meter.	- FP tunable filter with piezoelectric actuator.	Interrogation system without mechanical moving parts	

Figure 3.1: Wavelength detection system in function of application field and variation of the physical phenomenon.

be positioned exactly in the midway between two adjacent channels to have the best dynamic range available. In this paper a new multichannel algorithm is presented, overcoming the abovementioned disadvantage, with the aim to have a modular dynamic range for the AWG-based interrogation system and with an electrical component working in the order of MHz. The details of this work, with some experimental results, are described within this chapter.

3.1 Analytical Approach

The proposed concept depicted in Figure 3.1 can be described as follows: a broadband source (BBS) generates a light propagating towards one or more FBG by means of a circulator. The FBG works as an optical filter, reflecting a little part of the light propagating towards it while the remaining part is transmitted without losses. Thus, the reflected signals, containing information about the physical quantities to detect, propagate towards the AWG device with the task to be separated in many output channels depending on the correlated wavelength. Each output channel is connected to an electrical module converting the optical power to a voltage which is then acquired by a digital board and processed with a detection algorithm.
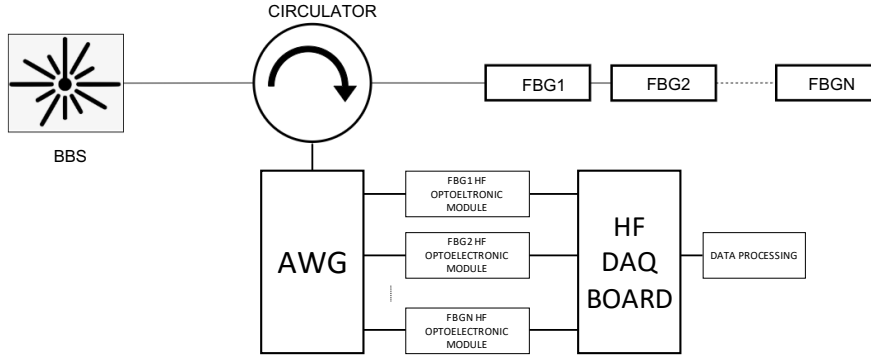
Figure 3.2: Schematic of the proposed concept.

3.1.1 Interrogation Algorithm

In In this case study here considered, the FOS is an apodized FBG (without side lobes) which can be modeled, Reflectance spectrum, with a Gaussian shape (considering the background noise and other minor effects to be negligible) with order *n* as follows:

$$B(\lambda) = b_0 \exp\left[-\left[\frac{(\lambda - \lambda_b)^2}{2c_b^2}\right]^n\right]$$

(3.1)

where b_0 is the FBG peak reflectance, λ_b is the central Bragg wavelength while c_b^2 is linked to the bandwidth (Full Width at Half Maximum) as follows:

$$FWHM = 2\sqrt{2\ln 2}\ c$$

(3.2)

The AWG Transmittance of the generic output channel *m* can be described with a Gaussian shape of order *p* as well and, as the previous case, the background noise can be considered as negligible:

$$A_m(\lambda) = a_{0m} \exp\left[-\left[\frac{(\lambda - \lambda_{am})^2}{2c_{am}^2}\right]^p\right]$$

(3.3)

where a_{0m} is the AWG peak transmittance about the generic output channel *m*, λ_{am} is the central wavelength of the same output channel while c_{am}^2 is linked to the bandwidth (FWHM) as before.

The output voltage is produced by the generic m output channel. acquired by the electrical module characterized by a certain gain and containing a photodetector with a certain Responsivity. Furthermore, it is the integration in the whole AWG output channel spectrum, in which the BBS signal can be defined as constant in wavelength since its spectrum is much wider than the AWG output channel one:

$$
\begin{aligned}
V_m(\lambda_b) \\
= a_{0m} b_{0m} \, R \, G \, S \int_\lambda d\lambda \exp\left[-\left[\frac{(\lambda - \lambda_b)^2}{2c_b^2}\right]^n\right] \exp\left[-\left[\frac{(\lambda - \lambda_{am})^2}{2c_{am}^2}\right]^p\right]
\end{aligned}
\tag{3.4}
$$

where R is the photodiode responsivity, G is the transimpedance amplifier gain and S is the optical power irradiated by the BBS. The result follows approximating the Gaussian with order 1:

$$
\begin{aligned}
V_m(\lambda_b) &= \frac{a_{0m} b_{0m} \, R \, G \, S \, c_{am} b_0 \sqrt{\pi}}{\sqrt{2}\sqrt{(c_b^2 + c_{am}^2)}} \; exp\left[-\left[\frac{(\lambda_b - \lambda_{am})^2}{2(c_b^2 + c_{am}^2)}\right]\right] \\
&= C_m exp\left[-\left[\frac{(\lambda_b - \lambda_{am})^2}{2\Delta_m}\right]\right]
\end{aligned}
\tag{3.5}
$$

which is depending on λ_b.

Considering two adjacent output channels with a voltage V_1 and V_2 is defined the interrogation function:

$$
\begin{aligned}
F_{12} &= \frac{V_1/C_1 - V_2/C_2}{V_1/C_1 + V_2/C_2} \\
&= \frac{exp\left[-\left[\frac{(\lambda_b - \lambda_{a1})^2}{2\Delta_1}\right]\right] - exp\left[-\left[\frac{(\lambda_b - \lambda_{a2})^2}{2\Delta_2}\right]\right]}{exp\left[-\left[\frac{(\lambda_b - \lambda_{a1})^2}{2\Delta_1}\right]\right] + exp\left[-\left[\frac{(\lambda_b - \lambda_{a2})^2}{2\Delta_2}\right]\right]} \\
&= \tanh\left(\frac{\left[-\left[\frac{(\lambda_b - \lambda_{a1})^2}{2\Delta_1}\right]\right] - \left[-\left[\frac{(\lambda_b - \lambda_{a2})^2}{2\Delta_2}\right]\right]}{2}\right)
\end{aligned}
\tag{3.6}
$$

which means:

$$F_{12} = \frac{V_1/C_1 - V_2/C_2}{V_1/C_1 + V_2/C_2} \tag{3.7}$$

$$= \tanh\left(\left[-\frac{(\lambda_b - \lambda_{a1})^2}{\Delta_1} + \frac{(\lambda_b - \lambda_{a2})^2}{\Delta_2}\right]1/4\right)$$

since ideally the bandwidth of each output channel are Δ_1 and Δ_2 we can approximate it by their average $\Delta_{12} = (\Delta_1 + \Delta_2)/2$.

The equation becomes:

$$F_{12} = \frac{V_1 C_2 - V_2 C_1}{V_1 C_2 + V_2 C_1} = \tanh\left(\frac{2\lambda_b(\lambda_{a1} - \lambda_{a2}) + (\lambda_{a2}^2 - \lambda_{a1}^2)}{4\Delta_{12}}\right) \tag{3.8}$$

where λ_b is:

$$\lambda_b = \frac{\mathrm{atanh}[F_{12}]\,2\Delta_{12}}{(\lambda_{a1} - \lambda_{a2})} + (\lambda_{a1} + \lambda_{a2})1/2 \tag{3.9}$$

The eq. (3.9) can be used for the Bragg wavelength detection only when the FBG spectrum lies within the AWG window composed by channel 1 and channel 2. If the FBG exhibits a wavelength shifting along more than two adjacent channels, the eq. (3.9) has to be modified in order to take into account terms about other windows. A method to match the Bragg wavelength calculated in the window 1 (channel 1 and 2) with the one calculated in window 2 (channel 2 and 3) is given by the following summation:

$$\lambda_b = \sum_{i=1}^{num\ channels} \left\{ \left[\frac{\mathrm{atanh}\left[\frac{V_i C_{i+1} - V_{i+1} C_i}{V_i C_{i+1} + V_{i+1} C_i}\right]2\Delta_{i,i+1}}{(\lambda_{ai} - \lambda_{ai+1})} \right.\right. \tag{3.10}$$

$$\left.\left. + (\lambda_{ai} + \lambda_{ai+1})1/2 \right] V_i V_{i+1} \right\} / \sum_{i=1}^{num\ channels} V_i V_{i+1}$$

3.1.2 Algorithm Consideration

It is seen from equation (3.8) that the interrogation function vanishes when λ_B is in the midway between two adjacent channels;

furthermore, λ_B is in a form as $\lambda_B = F\alpha + \beta$, in linear relationship with the interrogation function F, allowing an easy detection of the FBG wavelength.

Due to the aforementioned linear dependance, the sensitivity of the wavelength interrogation is given by the trend of F against λ (shown in Figure 3.3). The slope can be determined through the term α, which depends on the inverse of the term $\Delta_{i,i+1}$ as it is shown in eq. (3.10). The term $\Delta_{i,i+1}$ is function of the AWG and the FBG bandwidth since it is directly linked to $\Delta_{ai}^2 + \Delta_{FBG}^2$. This means that increasing the AWG bandwidth, the dynamic range of interrogation will increase, but the measurement sensitivity will decrease. A trade-off between sensibility and dynamic range is present. This is shown in Figure 3.3 where the λ_B is changing between 1552.6 and 1553.4 nm, completely inside the window 1 between AWG channel 1 and 2 with a frequency spacing of 0.8 nm. It is shown that the F_{12} is null at 1553 nm, that is exactly the middle frequency between the two channels. One of the key strengths of this interrogation system is that the aforementioned trade-off does not affect the wavelength detection: the interrogation function can be extended ideally along the whole AWG spectrum, which means that for a low AWG channel bandwidth value, thus increasing the sensibility, the dynamic range can be increased employing more channels. The FBG wavelength is not limited within one window between two adjacent channels, but it can also shift into other channels. The detection is performed due to an iterative algorithm of the interrogation function. Furthermore, losses due to connectors, noise due to devices and other parameters that can affect the measurement are avoided.
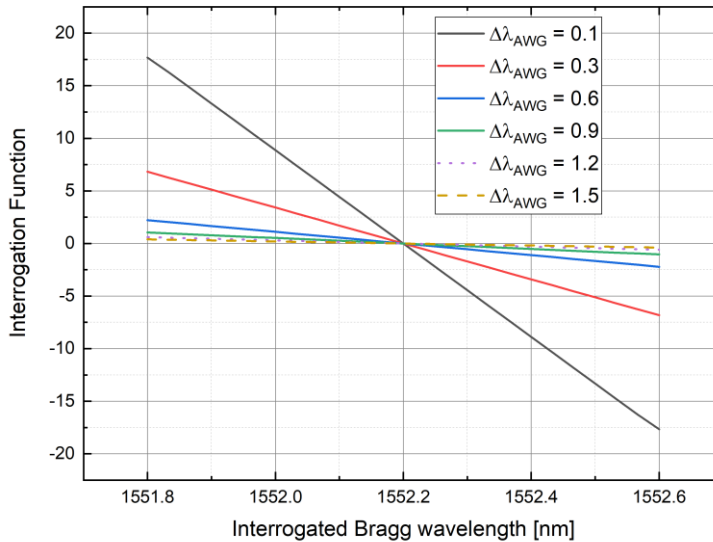
Figure 3.3: Interrogation function variation versus FBG wavelength for different AWG channel bandwidth values.

3.1.3 Analytical Validation

With the aim to confirm the interrogation algorithm and understand which parameter may affect the system, a validation through MATLAB software was led. As depicted in Figure 3.4, a linear Bragg wavelength shifting was assumed within two AWG windows: the window 1 between channel 1 and 2; the window 2 between channel 2 and 3. The AWG was assumed with a frequency spacing of 0.8nm and a channel FWHM of 0.6nm while the FBG is characterized by 0.2nm of bandwidth. By a first analysis, assuming FBG reflectance and AWG transmittance with a Gaussian spectrum of order 1, the calculated voltage output is Gaussian as well (Figure 3.5).

The interrogated Bragg wavelength obtained from simulation is shown in Figure 3.6 in which an interesting result is also depicted: if the AWG channel bandwidth is equal for each of the three channels, the Bragg wavelength shifting matches with the interrogated one (with a mean error value ideally null); if a discrepancy between the channel FWHM exists, the interrogated Bragg wavelength exhibits a different trend than the original one.
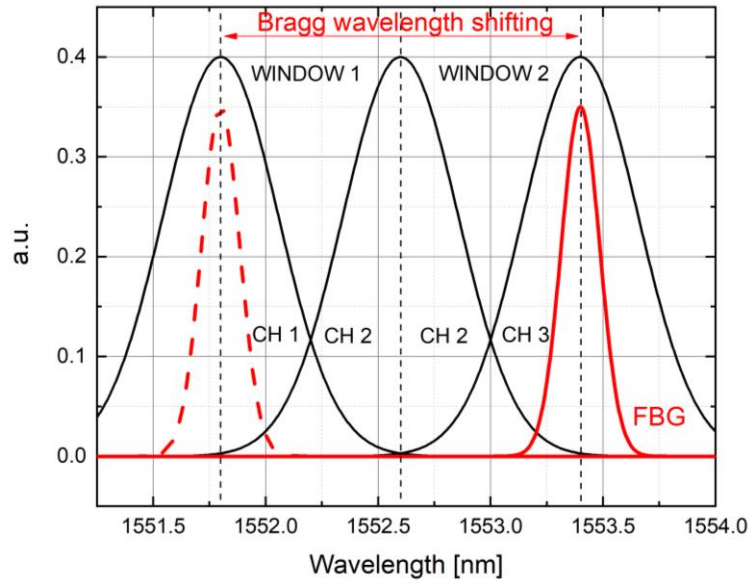
Figure 3.4: Bragg wavelength linear shifting among three ideal AWG output channels, between two windows.
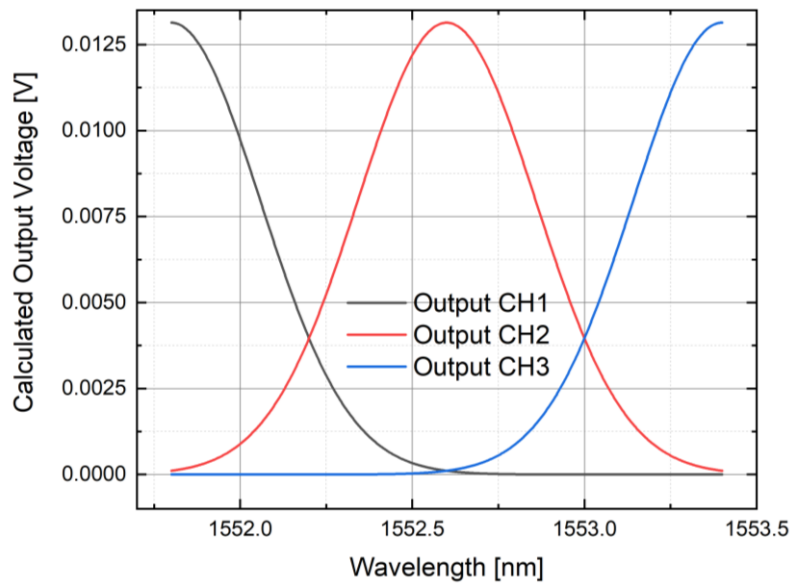
Figure 3.5: Output voltage calculated assuming a Gaussian spectrum for the AWG and FBG spectrum.
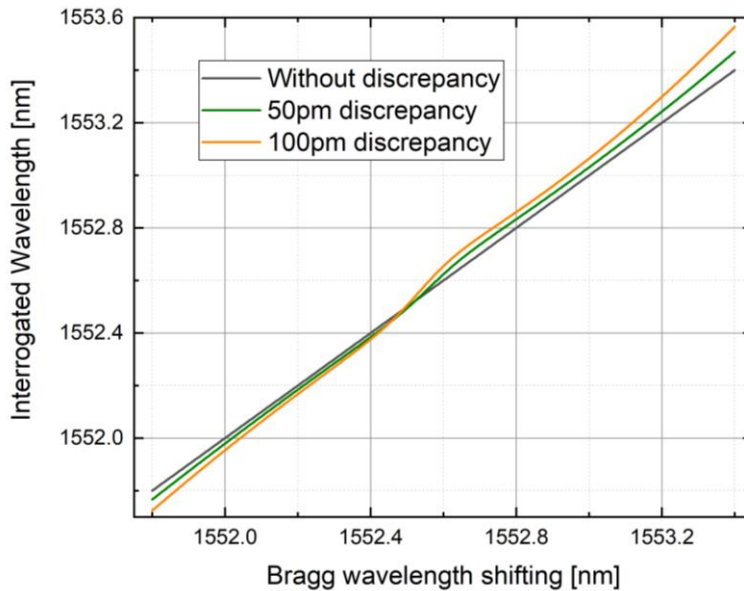
Figure 3.6: Interrogated Bragg wavelength against wavelength shifting for two discrepancy values of the AWG channel FWHM.

In Figure 3.6 a green shape with a discrepancy of ∓ 50pm ($\Delta_{CH1} = 0.6, \Delta_{CH2} = 0.55, \Delta_{CH3} = 0.65$) and an orange shape with a discrepancy of ∓ 100pm ($\Delta_{CH1} = 0.6, \Delta_{CH2} = 0.5, \Delta_{CH3} = 0.7$) are depicted. The mean error between the interrogated wavelength by the algorithm and the original linear shifted is about 11pm for the ∓ 50pm and about 26pm for the ∓ 100pm. This analysis was mandatory to do since in equation (3.7) the FWHM of AWG channels was assumed to be ideally equal. Apparently, a measurement error exists and is proportional to the bandwidth discrepancy among the AWG channels.

A second analysis was conducted on the assumption of Gaussian spectrum for the AWG transmittance. In Figure 3.6 it is represented the calculated output voltage for an AWG and an FBG modeled with a Gaussian filter with an order of 1.2. Although the output spectrum seems to be very close to the order 1, in Figure 3.7 the interrogated Bragg wavelength is shown: without any bandwidth discrepancy (in black) and with the two discrepancies of the case mentioned before (green and orange).
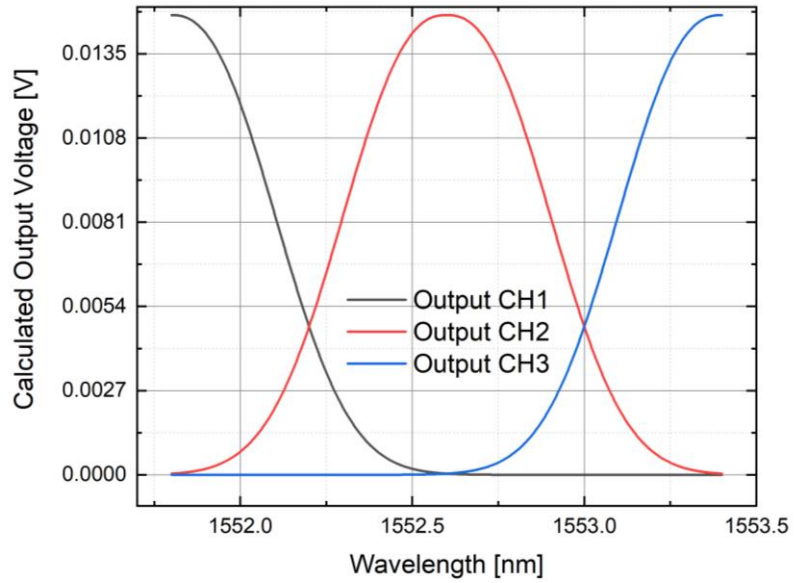
Figure 3.7: Output voltage calculated assuming a Gaussian spectrum with an order of 1.2 for the AWG and FBG spectrum.
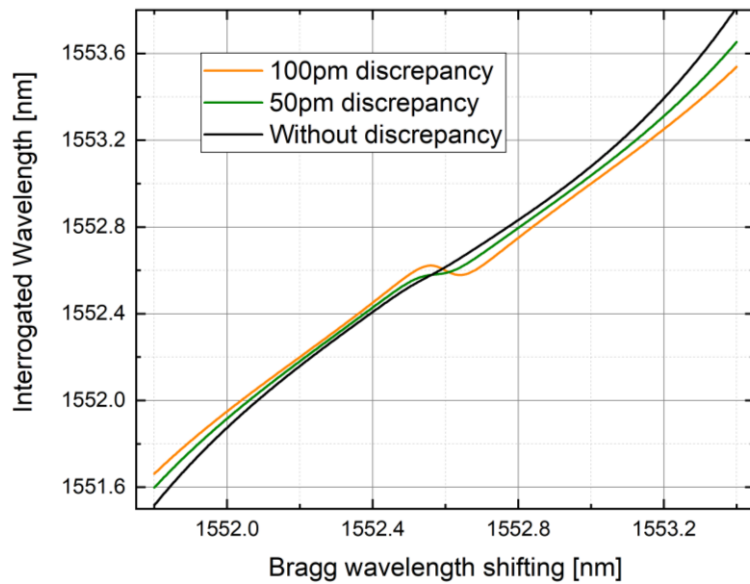
Figure 3.8: Interrogated Bragg wavelength against wavelength shifting for two discrepancy values of the AWG channel FWHM considering a Gaussian order of 1.2.

Even without discrepancy the interrogated wavelength is far away to be linear as the original wavelength shifting and a lot worse combining the discrepancy. From this study it appears that the intrinsic characteristics of the AWG which will be employed for the experimental analysis plays a key role for the measurement error of the final system. While parameters such as: AWG ripple, crosstalk and insertion loss are not affecting the system, the FWHM and the Gaussian model have to be as close as possible to the one of the ideal AWG to get a more performant interrogation.

3.2   Numerical Simulation

Numerical simulations were performed using specific software that handle easily optical and electrical system including noise and fluctuations that are avoided in the theoretical model, to express the results as real as possible. The aim was to validate the analytical approach of the interrogation system, extending the wavelength detection along three AWG output channel, simulating devices with real parameters. The design of an electrical circuit for the conversion of the optical power from the generic AWG output channel is demonstrated as well.

3.2.1 Optical Simulation

The study was performed with the software Optisystem, which is able to simulate both optical and electronic devices constituting the system under development. The software contains a variety of optical devices including the AWG and FBG. This latter has also the possibility to be modified in terms of apodization and chirping.

The schematic simulated shown in Figure 3.9 is composed from:
- A light source which is a LED with a power of 22mW, peak wavelength of 1555nm, bandwidth of 60nm and a flat spectrum extended for the whole AWG spectrum (Figure 3.10).
- An optical circulator with an insertion loss of 0.7db per path.
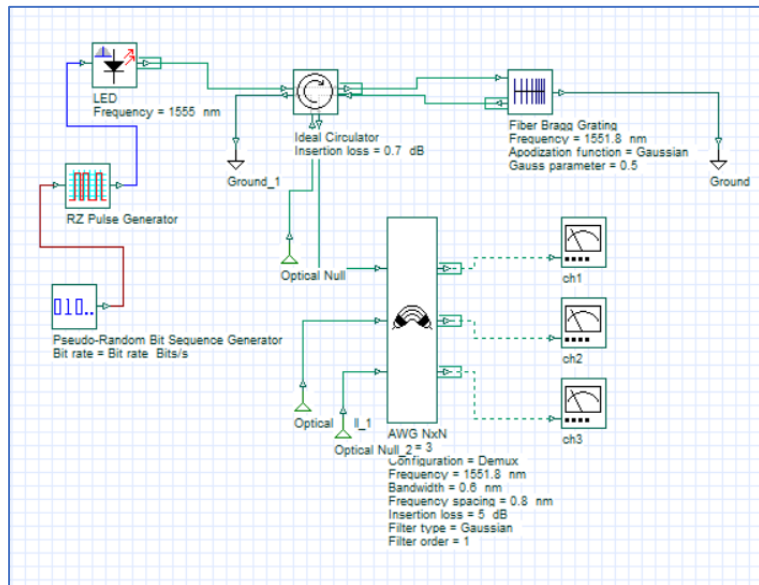
Figure Errore. Per applicare 0 al testo da visualizzare in questo punto, utilizzare la scheda Home.**9:** Schematic block of the simulated system with the software Optisystem.

- An FBG performing a linear shape in 25 points, shifting its Bragg wavelength from the maximum of AWG channel 1 to

     the maximum of AWG channel 3. The spectrum is apodized, without side lobes and with a Gaussian trend; the reflectivity is over 90%, simulating an FBG of a length of 1cm and a FWHM of 150pm (Figure 3.11).
- An AWG 1x3 in demultiplexer mode with a channel spacing of 0.8nm, a channel bandwidth of 0.6nm, a starting frequency (channel 1 peak) of 1551.8 and an insertion loss of 5dB. The filter type is first order Gaussian.
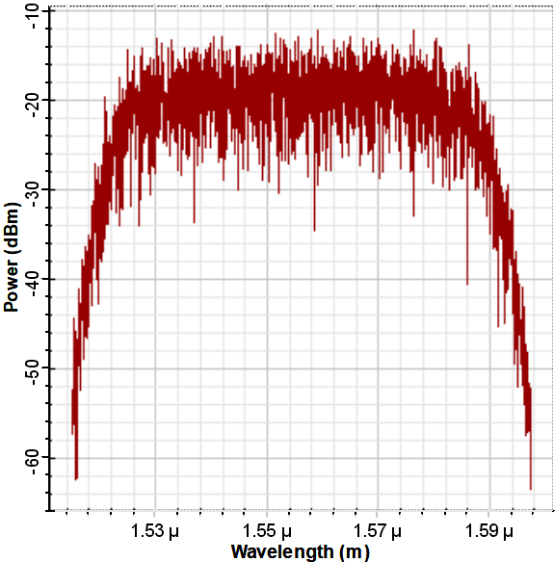
Figure 3.10: Broadband source spectrum.
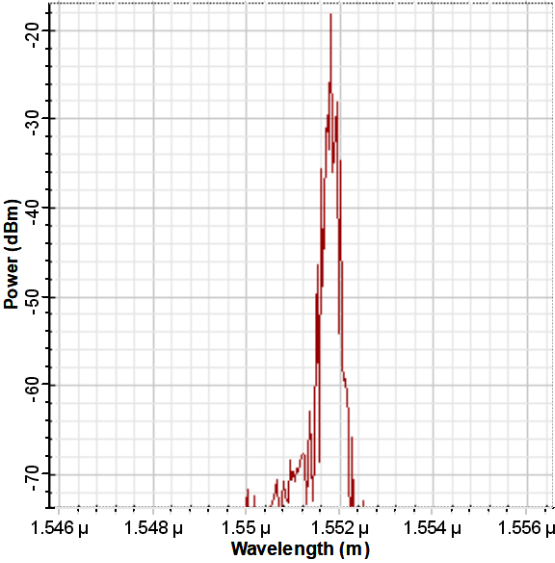

Figure 3.11: Back reflected signal spectrum from the FBG.
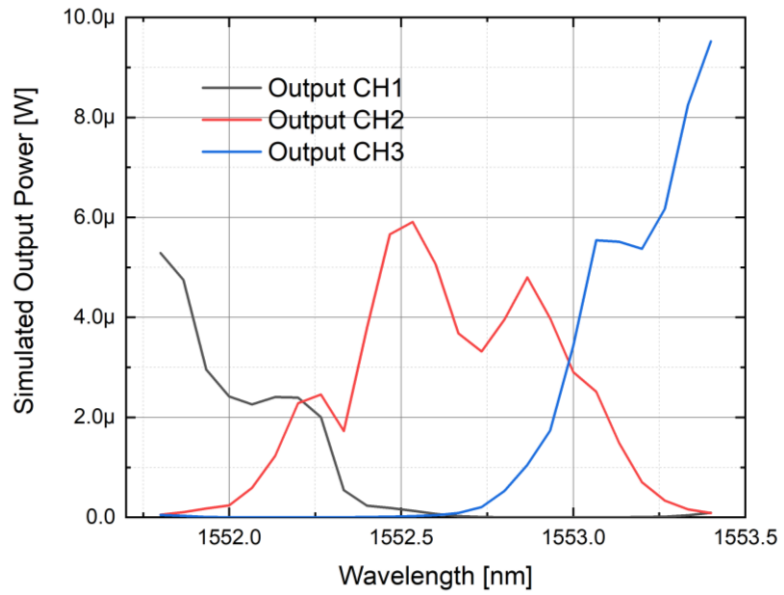
Figure3.12: AWG output power by numerical simulation.
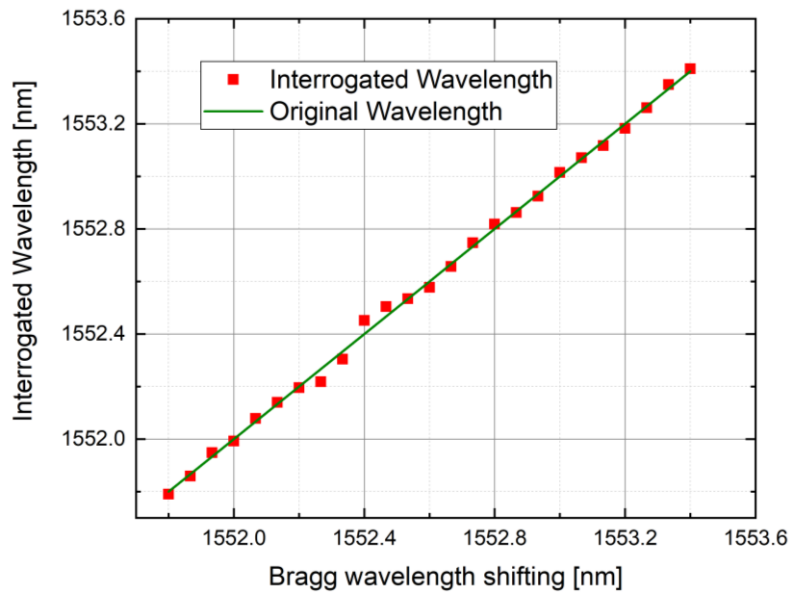
Figure 3.13: Interrogated wavelength performed by the proposed algorithm with simulated power.
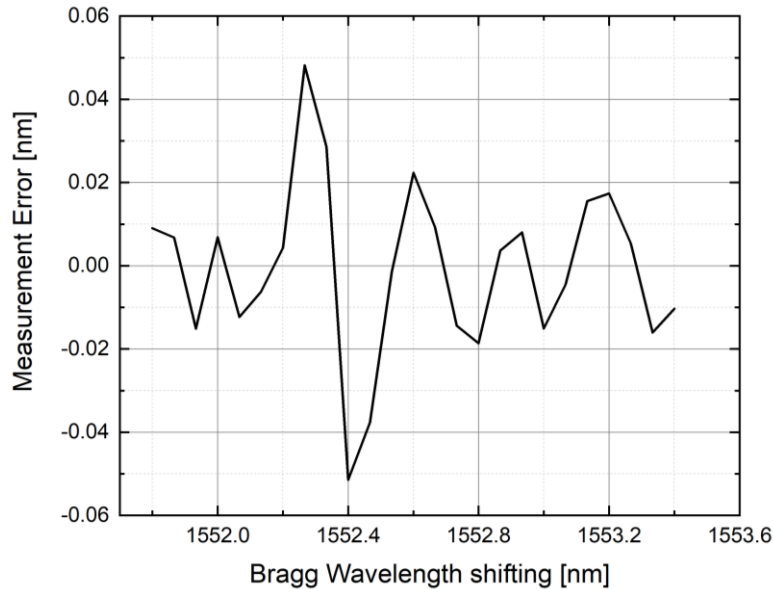
Figure 3.14: Measurement error between the original Bragg wavelength shifting and the interrogated one through numerical simulation.

In Figure 3.12 the output power by AWG channels is represented. The spectrum is very noisy due to the high ripple of the light source and the FBG reflectance which is not apodized at 100%. Nevertheless, as depicted in Figure 3.13, the interrogated wavelength, calculated with the proposed algorithm, is quite close to the original Bragg wavelength shifting. This demonstrates the peculiarity of the proposed concept which rejects the fluctuations: the source ripple does not affect the measurement. In Figure 3.14 the error value is shown: from a maximum of 6pm to a minimum of 0, this error is given by the FBG whose spectrum is not perfectly Gaussian. However, the mean error value is in the sub-picometer order. From the optical point of view, the numerical simulations gives an encouraging result confirming the theoretical aspects.

3.2.2 Electrical Simulation

As shown in the previous analysis, the Arrayed Waveguide Grating is definitely the most important device in the interrogation system: from its characteristics, the sensitivity and reliability of the

interrogator are defined. The proposed system is also composed of an electrical part which has the task to convert the information stored in an optical signal, to an electrical one and cannot be ignored for the correct working of the whole interrogator. For this reason, electrical consideration must be done as well.

The design begins by modeling the photodiode and the way to use it: for this application, in which the aim is to design a circuit working at about 5 MHz, the speed and so the photoconductive mode is necessary. In Photoconductive mode the photodiode is biased (typically with -5 V or, for simplicity, with the negative bias of the operational amplifier), this increases the dark current but reducing the parasitic capacitance and, thus, increasing speed and responsivity (SCR zone wider, hence more photons absorbed). The photodiode chosen is made of InGaAs material in order to absorb photons in C band (1550 nm), with these characteristics:

- 2 GHz response;
- 20 pA dark current at -5 V;
- 0.95 A/W responsivity at -5 V;
- 1 pF parasitic capacitance at -5 V.
- 3 x 10^{-15} W/$\sqrt{Hz}$ Noise Equivalent Power.

These values are needed to simulate the photodiode in the circuit analysis that follows. Due to the parasitic capacitance, photodiodes provide an output current at high impedance (high at DC). If this current flows into a resistor to generate a voltage, two problems will come: if high gain is needed, a large resistor is needed as well reducing the response, hence increasing time-constant; with a small resistor, the gain is lower, increasing the speed, but the signal to noise ratio (SNR) might be unacceptable. The solution is to feed the photodiode's output current into the summing point of a transimpedance amplifier. Now the response time is independent from the photodiode parasitic capacitance, allowing to use large resistor for high gain and improving SNR too. The two stages (depicted in Figure 3.15) include a first transimpedance amplifier in inverting configuration for current to voltage conversion, then a RC filter and a buffer to decouple the device downstream. The gain is directly determined by Rfeedback. The instability, that could also affect a simple configuration of an operational amplifier if the delay created by amplifier's input capacitance reacts with the feedback resistance, may represent an issue. This can be avoided moving the pole
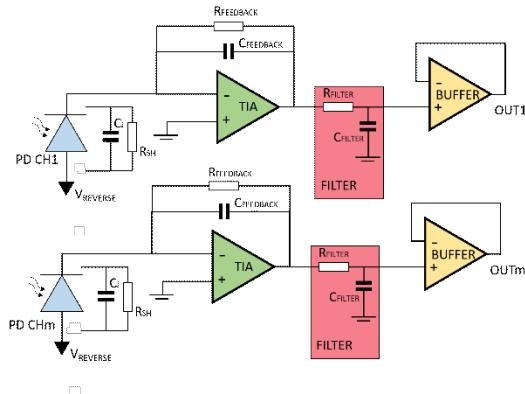
Figure 3.15: Schematic of the electronic section conditioning the signal coming from AWG channel to interrogate a single FBG.
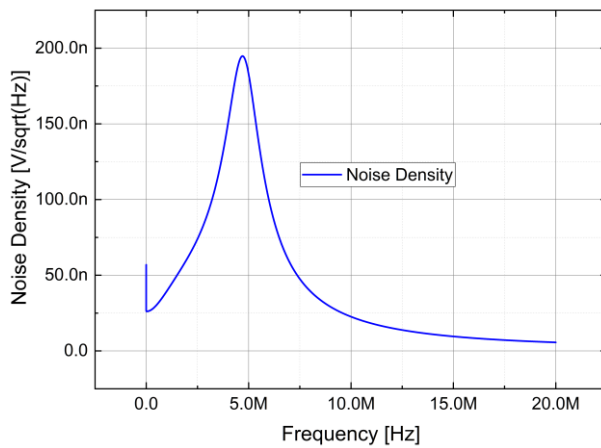
Figure 3.16: Noise density simulation of the electronic section.

created at higher frequency or deleting it with a zero. The best solution is to connect a feedback capacitor Cfeedback in parallel with Rfeedback limiting the frequency response and avoiding gain peaking that can lead to overshooting. In Figure 3.16-19 some analyses follow: noise density simulation, Bode diagram, stability simulation and a pulse response to show the characteristics of the designed circuit. The operational amplifier chosen is the LTC6244HV by Analog Devices, with a low bias current (1pA), low input capacitance (2.1pF) and with a high Gain Bandwidth Product (GBP) (50MHz). The gain was chosen to be 33k
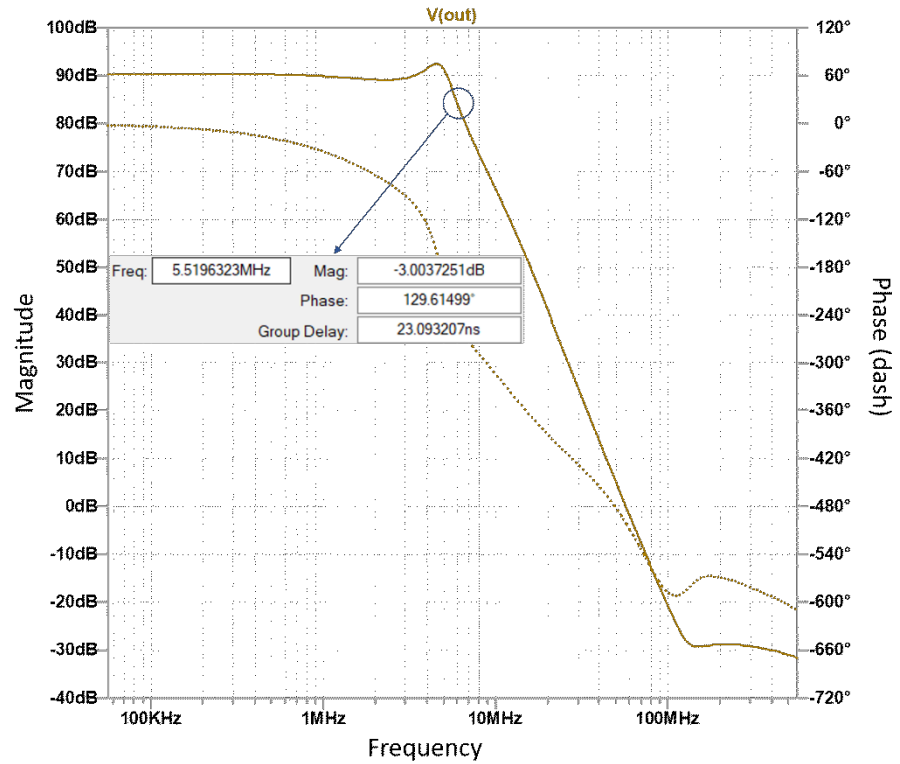
Figure 3.17: Bode diagram of the electronic circuitry. The 3-dB bandwidth is about 5.5MHz.

since the output power expected is in the order of few micro watt (in the case of FBG with 0.2nm FWHM), a maximum voltage of about 1V is far away from the noise level and is well enough for the algorithm process. The feedback capacitance is of 2.4pF, which gives a right balance between the 3-dB bandwidth (from the Bode diagram 5.5MHz) and the stability given by the pulse response (exhibiting an overshooting of 1%) and the margin calculation. The margin stability analysis states a phase margin of 58° and a gain margin of 1.6dB.

Figure 3.18: Stability analysis through phase and gain margin calculation.

Figure 3.19: Stability analysis through pulse response simulation.

3.3   Experimental Results

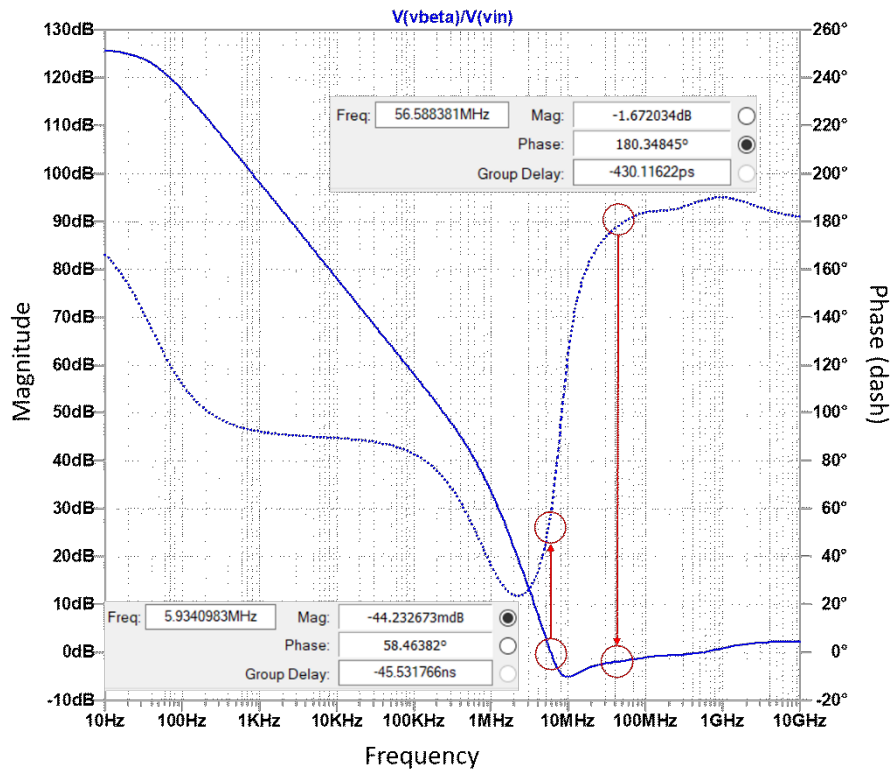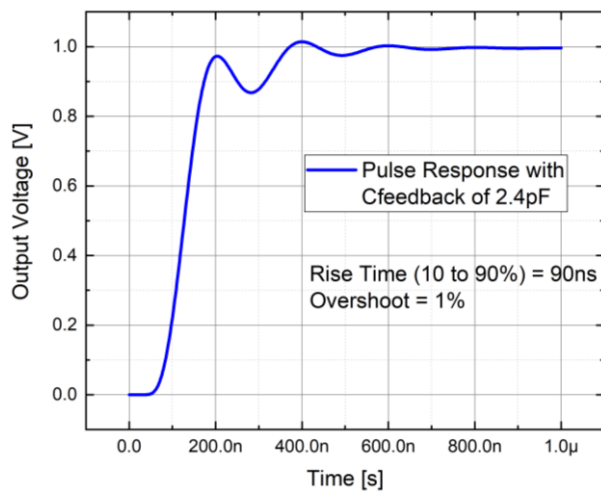For the experimental measurements, an AWG was employed (the characteristics are well described in the appendix section). The first analysis has the aim to validate the theoretical and numerical simulations, investigating the AWG spectrum and the limits of the interrogation algorithm.

3.3.1 Real Devices Spectrum Analyses

The detection algorithm presented in paragraph 3.1.1 is based on some ideal hypotheses which may not be fully satisfied in the actual situation. An example is given by the AWG and FBG employed for a first experimental analysis: in Figure 3.20 the whole AWG spectrum is shown with the superposition (in red) with an apodized FBG characterized by 180pm of FWHM. The declared (by the manufacturer) channel spacing is 0.8nm while the channel bandwidth is 0.6nm. For the tests and elaborations, a first order Gaussian was used to model the single AWG channel Transmittance spectrum, instead of a second order which, as it is depicted in Figure 3.21, seems to be closer to real. The same in Figure 3.22 for the FBG. Theoretically, this may lead to an accuracy decrease. with a flat response when the Bragg wavelength is crossing from a window to another. The conceptual problem mentioned above are related to FBG characterized with very narrow bandwidth with respect to the AWG channel. From a spectral point of view, it happens because of the FBG reflectance, positioned on the channel peak, that is so narrow to not integrate the transmittance of adjacent channel. This consideration involves a lower limit for the bandwidth of FBG that can be interrogated while the upper limit is given by the AWG channel one.

From (3.9) it seems that it is possible to increase the sensitivity of the system choosing an AWG device with the right bandwidth (lower bandwidth means higher accuracy). At the state-of-art, this trade-off leads to a significant decrease of the dynamic range. With the proposed multichannel algorithm, it is possible to employ an AWG with lower bandwidth value without loss in terms of dynamic range since it is possible to use multiple consecutive "windows".
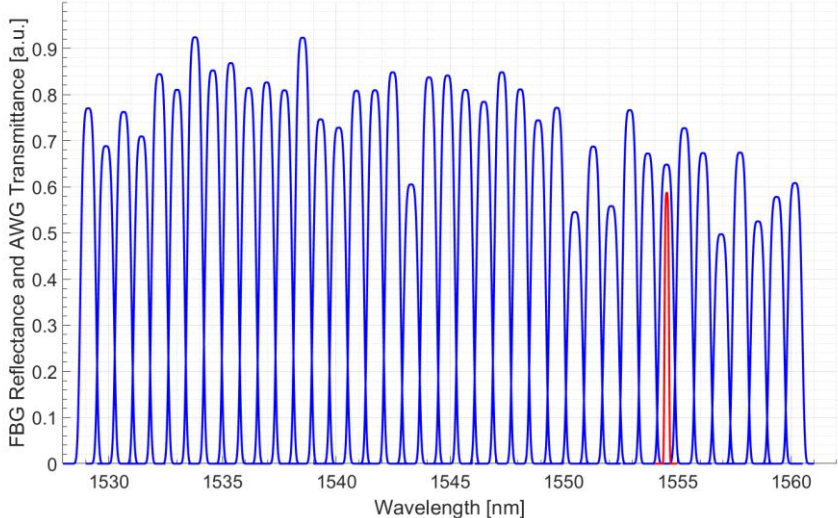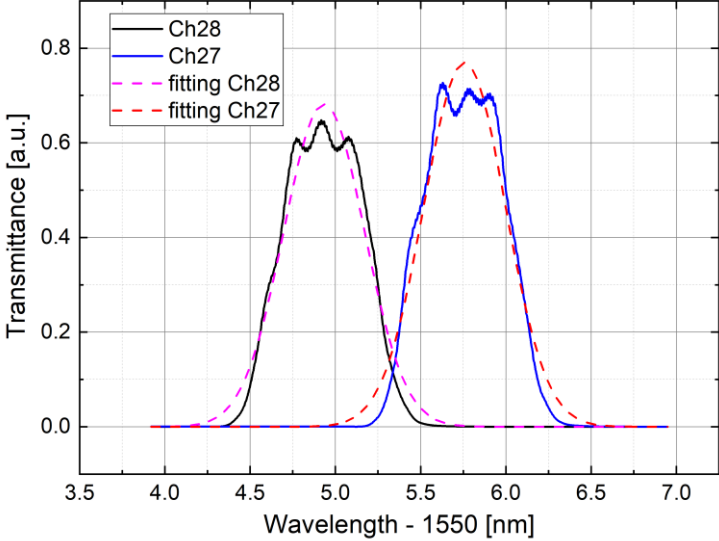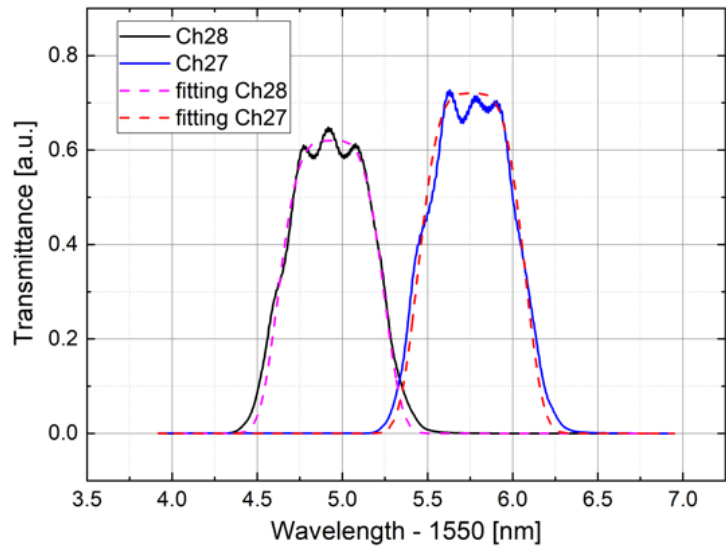
Figure 3.20: AWG employed spectrum with the superposition of an FBG (in red).

(a)

(b)

Figure 3.21: First order Gaussian fitting of channel 27 and 28 (a). Second order Gaussian fitting (b)
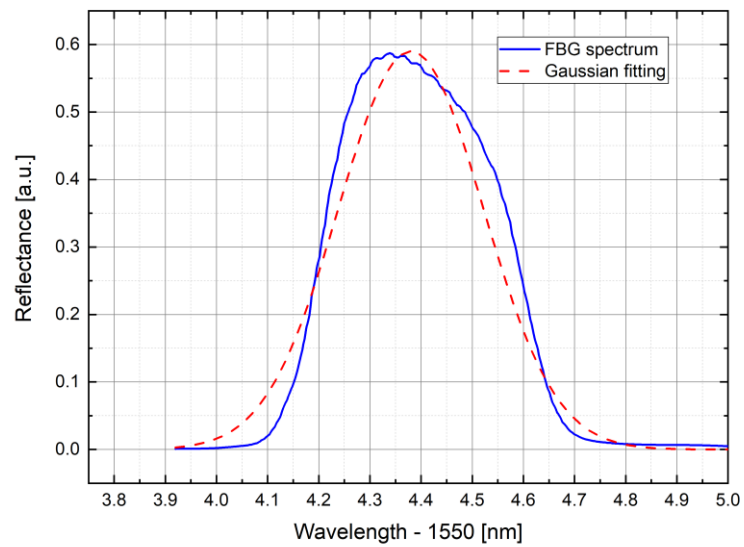
Figure 3.22: Magnified view of FBG with first order Gaussian fitting.

3.3.2 Linearization of the Interrogation Function

In a real case, the interrogation system presents some phenomenon which may affect the wavelength detection: optical noise, electrical noise and, above all, the non-ideal spectrum of the optical devices, produce an amount of optical power at the AWG channel output, overlapped with the FBG signal.

Trying to quantify how this noise can affect a wavelength detection, a measurement with the FBG illustrated in Figure 3.22 performing a wavelength shifting between two AWG channels (illustrated in Figure 3.21 in which a comparison between a first and second order Gaussian fitting is represented) was done. The employed source is a SLED characterized by 40nm of bandwidth, central wavelength at 1550nm and an output power of 16mW; the optical circulator exhibits an insertion loss of 0.7 per path; the photodetectors utilized are InGaAs photodiode from Throlabs with a gain of 10k through a simple resistor. The Bragg wavelength was shifted due to temperature variation by means of a heat plate, between the central peak of AWG channel 28 and the central peak of AWG channel 27. In Figure 3.23 the output optical power and the relative interrogation function are showed. This latter is not linear as expected since exhibits a curvature at the initial and final part of the spectrum due to the non-ideality noise mentioned above. According to [106] it is possible to measure the non-ideality noise (with an OSA or a high gain photodiode) and subtract the obtained value (called linearization factor J) from the AWG channel optical power monitored. The interrogation function of Figure 3.23b while changing J is shown in Figure 3.24. The best linearization is given by subtracting a power of 0.13uW at the output of channel 28 and 27. The high noise region (highlighted by Figure 3.25) is due to electrical noise which gives value close to 0, producing high value of the interrogation function due to the hyperbolic arctangent. The phenomena get furthermore worse with the subtraction of J. Ad-hoc electronic circuitry with low noise mitigates the effect as is shown in the next paragraph.
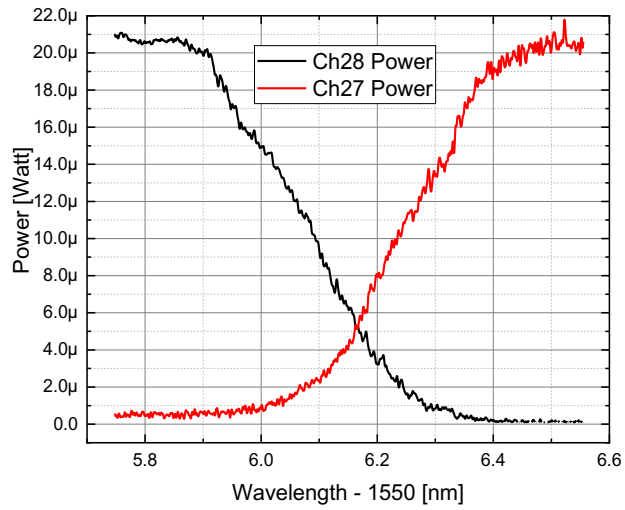
(a)
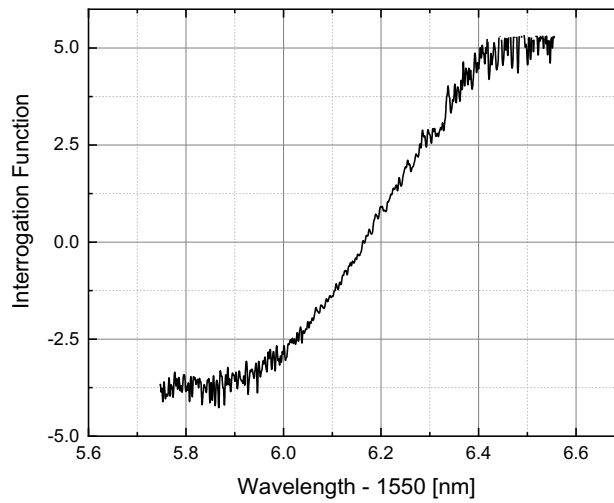
(b)

Figure 3.23: (a) output power from AWG channel 28 and 27 performed by a linear Bragg wavelength shifting; (b) related interrogation function.
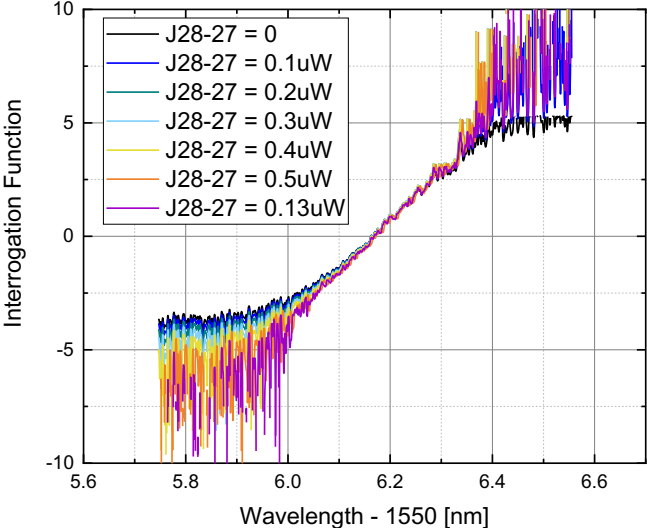
Figure 3.24: Interrogation function changing the linearization factor J..
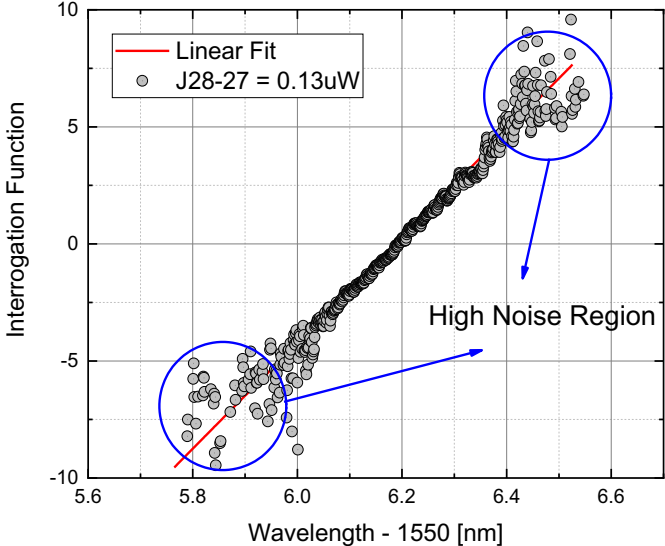
Figure 3.25: Interrogation function linearized with a linear fitting.

3.3.3 Measurements and Results

In this paragraph the results obtained from experimental measurements led in static and dynamic variations are reported.

- In order to achieve equivalent static experimental characterizations, temperature solicitation was sensed by using three FBG having three different FWHM values. The aim of this experimental analysis is to prove that the interrogation capability with the proposed system is not depending on the FBG bandwidth. This peculiarity represents an advantage since, in most of the employed interrogation systems (e.g., based on tunable laser) the higher is the FBG bandwidth, the lower is the measurement accuracy. Furthermore, high-bandwidth FBG are less expensive and usually show a Gaussian trend of Reflectance closer to the first order.

- As dynamic experiments, the system was tested by using high frequency strain stresses and an FBG glued on an Aluminum plate in order to prove the feasibility. A first vibration test was sensed in the range of hundreds of Hertz by hitting with the plate, while, in a further measurement, a pressure signal generated by a piezoelectric probe, in order to test the interrogation in the MHz range, was sensed as well. The goal of these experiments was to prove that with the proposed optical components, in which passive devices are employed, the proposed concept is able to behave as the currently used interrogation system, also working in applications (as the high-frequency detection) in which the well assessed tunable filter-based interrogators are not suitable due to the limits on the read-out and numerical elaboration speed.

As reported in section 3.2, the AWG channel spectra are much better modelled by using a second order Gaussian which, if handled in a different algorithm, gives a system of equations without presenting analytical solutions. To overcome this problem, a possible remedy may be given by a look-up-table approach as in [109], although this latter involves onerous data processing. In the proposed experimental analysis, the first order algorithm explained in section 2 was employed, approximating both AWG Transmittance and FBG Reflectance spectrum as first order Gaussian. To mitigate and overcome the non-
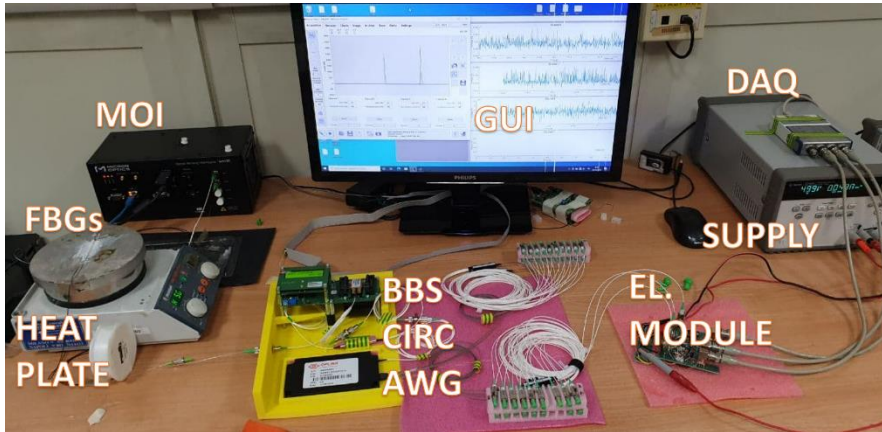
Figure 3.26: Illustration of the measurement setup.

ideality error given by the approximation imposed, some corrections were applied:

• An offset voltage given by the system noise were compensated.

• A furthermore compensation was done subtracting a little amount of voltage to every analog output which represents the crosstalk noise among the AWG channels.

• After a proper calibration, a slope correction was done minimizing the error between the interrogated Bragg wavelength and the spectrum position in the three well known wavelength values.

3.3.3.1 Temperature Measurements

In these kind of tests, three FBG sensors were interrogated for during a temperature variation with the aim to calibrate the system and ensure the sensing reliability for different FBG bandwidth: 230pm, 315pm and 500pm. The setup used is referred to the Figure 3.26: The FBG sensors were positioned with thermal paste onto a heat plate which is capable to yield the temperature variation, while the voltage signal was ac-quired by a DAQ board and processed by means of a GUI designed ad-hoc for the test. Each of three Bragg wavelength shifts among 3 AWG channels, in a range of about 1.6nm. In order to verify the correct functionality of the system, the Bragg wavelength characterized by 500pm of FWHM was interrogated in the first place
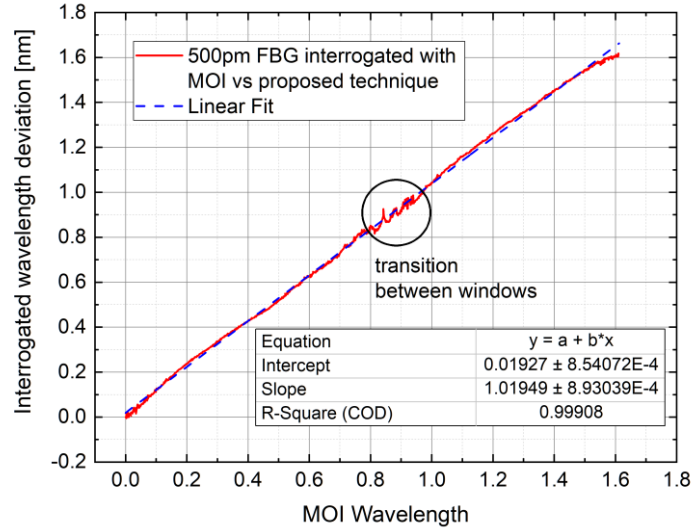
Figure 3.27. Comparison between the 500pm FWHM FBG interrogated with MOI vs the proposed interrogation system (red) and the linear fit (blue, dash).

with a Micron Optics Interrogator (MOI) as reference, then, successively, with the proposed one with the same temperature shifting. The Figure 3.27 shows the result in which can be noticed the wavelength detected by the MOI vs the one obtained by the interrogation system performing the proposed algorithm. The agreement between the two approach is validated by the linear behavior present in the plot. Among many measurements, which were led to ensure the repeatibility and stability of the system, in the next subsections three cases (one for each FBG) are reported in which are depicted the wavelength detected over the 3-channel shifting. Since a one-to-one correlation between the output voltage level and the AWG spectrum is present, this information was used as reference value monitoring the interrogated wavelength value on the maximum of each AWG channel.

- For the 230pm FBG, AWG channels 35, 34 and 33 were employed (the equivalent peak wavelength is 1549.315nm, 1550.116nm and 1550.918nm for each channel). In order to ensure a linear variation among the

interested channels, the initial transient given by the heat plate was avoided. This was done cooling the FBG in such a way that the Bragg wavelength was positioned before the channel 35 peak, allowing the transient to take place within the window 36-35.The Bragg wavelength position relative to the starting temperature was checked with the MOI system. The validation of the measurement, as well as the error, was calculated subtracting the interrogated FBG wavelength value in the mentioned wavelength points, which are known from the AWG channels spectra. In figure 3.28 it is shown the result: the interrogated Bragg wavelength matches optimally the AWG spectrum, exhibiting an error in the sub-picometer range at the AWG channels peak. It can be noted a narrow region (circled in magenta) with a change in the slope, which is given by the transition between the windows 35-34 and 34-33. This unwanted alteration is caused by the first order Gaussian approximation, as described in section 3.3.1.
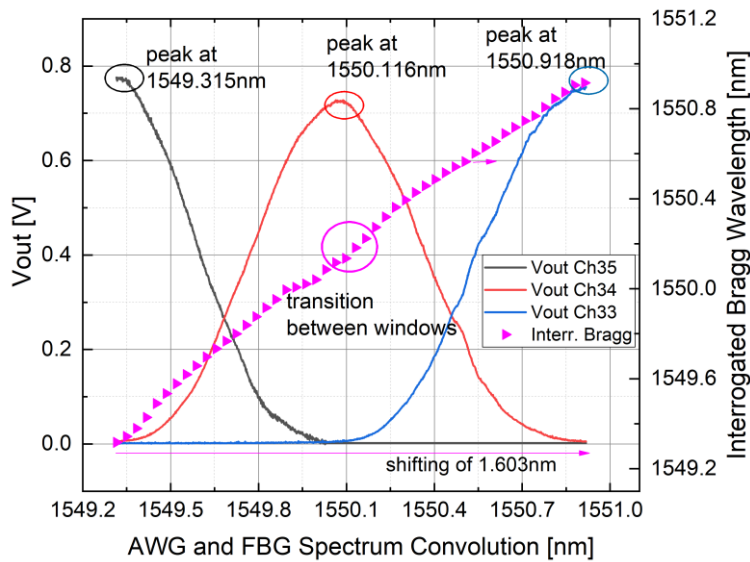
Figure 3.28: Interrogation of a 230pm bandwidth FBG among AWG channel 35, 34 and 33.

- For the 315pm FBG, AWG channels 28, 27 and 26 were employed (the peak wavelength is 1554.940nm, 1555.747nm and 1556.555nm). The FBG wavelength was positioned before the channel 28 peak, to ensure a linear variation among the interested spectrum (ch28-26). Again, the Bragg wavelength position relative to the starting temperature was checked with the MOI system. As in the previous case, the validation of the measurement was checked subtracting the interrogated FBG wavelength value in the mentioned wave-length points, which are known from the AWG channels spectra. The resulting plot is shown in figure 3.29: also in this case, the error is in the sub-picometer range at the AWG channels peak and a narrow region (circled in magenta) with a change in the slope is present, which is given by the transition between the windows 28-27 and 27-26.
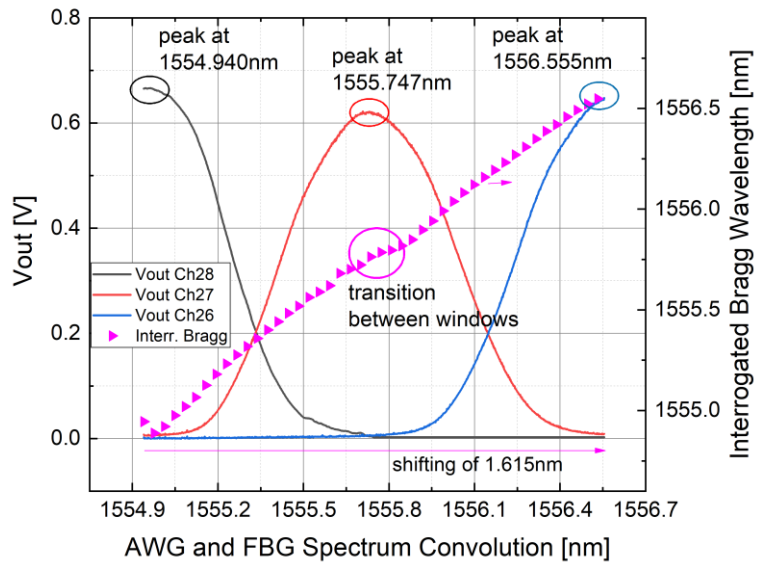
Figure 3.29: Interrogation of a 315pm bandwi*d*th FBG among AWG channel 28, 27 and 26.
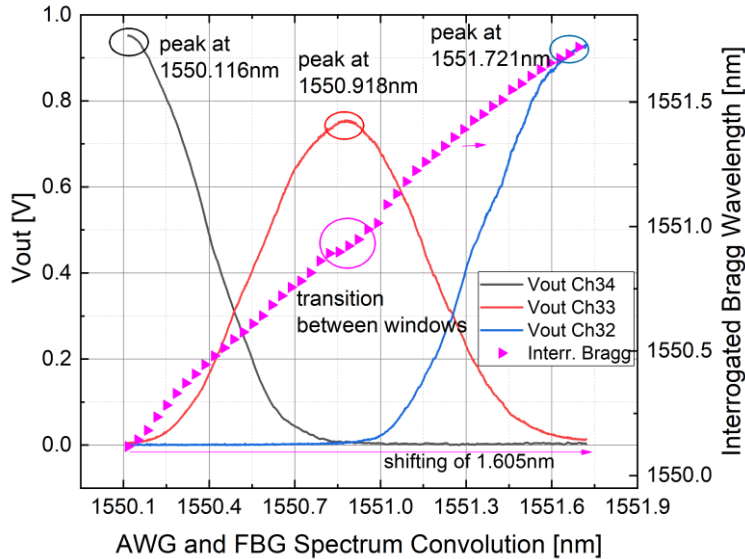
Figure 3.30: Interrogation of a 500pm bandwi*d*th FBG among AWG channel 34, 33 and 32.

- For the 500pm FBG, AWG channel 34, 33 and 32 were employed (the peak wavelength is 1550.116nm, 1550.918nm and 1551.721nm). The FBG wavelength was positioned and measured as the previous case, as well as the validation of the measurement. The result is shown in Figure 3.30: here, the slope variation (circled in magenta) given by the transition between the windows 34-33 and 33-32 is less pronounced due to the wider FWHM of the FBG under test, exhibiting a convolution with the AWG channels spectra closer to a first order Gaussian. As before, the measurement error changes among the sub-picometer value over the Gaussian peaks.

3.3.3.2   Strain Measurement

To test the calibrated algorithm in a non-quasi static wavelength variation, a strain measurement in the hundreds of Hz range was done. The AWG channels employed are the ch 35 and ch 33. The FBG was

(a)

(b)
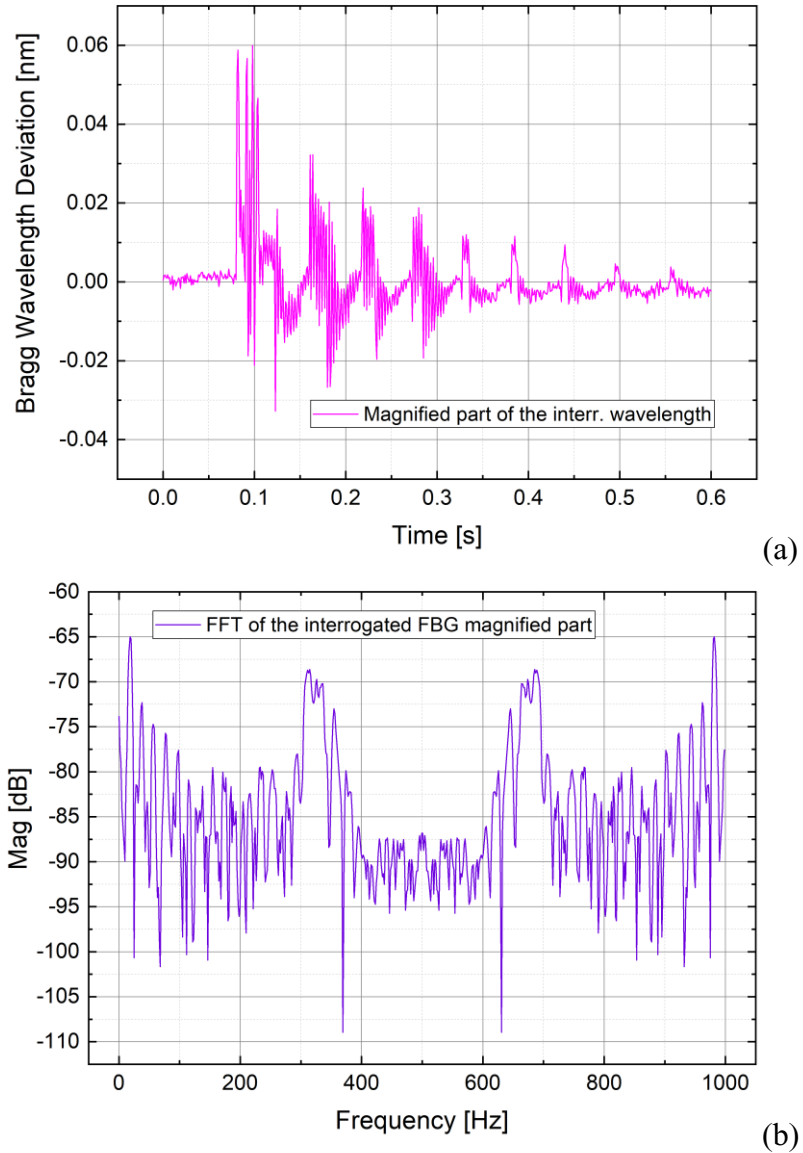
Figure 3.31: Bragg wavelength interrogated during a strain measurement (a), with the relative FFT (b).

pre-strained in the window 35-34 with the possibility to sense both elongation and compression. The test was conducted by hitting a metal plate of 4mm thickness where the 230pm FWHM FBG sensor was glued on. The result is shown in Figure 3.31 in which is represented the

Bragg wavelength variation in time domain (Fig. 3.31a) during the vibration phenomenon, and the corresponding frequency analysis by means of a Fast Fourier Transform (FFT) in Figure 3.31b.

3.3.3.3   High-Speed Measurement

To investigate the capability to sense a physical phenomenon whose variation is in the order of Mhz, a high-speed measurement was conducted as well. The vibration was generated by an ultrasound probe (Figure 3.32) whose oscillation is in the order of few MHz and is sensed through the same FBG glued on a metal sheet employed for the previous case. To check the correct working of the ultrasound probe, an oscilloscope was connected to it, processing the reflected as illustrated in Figure 3.33a. In this latter, a spike is showed representing the probe ignition with a pulse at -70V (that is a typical value for this kind of probe) generated by an external circuitry, followed by a series of low intensity vibration. In Figure 3.33b the FBG measurement is depicted: the output voltage of the AWG channel 35 and 34 are represented with the relative interrogated Bragg wavelength obtained with the detection algorithm. It's worth to note the evolution over time is the same for both electrical and optical behavior, confirming that the vibration sensed by the FBG are generated via the ultrasound probe.

Figure 3.32: High-speed measurement with an ultrasound probe resting on a metal sheet with an FBG glued
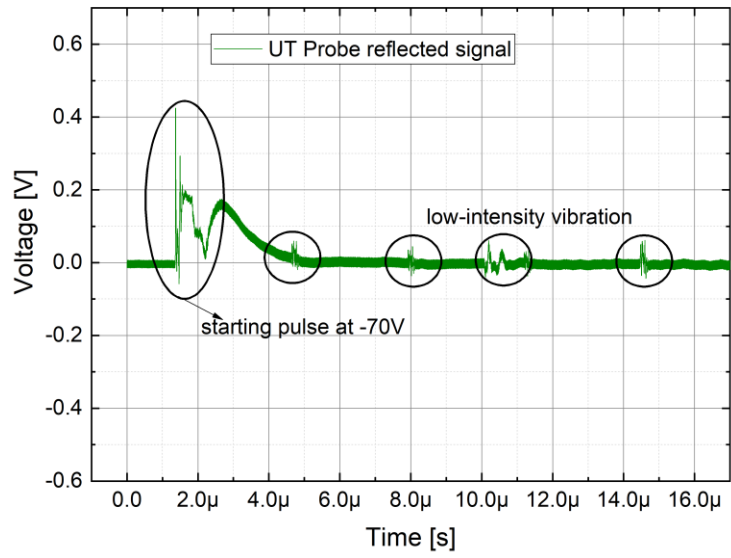
(a)
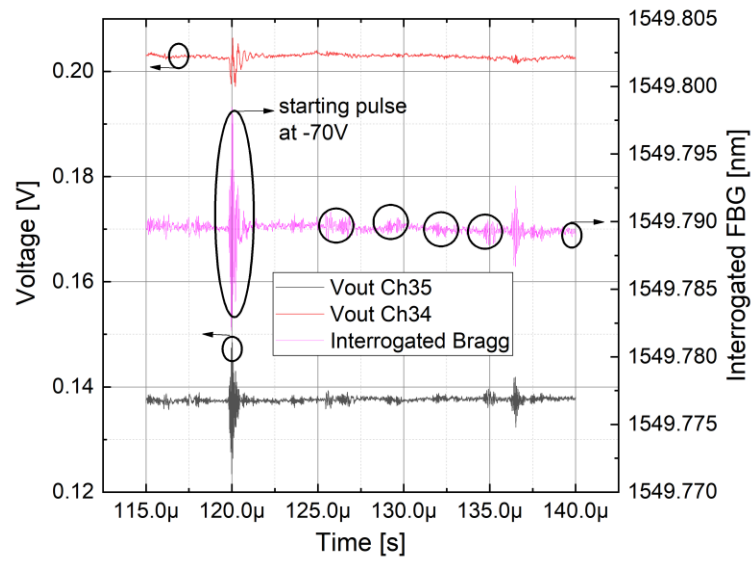
(b)
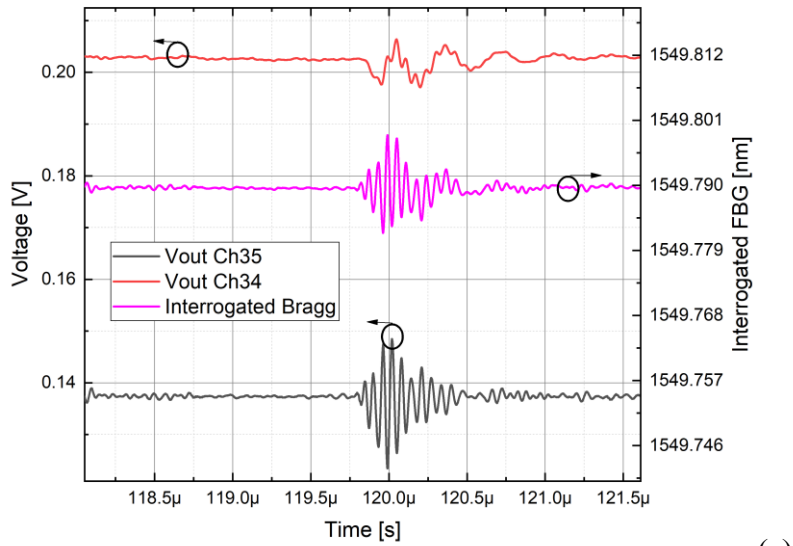
(c)
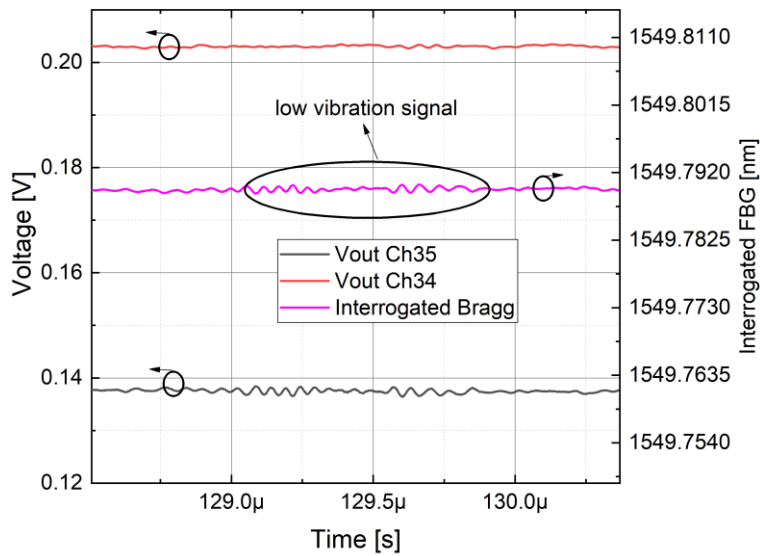
(d)

Figure 3.33. Ultrasound probe reflected signal measurement, with the highlighted part obtained resting the probe on the metal sheet (a). Output voltage from the monitoring of channel 35 and 34, with the interrogated FBG in the middle (b). Magnified part of the high-speed signal, during the ignition pulse, measured by the FBG sensor (c). Magnified part of the reflected signal, during the probe resting on the metal sheet, measured by the FBG sensor (d).

The vibrations from the metal plate are detected as well. In Figure 3.33c a magnified part of the probe ignition is represented, while in Figure 3.33d a magnified part of the vibrations generated by the contact between the probe and the metal are reported.

3.4   Conclusions

In this chapter the capability to interrogate one or many fiber optic sensors with a system having a modular dynamic range has been investigated through a multichannel approach based on Arrayed Waveguide Grating device. Starting from theoretical study, an analytical model of the system has been obtained. It has been demonstrated that the classical 2 channels sensing approach can be overcome by the multichannel methodology without affecting the sensitivity of the system but increasing dynamic range. In this work massive experimental analyses have been conducted with a 40-channels AWG with 800pm of frequency spacing and 600pm of channel bandwidth with different kinds of FBG sensors. Discrepancy between the theoretical model and real characteristic of optical devices has been taken into account and have been mitigated opportunely.

Temperature tests have been reported by using three different FBG sensors characterized by 230, 315 and 500pm of FWHM. All results have proved the feasibility and the reliability of the system. Measurements were made in large wavelength variations covering at least 3 AWG channels.

Strain measurement has been reported to test the system in dynamic measurement conditions. A 4 mm metal plate, on which the 230pm FWHM bare FBG was glued, was hit by a hammer, causing mechanical stresses in the range of hundreds of Hz. Moreover, with the same plate-FBG, a high-frequency measurement has been conducted sensing the vibration generated by an ultrasound piezoelectric source. In both situations, the proposed interrogation system has been successfully used to sense the FBG vibration in the 100Hz and MHz range, detecting the starting vibration pulse and the low intensity signal of the piezoelectric source.

The aforementioned experimental analyses have been acquired with a custom high-speed and low-noise electrical module composed by a reverse biased photodetector and a double stage transimpedance

amplifier and processed by mean of a DAQ board and a GUI. The electrical section offers a 3dB bandwidth of more than 5Mhz and, since the optical section is completely passive without movable parts, this is the only constrain which limits the speed of the interrogation system. Obviously, it is also possible to play with the bandwidth-noise trade-off to increase the equivalent speed inter-rogation performance. Hence, with the proposed interrogation system, it is possible to overcome the limits that afflict the state of the art of the AWG-based systems.

In conclusion, the proposed optoelectronic circuit and elaboration stage, which exhibits a large modular dynamic range that works up to 5Mhz with multiplexing capability, constitutes a strong competitor in the field of Interrogator System for FBG arrays for both static and dynamic measurements thanks to its stability, robustness and reliability.

Chapter4: Full Analog AWG-Based Safety System

Even if FOS are broadly employed in many applications due to its advantages, they are up to now not so widely used for the monitoring of industrial processes [132] and are usually substituted with low performance but easier to manage sensors, in agreement with industrial monitoring standards. Furthermore, although FOSs are the perfect candidate for the monitoring of temperature and strain [133]–[135], they are not used as sensors in a safety monitoring system. Among many causes for this slowdown, it is worth to highlight the limits of state-of-art interrogation systems which are based on digital processing data making them not so reliable enough to be employed in that kind of application in which a direct conversion from the physical phenomena and an electrical signal is needed (e.g. temperature monitoring with PT sensors). The aforementioned papers, so do a few others in literature, regard optoelectronic circuit in which a digital section is needed. As depicted in Figure 4.1, the typical interrogation system for the monitoring of a physical quantity, uses a FOS with a certain spectrum that has to match with a filter (AWG, linear or Fabry-Perot) or has to be detected from a tunable laser. The reflected wavelength by the sensor has to be converted in an electrical signal and then sampled and processed with a digital unit. After this series of manipulations, the output data in form of wavelength shifting is ready to be read and converted in the related physical quantity. This kind of techniques made up with a high number of processes for data manipulation, although perform a high accuracy detection, are not suitable for that environments in which it is required a data acquisition in a more robust way. Looking again at Figure 4.1, the concept is free from digital processing, due to its peculiarity to have a modular electrical section which can be designed ad-hoc in respect of the sensor under test. The output data is an analog monotone signal in the range 4-20mA, compatible with the

TYPICAL FOS MONITORING SYSTEM

| Physical Quantity to Sense | → | Fiber Optic Sensor | → | Optical Detection | → | Electrical Detection |
| Sampling | → | Digital Processing | → | Output Data |

PROPOSED FOS MONITORING SYSTEM

| Physical Quantity to Sense | → | Fiber Optic Sensor | → | Optoelectronic Detection | → | 4-20mA conversion |
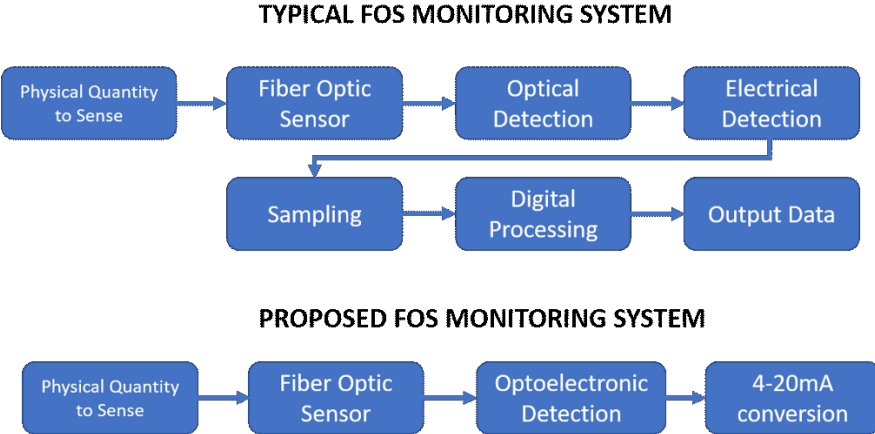
Figure 4.1: Typical interrogation system block chain compared to the proposed system.

input of a Programmable Logic Controller (PLC). The proposed optoelectronic system allows to the well-known FOS technology to be directly and simply embedded into PLC systems and/or a security related scenario, without the need of A/D and D/A conversions. It has the potential to turn FOS measurement systems in an alarm system, where every measurement point is able to be "logically connected" to an alarm switch which, for example, switches when a threshold is overcame. The proposed approach can be applied in harsh environments, always relying on the intrinsic advantages of FOS technology, but especially in that scenario, e.g. industrial processes, where the PLC ruggedness is required.

4.1   Operation Principle

The working principle of the proposed system depicted in Figure 4.2 is as follows: a broadband luminescent source generates a light signal propagating, through an optical circulator, towards a FOS (for simplicity one Fiber Bragg Grating sensor is considered) whose working principle is to reflect a part of it in respect of the spectrally reflectance shape from which it is characterized. The reflected optical signal propagates towards the AWG, with a proper spectral transmittance, filtering the input and letting it propagates towards one
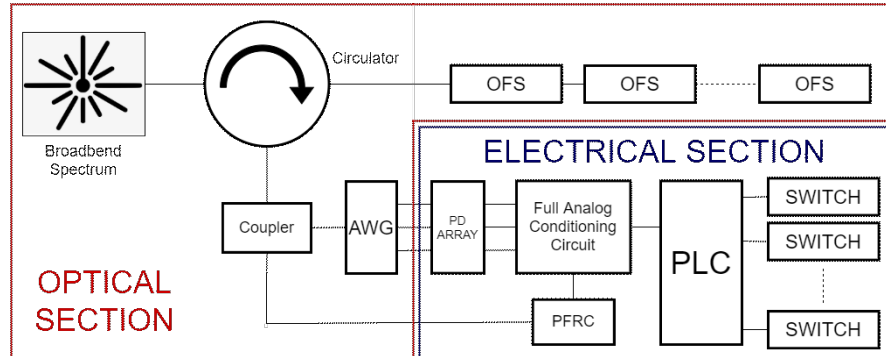
Figure 4.2: Optical and electrical section composing the proposed system.
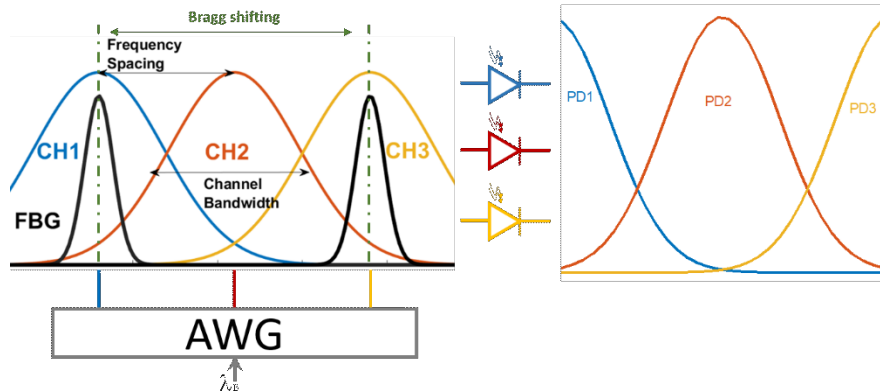
Figure 4.3: Illustration of the photogenerated current due to an FBG shifting among three AWG channels monitored with three photodetectors.

of the multiples output channels dedicated to the FBG sensor under exam. The emerging optical signal coming from the single channel is then handled by a number of Sensing Circuit, composed of a photodetector and an entirely analog conditioning circuit. This latter is shown in Figure 4.3 and it is composed by a first stage with a transimpedance amplifier (TIA) with the aim to transduce the photogenerated current from the photodetector in a voltage signal; a variable gain amplifier (VGA) which is needed to restore, in case a malfunction occurs, the output level; an optical barrier to completely separate the mentioned devices (sensing part) with the output stage and avoid possible leakage current which can damage the devices; a last gain variable stage which has the aim to match the output system with the PLC input.
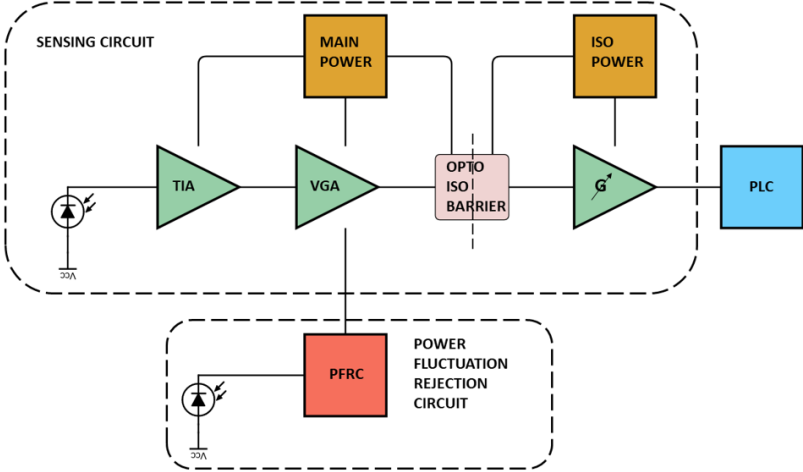
Figure 4.4: Block scheme about the sensing circuit composing the full analog electronic section.

This latter stage, in case more sensing board are employed for the same sensor, is used as an adder stage which combine the spectrum coming from AWG channels. The variation of the physical quantity which has to be monitored by the sensor, produces a wavelength variation of the optical power which illuminates the AWG. Consequently, the photodetectors connected to the AWG channels, is sequentially illuminated allowing an increment of the output current or voltage (Figure 4.4). Setting a threshold value, in terms of voltage or current, it is possible to trigger, then, a switch that activates an alarm if the monitored physical quantity exceeds the safety limits.

The main feature of the proposed system is the fully analog conditioning circuit which generates an output signal included in a range between a minimum and a maximum value: the minimum is always different from the null value, in order to have a check on the working status; the maximum depends on the switch threshold value. Moreover, the system is completely modular depending on the type of FOS, the number of sensors to read simultaneously, the kind of the physical quantity and the current or voltage threshold.

4.1.1 Electrical Considerations

To better understand the characteristics of the Sensing Circuit an electrical analysis was conducted. The photodiode employed is the same for the circuit designed in chapter 3: an InGaAs technology with responsivity close to 1. The TIA needed for this application is completely different from the LTC6244HV since here the robustness and reliability are the most important features to obtain, instead of the high-speed and high gain needed in the previous chapter. The operational amplifier is the ADA4625 by Analog Devices, characterized by a GBP of 18MHz, a low noise density of 3.3nv/√Hz, an input current of 15pA and, above all, an output short-circuit current of 46mA and a supply operation of 36V (+/- 18V). The signal flows then into a VGA by Texas Instrument (VCA810) which has a GBP of 35MHz, high output current, low input density noise and a limited voltage input. For this latter reason, the TIA gain is dimensioned with a low resistor (1 kΩ) while the further gain (designed ad-hoc to get an output signal in the range 4-20mA) is given by the followed stages. Due to the low feedback resistor, the TIA bandwidth is too wide (few of MHz as illustrated in Figure 4.5) hence, the system bandwidth is limited by the optoisolator. It's worth to note the stability parameters depicted in Figure 4.6: the phase margin is about 100° indicating a good stability; the gain margin, calculated as the gain value when phase is 180°, exhibits a negative value and a positive one, both at very high frequency (262 and 447MHz as illustrated in Figure 4.6) in respect of the working frequency of the system (tens of kHz). The positive gain margin may trigger instability, but it was noted by experimental analysis that this harmonic does not affect the circuitry.

As written, the bandwidth is limited by the optoisolator which is the IL300 by Vishay. It works with a LED irradiating the input signal towards two photodetectors, one in feedback with an amplifier while the other in output to a second amplifier. With this configuration the input signal is totally replicated in output without lose in speed and voltage level. The schematic from the application note [136] illustrated in Figure 4.7 shows the configuration in photoconductive mode: with this modality the maximum speed is guaranteed (200kHz) but also a high noise. In Figure 4.8 it is shown an experimental measurement of a
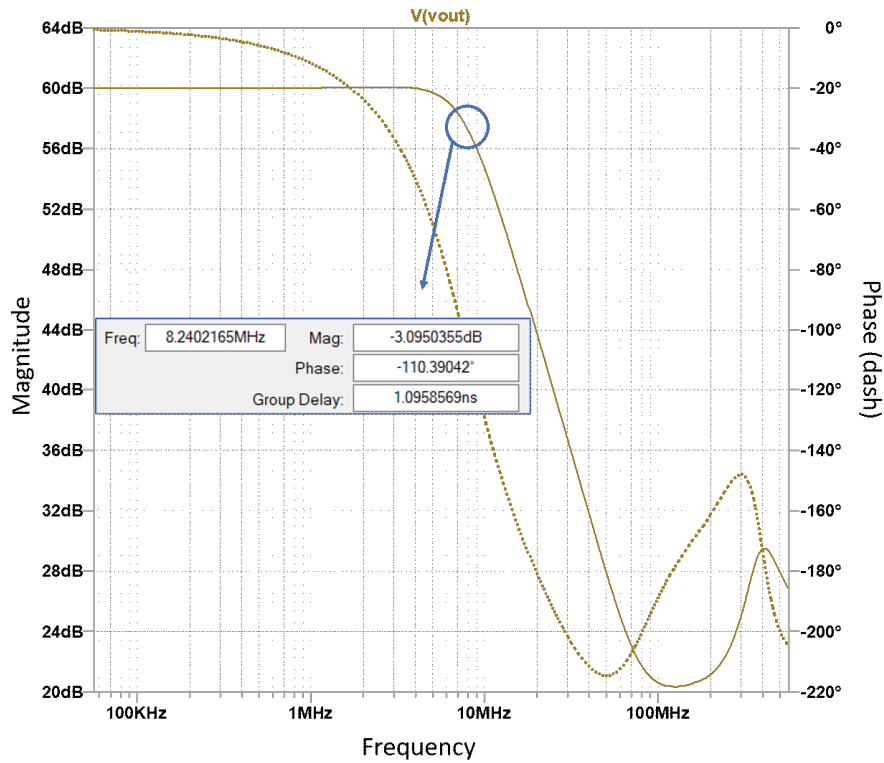
Figure 4.5: ADA4625 Bode diagram. With 1k of feedback resistance and 20p of feedback capacitance the 3-dB bandwidth is over 8MHz.

temperature variation monitored with an FBG sensor during the heat-up and cool-down. Looking at the configuration in Figure 4.9, the circuitry is in photovoltaic mode: the speed is reduced (40kHz), but the noise produced by the increment of the photodetectors' dark noise is significantly reduced as depicted in Figure 4.10 in which is represented the same measurement of 4.8. In next paragraph, experimental measurements are led with the IL300 in photovoltaic mode.
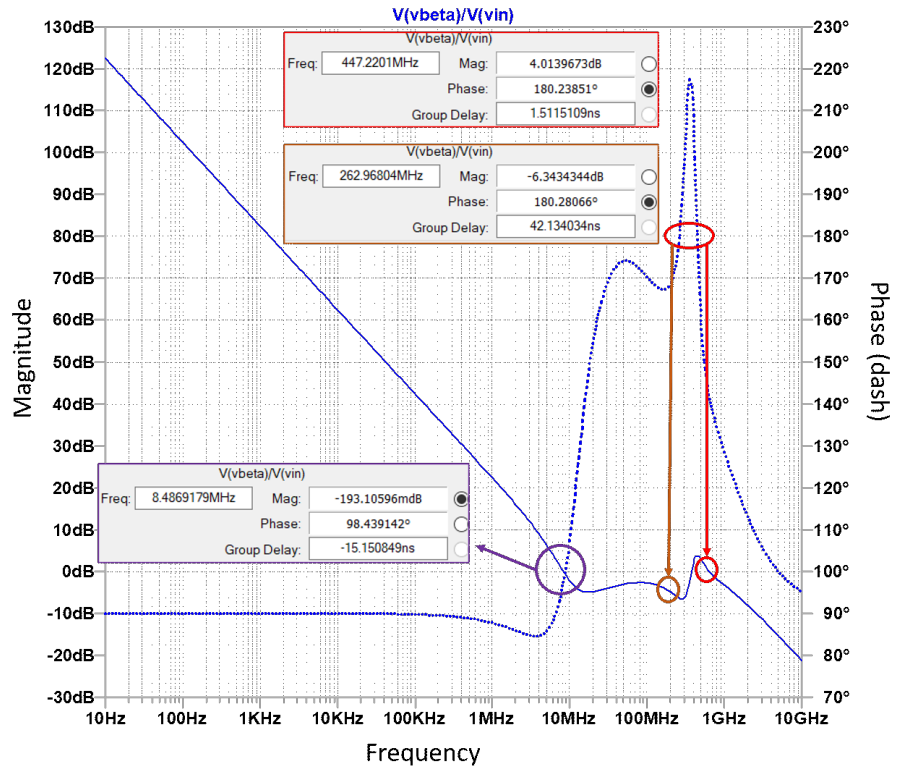
Figure 4.6: ADA4625 stability diagram. With 1k of feedback resistance and 20p of feedback capacitance the phase margin is 100° while the gain margin exhibit a negative value and a positive value out of working bandwidth.
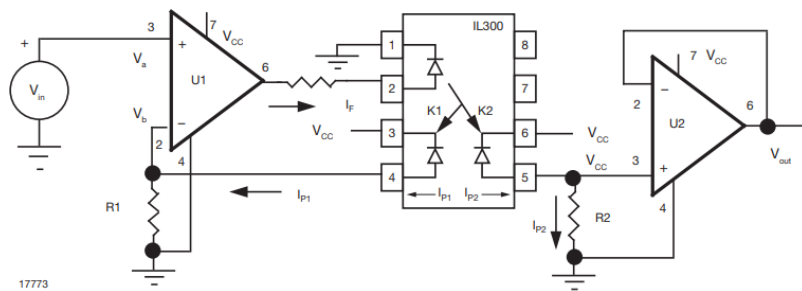
Figure 4.7: IL300 in photoconductive mode [136]. The photodetectors are reverse biased producing a speed and noise increment.
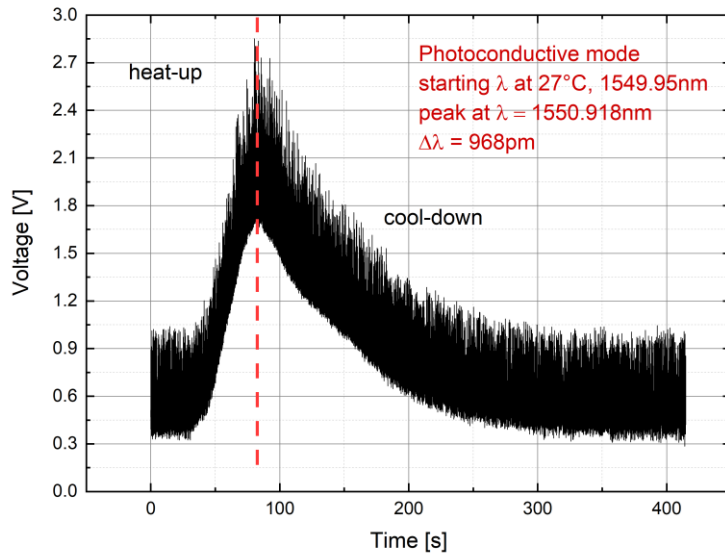
Figure 4.8: Experimental analysis with the IL300 in photoconductive mode. The result was obtained from a temperature variation during the heat-up and cool-down step of an FBG sensor.
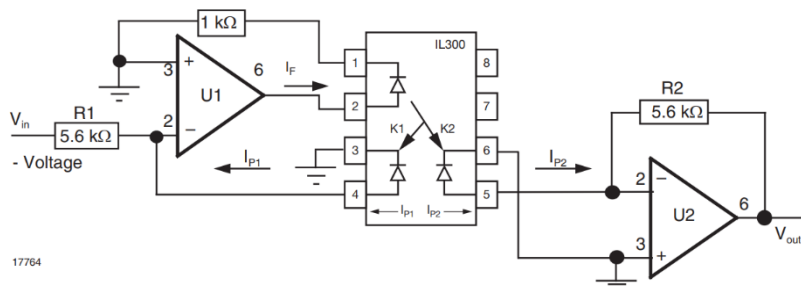
Figure 4.9: IL300 photovoltaic mode configuration [136]. The photodetectors are not biased, decreasing the dark current, hence the noise.
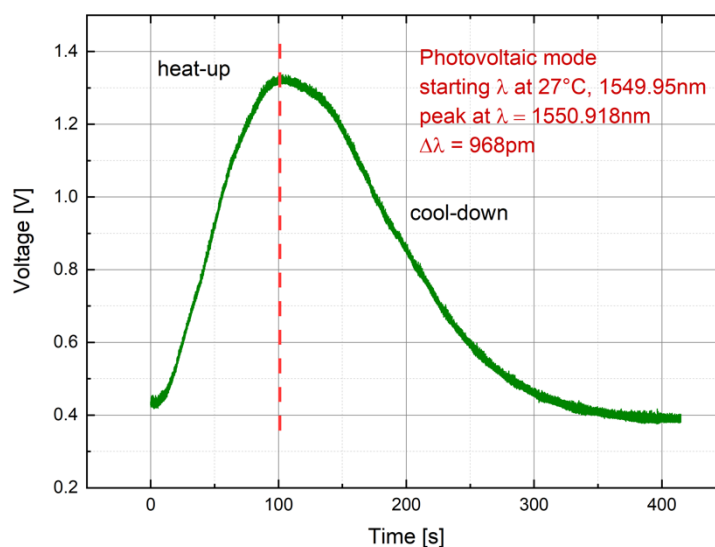
Figure 4.10: Experimental analysis with the IL300 in photovoltaic mode. The result was obtained from a temperature variation during the heat-up and cool-down step of an FBG sensor.

4.1.2 The Power Fluctuation Rejection Circuit (PFRC)

The optoelectronic circuit also contains a power fluctuation rejection circuit (PFRC), whose schematic block is depicted in Figure 4.11, which takes as input a part of the optical signal reflected from the FOS chain, before the demultiplexer filtering, comparing it with a reference current and generating, in case of power fluctuations, a control signal with the aim to compensate this power variations. It is a full analog subsystem designed to compensate the power fluctuations which can occur on the Broad Band Spectrum Source (BSS) or the eventual losses on the optical connectors or within the circulator. All these events can lead to long-term change in the circuit's output characteristic and this is not acceptable since the whole is designed to be a monitoring system. This technique works out the aforementioned issues that, involving the decimation of the optical power, lead to a decrease/increase of the output electrical signal. A little percentage of the back reflected light from the FOS chain and before the AWG is sent, through the mean of a photodetector, to a Logarithmic amplifier which perform a comparison with a reference current that is the expected one
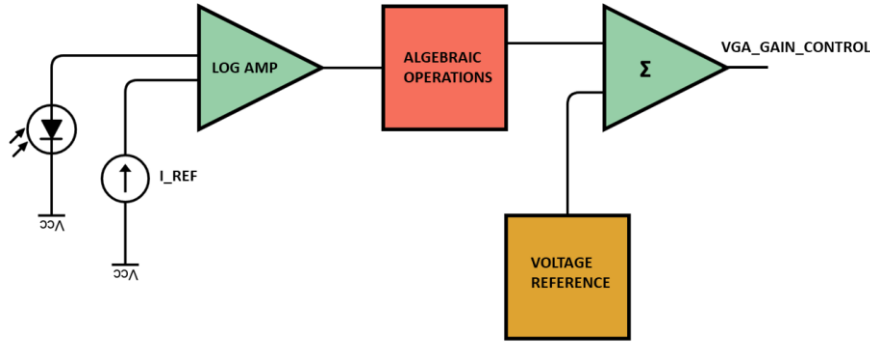
Figure 4.11: Illustration of the block scheme about the power fluctuation rejection circuit.

when the system is deployed on the field. The result of the comparison is a linear output characteristic that increase if the back reflected light decreases. A such obtained signal is used in combination with some others algebraic operations to generate a control for a Variable Gain Amplifier (VGA). The latter one is placed on the sensing circuit at the output of the TIA to restore the original voltage signal in case of power losses.

The Logarithmic amplifier output is in the form

$$V = 0.5 \log\left(\frac{I_1}{I_{REF}}\right) \tag{4.1}$$

the VGA's one, instead, is described by

$$G_{VGA} = 10^{-2(V_{control_{VGA}}+1)} \tag{4.2}$$

where G_{VGA} represents the gain expressed in V/V. The algebraic operations are needed to produce the right voltage level to let the VGA behave as intended, e.g. if the source's current is halved then the control signal is such that the VGA applies a x2 gain to restore the expected
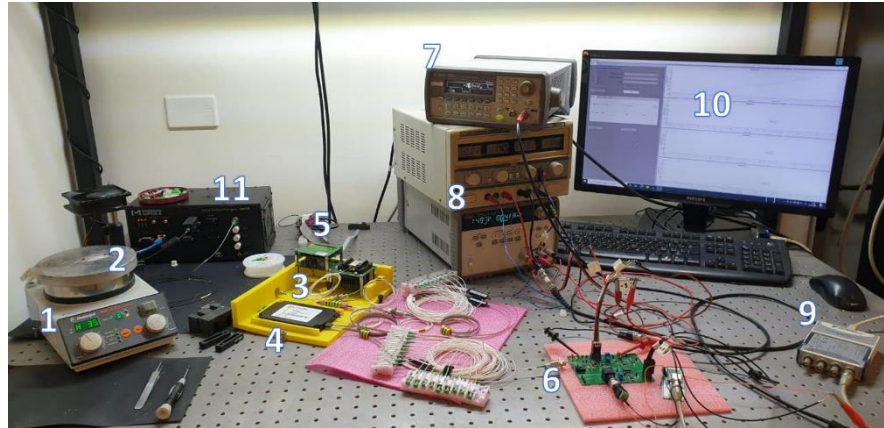
Figure 4.12: Description of the measurement bank in which the numbers represent the devices and facilities employed during the experimental analysis. The description follows in the text.

signal's levels. The voltage reference is used to keep the latter in a "unity gain" state so, that if no power fluctuations occur, there is no modification of the TIA output signal.

4.2   Experimental Measurements

In this paragraph some measurements were led to prove the feasibility and the reliability of the system. Since the system has the aim to be employed as safety monitoring, a temperature variation was sensed with a ΔT of 50°C which is a possible real case scenario that the proposed system may face when used as fire alarm in industrial environment, and a ΔT of 130°C to prove the peculiarity to have a modular dynamic range. The measurement bank is depicted in Figure 4.12 and the description follows: the AWG (3) employed is a 40 channel with 0.8nm of frequency spacing and 0.6nm of Full Width at Half Maximum (FWHM) while a FBG (2) with 0.315nm of FWHM is the sensor under test with a Bragg Wavelength of 1555nm. The light source (5) is a SLED with a 20mW output power which contains in a flat spectrum the whole AWG which goes from 1528 to 1560nm. The optical circulator (3) is also contained in the AWG spectrum range. The electronic section was soldered on a matrix board (6) with discrete
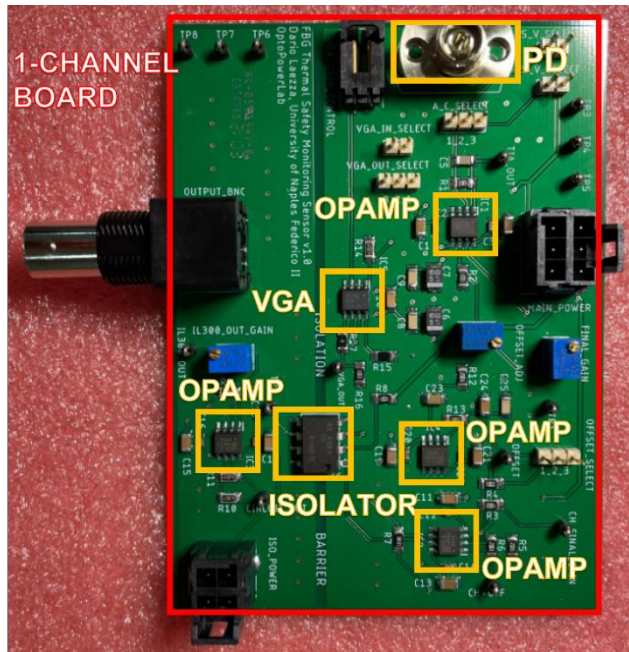
Figure 4.13: The sensing circuit employed, composing the full analog conditioning circuit, soldered on a PCB.

components as depicted in Figure 4.13 (it is composed by two sensing circuit). Data were obtained through a DAQ board (9) by National Instrument connected to a Graphical User Interface (GUI) (10) with which is possible to change the sampling frequency, see in real time and store data. A heat plate (1) is also needed and a FBG calibrated (2), interrogated with a Micron Optics system (11), was positioned close to the FBG under test with the aim to have a temperature reference. Other equipment are two DC supply (8) to power the PCB and a function generator (7) which is needed to gain the sensing circuit with an offset signal.

4.2.1 1-Channel Measurement

As shown in Figure 4.14, the FBG under test is positioned between the channel 28 (with central wavelength of 1554.94) and channel 27 (with central wavelength of 1555.747). Since the optical output is given by the integration of the superposition between the FBG

reflectance and the AWG dedicated channel transmittance, since the measurement consist of a temperature increment, the FBG will shift between the channel 28 and channel 27 spectrum with the possibility to use either one channel or the other to follow the output spectrum.

-   If the photodetector is positioned on the channel 27 the output power is given in Figure 4.15 as the blue shape: at the starting point, for few hundreds of picometers, the superposition between the FBG and channel 27 gives low power values which is translated in tens of degrees hard to detect if the noise is high. A furthermore problem can occur if the temperature raises experiencing a wavelength shifting over the channel 27 peak: the output power will start decreasing due to the gaussian shape.

-   If the photodetector is connected to channel 28 (Figure 4.16, black shape) the superposition between the FBG and channel 28 gives an output spectrum with a high accuracy, furthermore, even if the temperature raises over the maximum value, the output power keep going with a constant value. To have an increasing monotone shape, the curve must be inverted.

The right choice to have an increment of the accuracy and a constant value over a threshold lead to use the channel 28 in reverse mode (Figure 4.16) as monitoring channel. The results follow with many plots in which the system output voltage (related to the temperature measurement) is considered with a reference temperature acquired with a calibrated FBG sensor, interrogated with a MOI. In Figure 4.17 it is shown the experimental result of a temperature deviation about 50°C which is approximately a shifting of 500pm of the FBG under test. Since the digital acquisition board takes as input a voltage, the output is expressed in voltage as well. However, it is important to note that the system, once the load is given, is able to generate in output the right current in the range 4-20mA.

As expected, the voltage spectrum is increasingly monotone, in function of a temperature raise that is almost linear. With this measurement was proved the feasibility of the system and, furthermore, the possibility to employ only one AWG channel for the monitoring of a 500pm Bragg shifting. It was possible to match the output voltage in function of the temperature deviation with a polynomial fitting as
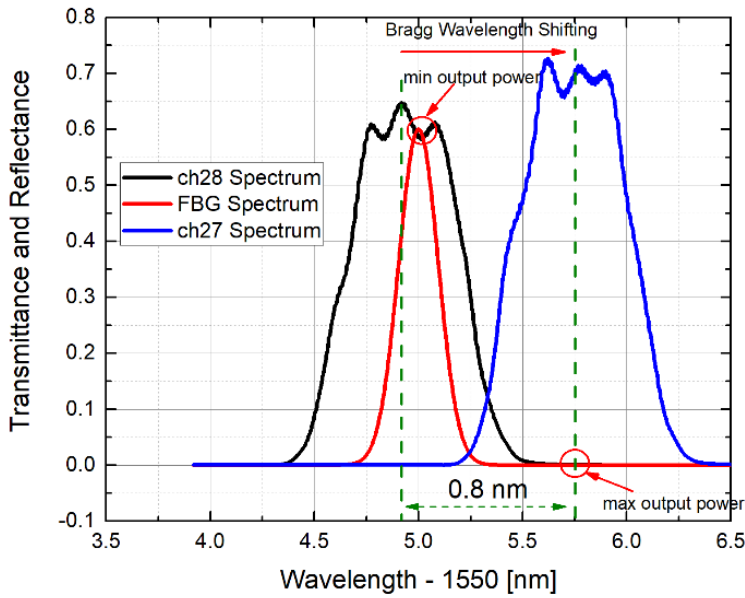
Figure 4.14: Superposition between the FBG under test and AWG channel 27,28.
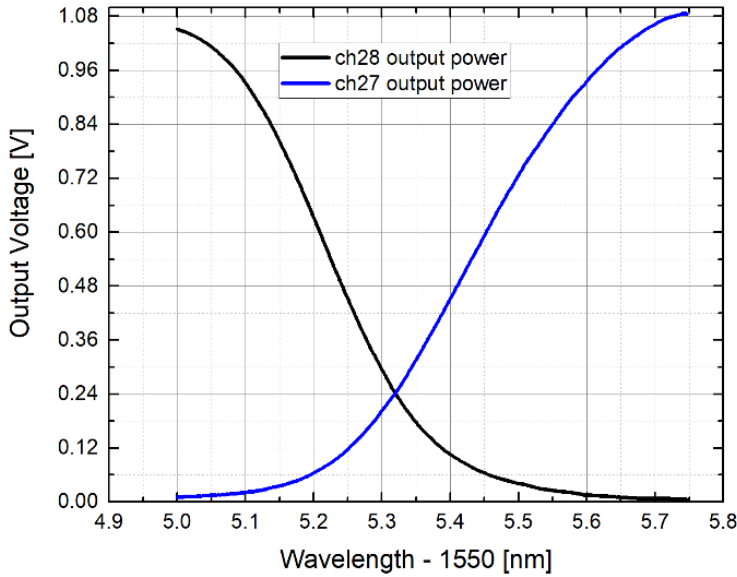
Figure 4.15: Output power spectrum for AWG channel 27,28.

shown in Figure 4.18: the goodness of the fitting, expressed with the R-square, is more than 0.99.
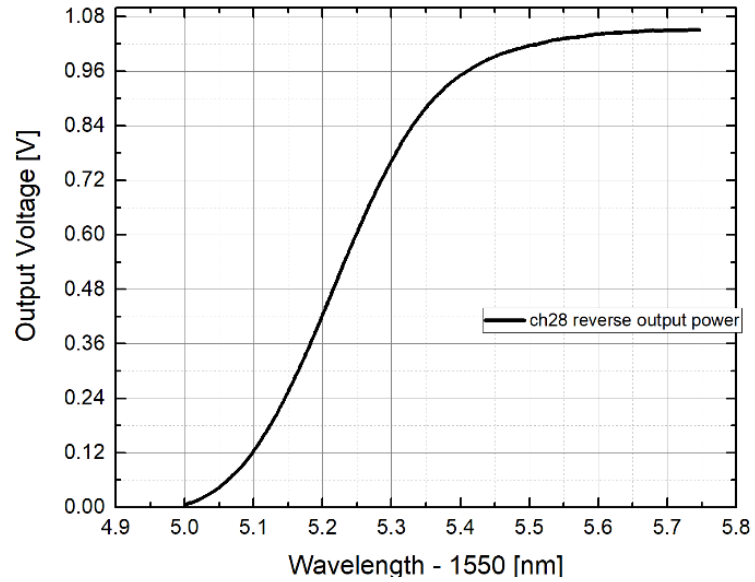
Figure 4.16: Channel 28 in reverse mode.
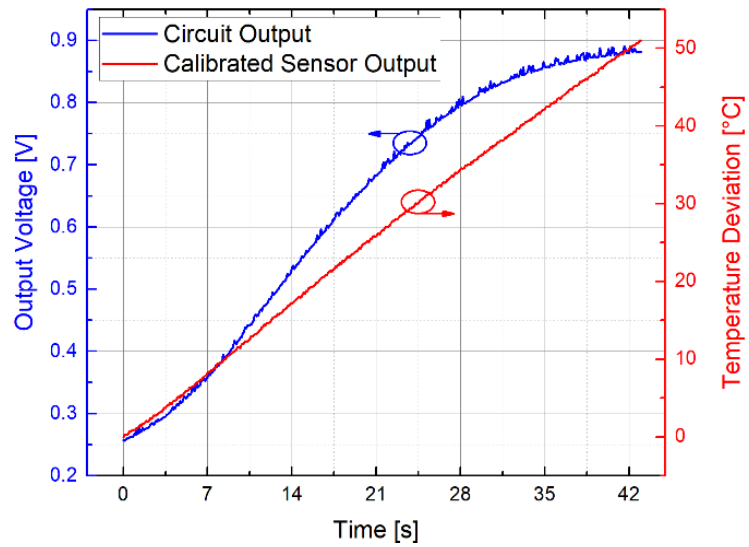
Figure 4.17: Time vs Current about the 1-channel experimental measurement with temperature reference.
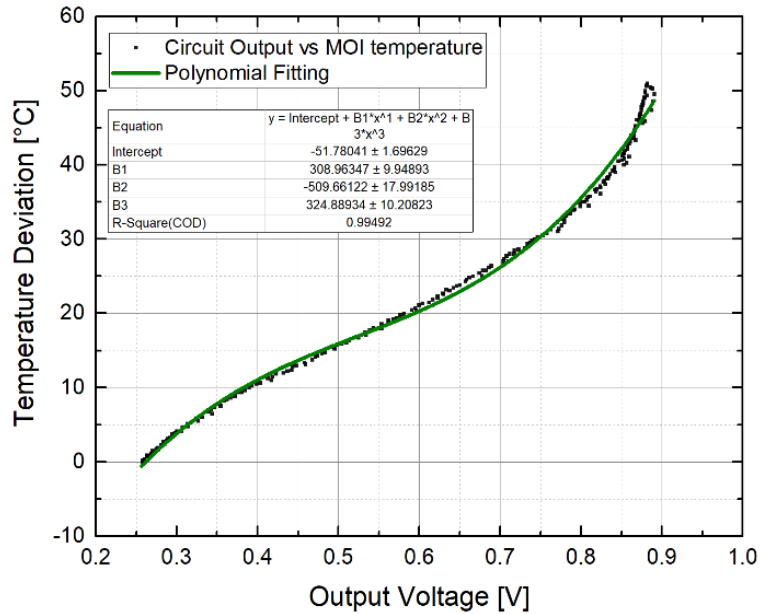
Figure 4.18: Voltage vs Temperature reference with polynomial fitting model.
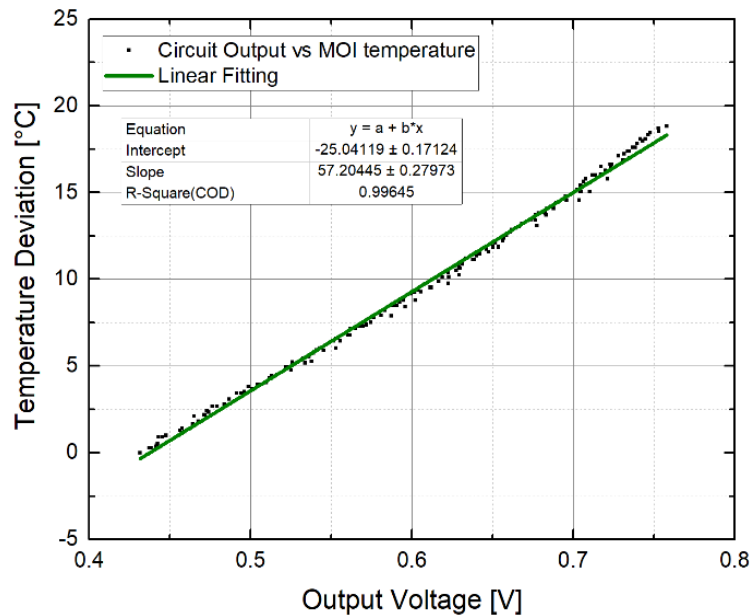
Figure 4.19: Voltage vs Temperature reference with linear fitting model.

This information may be used to calibrate the system response in function of the temperature to measure. As said above (also shown in Figure 4.18) the output voltage of the channel 28 presents a quasi-linear region on 400pm. Effectively, in a range of 20°C a linear fitting matches optimally as in Figure 4.19.

4.2.2 2-Channel Measurement

For this measurement, two AWG channels (27 and 26) were employed as shown in Figure 4.20. In Figure 4.21 the electrical scheme is depicted: in this effort two 1-channel board are given as input to an adder stage to combine the respective shape, obtaining a one output increasing monotone. Also, in this case the experimental result gives an increasing monotone spectrum: this result means that is possible to choose the number of AWG channels to employ in function of the physical quantity to sense: a monitoring system with a modular dynamic range. In Figure 4.22 the spectrum is displayed: channel 27 is fully monitored from the low sensitive area (initial part) to the peak. An almost flat region follows, then, a high accuracy region given by the increasing Gaussian shape of channel 26. Even if the transition between channel 27 and 26 is described by an almost flat region, a good sampling rate as the one characterizing PLC systems, is able to appreciate the variation. With a point-by-point calibration voltage(current)-wavelength the spectrum can be linearized without losing accuracy in low sensitive regions.
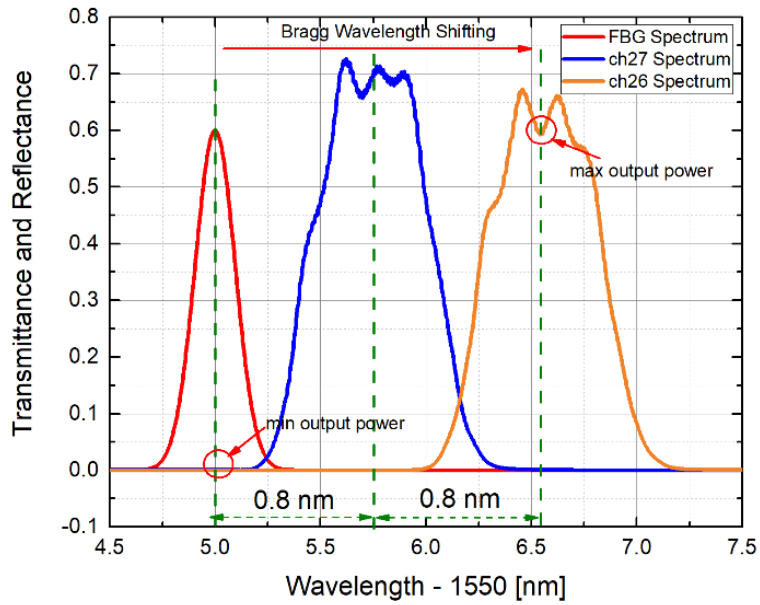
Figure 4.20: Superposition between the FBG under test and AWG channel 26,27.
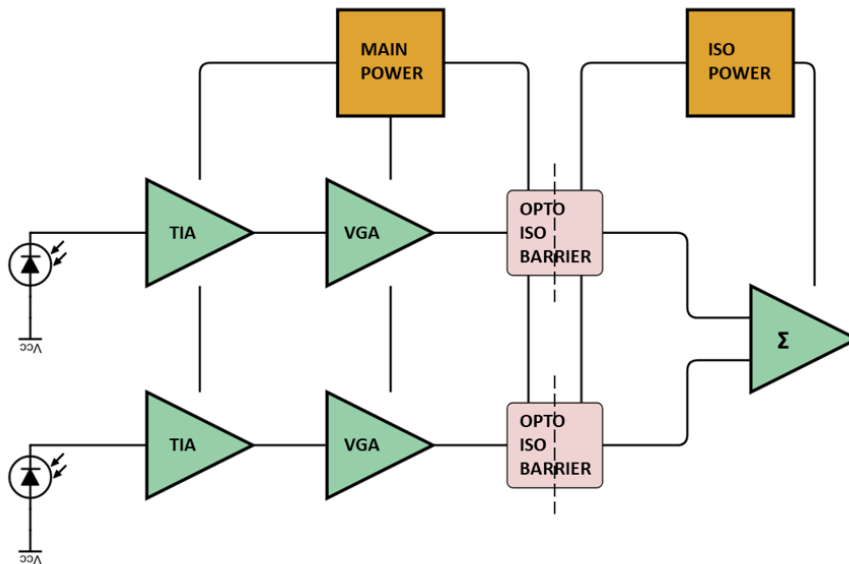
Figure 4.21: Block scheme about the electronic section in 2-channel measurement.
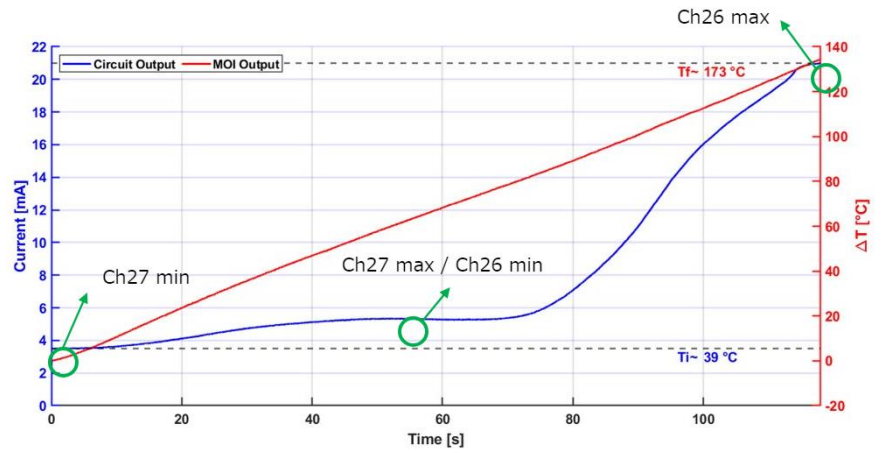
Figure 4.22: Block scheme about the electronic section in 2-channel measurement.

4.2.3 PFRC Validation

The experimental validation about the PFRC was conducted as well. The circuit was soldered on a matrix board with discrete components as depicted in Figure 4.23 and two cases are reported to

show the functionality: in the first one the source's current is set to its maximum (500 mA), in the second case the current is set to its half. Given an input reference voltage signal that consist in a sine wave at 10 Hz with a 30mV peak-to-peak amplitude with a 15mV offset, the VGA output is showed in Figure 4.24. In the first case the output follows the reference input signal, in the second one the output doubles.
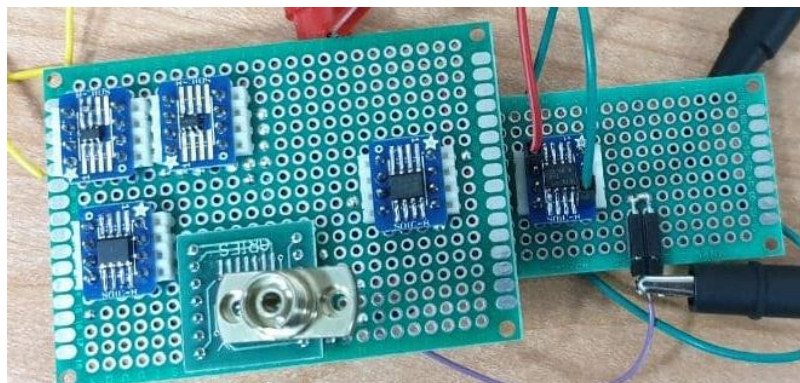
Figure 4.23: PFRC soldered on a matrix board.
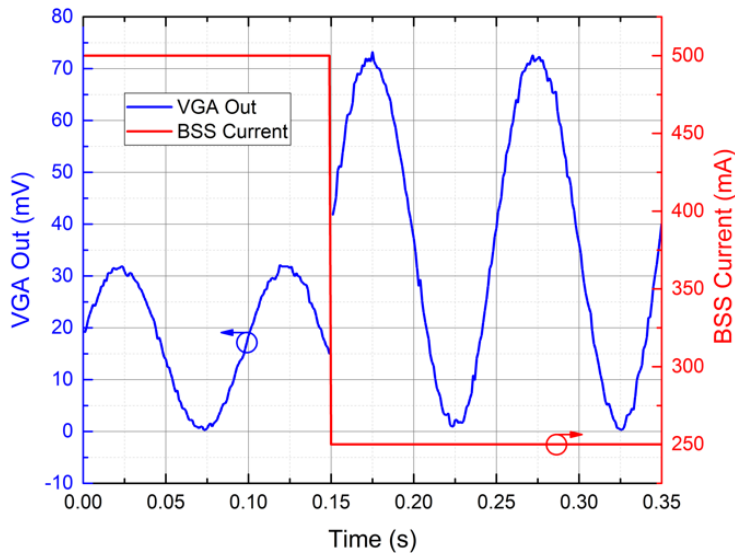
Figure 4.24: Samples vs VGA Output signal passing from 500mA to 250mA BBS current.

4.2.4 Reliability and Repeatibility of the System

With the aim to test the repeatibility, thus the accuracy, of the system, five measurements during the heat-up and cool-down stages were conducted. The quantity sensed is the same done in the previous subsection: a temperature variation produced by a heat plate with a calibrated FBG sensor close to the FBG under test. The temperature variation range is from a value of 25.5°C to 90°C. As shown in Figure 4.25, in which the reference temperature is reported in the second y-axes, a certain deviation is present among the curves. To understand the source of this error a comparison with the temperature variation experienced by the reference sensor was necessary: since the same deviation among the curves is present also for this latter for both the heat-up and cool-down stages, these shown spectrums oscillating around a mean curve are given by a systematic intrinsic error of the heat plate. The proposed concept presents an optimal degree of repeatability of the measurement.

Another measurement was done keeping on the whole system on a constant temperature value to get information on the reliability and

the stability of the proposed concept monitoring if a degradation of the accuracy occurs after many hours of acquisition.

(a)

(b)
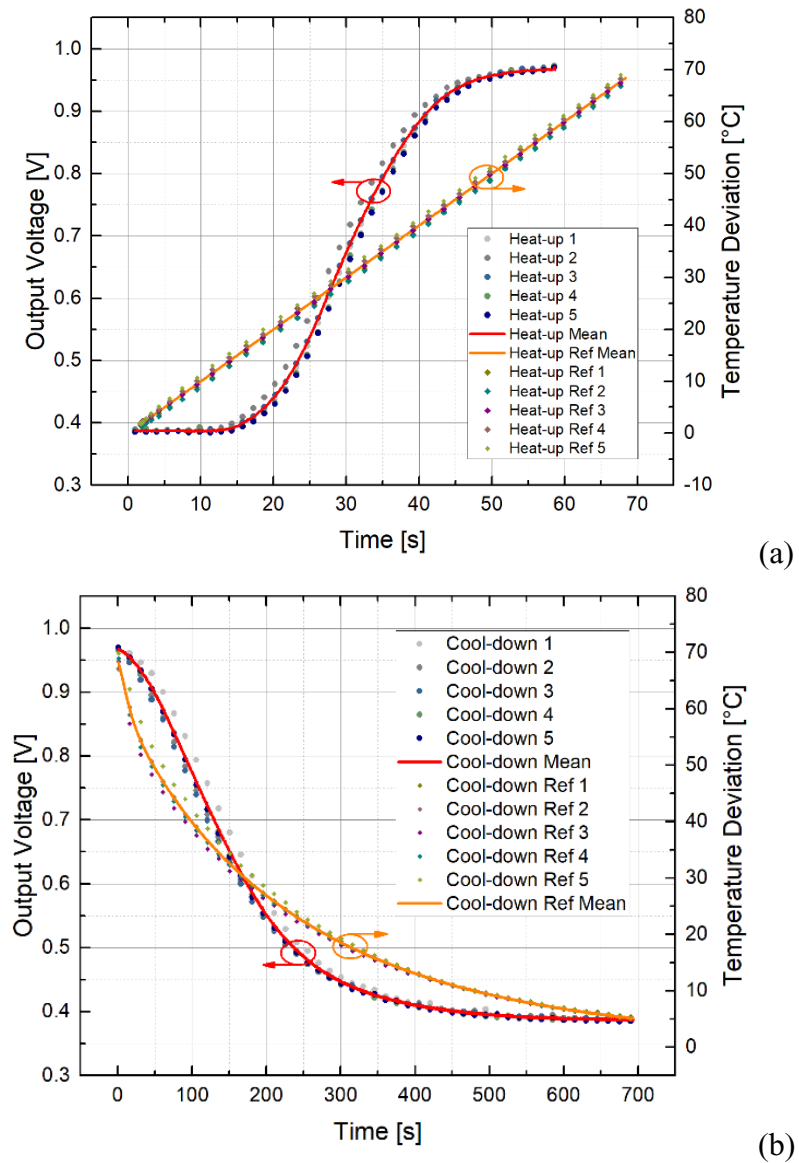
Figure 4.25: (a) heat-up measurement repeated 5 times with mean spectrum highlighted in red; (b) cool-down measurement repeated five times with mean spectrum highlighted in red.

(a)

(b)
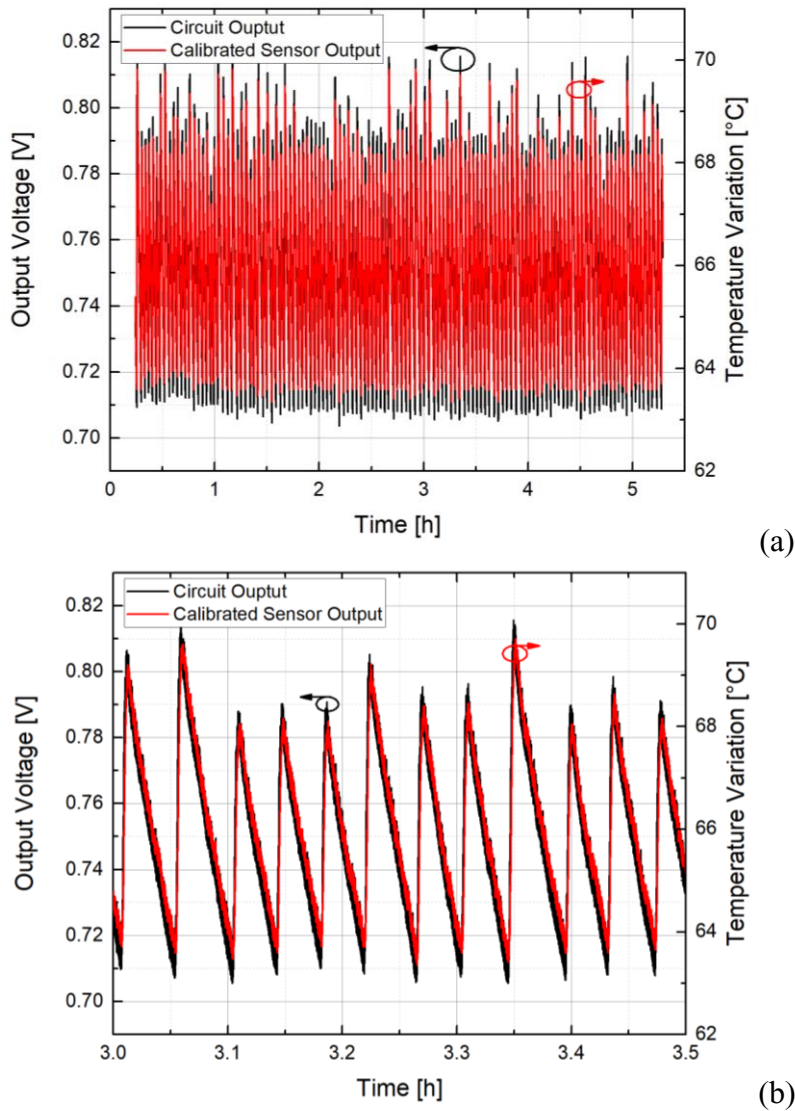
Figure 4.26: (a) over 5 hours measurement Time vs Voltage with temperature reference at a heat plate fixed temperature of 66°C, (b) magnified part.

In Figure 4.26, 5 hours and half measurement is shown: the output voltage variation is taken in comparison with the temperature reference one. The temperature variation is present since it is produced by the heat plate which was set to a temperature of 66°C. Zooming in

the middle region is possible to appreciate how the system output follows in a very optimal way the temperature variation by the calibrated sensor, highlighting the linear behavior.

4.3   Combined Measurement

As demonstrated from the previous analyses, a key point of the proposed concept is to have a modular electronic section composed by one or more Sensing Circuit with the aim to improve the dynamic range of monitoring. Whether the temperature deviation to monitor is of maximum 80°C (if the sensor calibration is 10pm/°C) can be done in a single AWG channel since the wavelength shifting is in the order of hundreds of picometer. On the other hand, for the monitoring of higher temperature variations or physical quantities based on mechanical stress which experience a wavelength shifting of few nanometers, more Sensing Circuit can be employed combining with a final adder stage, which also takes into account the impedance matching, the single output analog circuit. Due to this peculiarity, the proposed system shows the possibility to combine multiple single channel circuit coming from different FOS. As well described in literature, to perform a high accuracy strain measurement with a FBG, a compensation in temperature must be done to eliminate the contribution within the wavelength shifting given by the temperature variation. A further case is the one describing the humidity FBG sensor: it is composed by a typical FBG for temperature monitoring and another FBG with a coating highly sensitive to the humidity. In many environments in which the temperature is widely under 0°C, the presence of humidity may provoke the creation of ice, damaging the facilities or the devices working. The opportunity to have an alarm switching if the threshold humidity level overcame is absolutely needed.
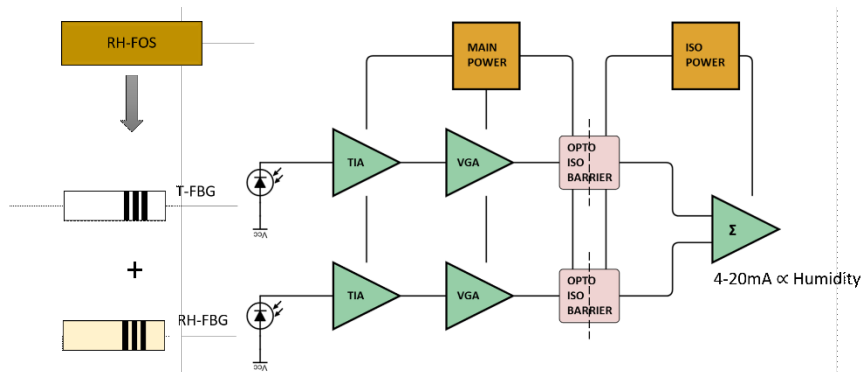
Figure 4.27: Sensing Circuit for the combined measurement of two physical quantity variations (in this case temperature and humidity) to obtain a compensated humidity measurement proportional to 4-20mA.

This can be done utilizing, as depicted in Figure 4.27, two sensing circuit in which the first one detects humidity variation, while the second one compensates from the temperature combining the two signals into the final adder stage (performing a subtraction). At the system output a 4-20mA increasing monotone signal is present proportional to the humidity level.

4.4   Common Electrical Module (CME) System

Considering a FOS system in which every sensor fabricated along the array is used to monitor the same physical quantity with the same dynamic range of measurement: this is a possible scenario in which the system is employed for the temperature monitoring in several points within a certain environment (but it is also related to every physical quantity variation in which every sensor is related to the same electronic section). In that case the electronic section related to every sensor is composed by the same number of Sensing Circuit (for simplicity let's consider one, as the case study of 1-channel measurement). Thus, a single Sensing Circuit can be used as CME for the whole array of sensors.
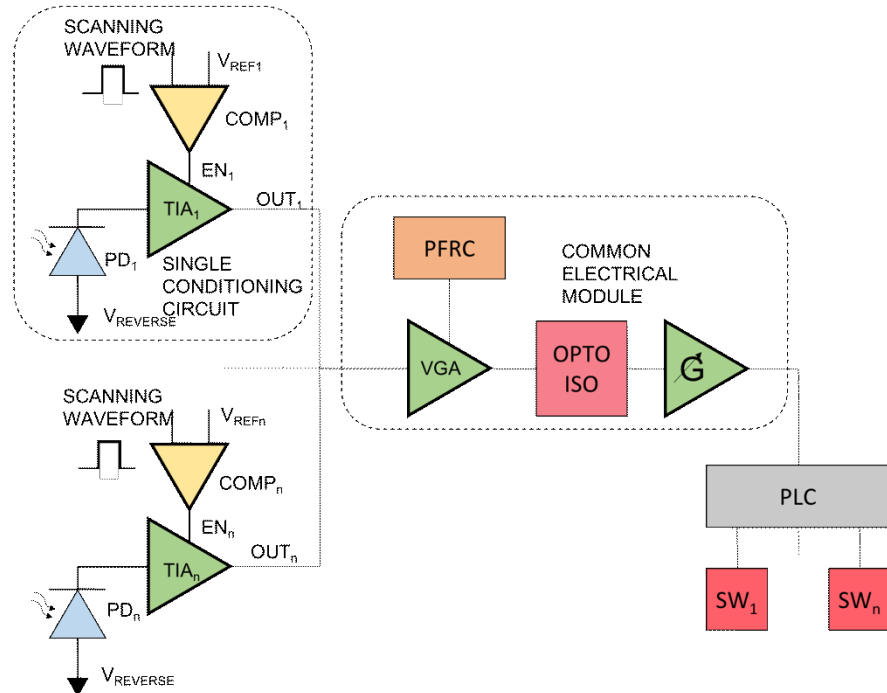
Figure 4.28: Proposed system based on a CEM in which only one electrical section is used to monitor plenty of FOSs with the same dynamic range of measurement.

The idea is illustrated in Figure 4.28 in which every FOS is related to a photodetector and to a TIA for the transduction in voltage. The TIA has to be related to the sensor for two reasons: the first is to compensate the insertion loss characterizing the AWG channel connected to the sensor which, as discussed in chapter 2, is not the same value for every channel; the second reason is to use a TIA with the enable pin (EN) to select in a certain instant which is the sensor to be monitored by PLC. Every enable pin is connected to a comparator which has in input a scanning waveform, equal for every comparator, and a reference voltage which represents the voltage level of the scanning waveform at which the relative output voltage is allowed to propagate through the CME. If, as case study, 10 FOSs are contained into a single array and the scanning waveform has a peak value of 1V (it can be whatever waveform produced with analog devices), every V_{REF} can assume a value in the range of 100mV-1V with 100mV step. The frequency characterizing the scanning waveform is the frequency of acquisition for the PLC which will refresh the acquired values at

every scanning waveform period. For temperature monitoring, a frequency of 10Hz is enough. With this technique, a considerable drop on the cost of the system can be obtained.

4.5   Pilot Project

Due to the optimal results during the experimental validation of the proposed system and the its peculiarity (the full analog conditioning circuit above all), the concept was proposed to the Technical Coordination of the at the Compact Muon Solenoid (CMS) [137] experiment to be integrated into the Detection Safety System (DSS). Is one of the two "general purpose" detectors at the Large Hadron Collider (LHC) [138] at CERN. The experiment is located in an underground cavern at LHC experimental point number five, near the French town of Cessy. The main feature of the detector is a strong super-conductive solenoidal mag- net, which can reach a 4 T field and dictates the cylindrical shape of the experiment. The magnet occupies the central region of the detector, called barrel, which is externally subdivided in 5 wheels. The wheels compose the iron yoke for the return of the magnetic fields and contain the chambers for the detection of muons. The central wheel (designated wheel 0) is also the structural support for the magnet to which it's connected. The barrel region is closed on both ends by four instrumented iron disks called endcaps. Once closed, the detector is quite compact, being a cylinder 21.6 m long and with a diameter of 14.6 m. Its total weight is of about 14500 tons. In Figure 4.29 an expanded section of the CMS detector is shown, with highlighted the main sub-detectors. The CMS operation in very complex environmental conditions re- quires a constant monitoring of temperature, structural deformation, relative humidity, magnetic field and ionizing radiation. Indeed, all the CMS experimental area is under constant monitoring. As for all the LHC experiments, the safety and the equipment protection of the CMS experimental site is guaranteed by the Detector Safety System (DSS). At the beginning of 2001, the four LHC experiments produced a working document defining requirements for a system assuring equipment protection for the valuable, and sometimes
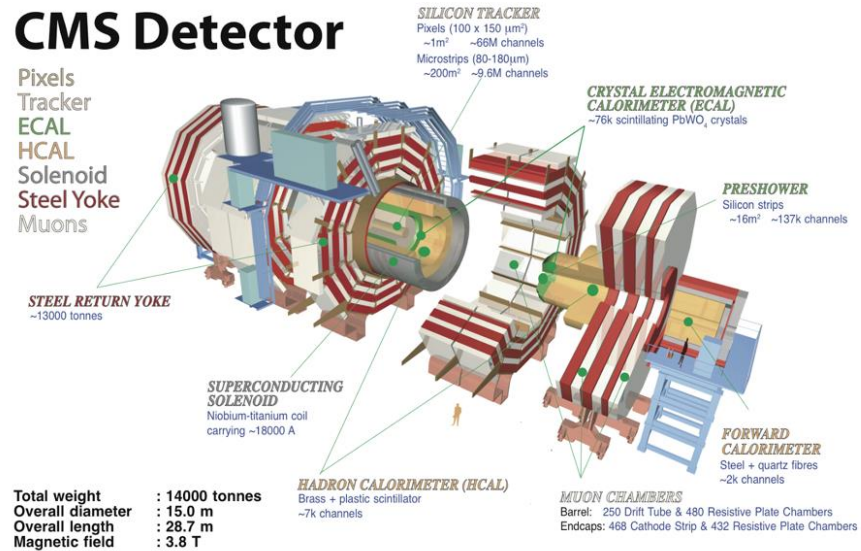
Figure 4.29: CMS schematic layout.

irreplaceable, detectors. The outcome of this is the DSS. The main goal of the DSS is to detect abnormal and potentially harmful situations, and to minimize the consequent damage to the experimental equipment by taking "protective actions". By implementing this strategy, a reduction of the occurrence of higher-level alarms with more serious consequences can be expected, and therefore an increase of the experiment's running time and efficiency. As a consequence of the above-mentioned goals, the following main requirements were defined for the DSS. It has to be, just to cite the main requirements:

- highly reliable and available, as well as simple and robust;
- provide a cost-effective solution for experimental safety;
- able to take immediate actions to protect the equipment;
- scalable, so that it may evolve with the experiments during their assembly, commissioning, operation and dismantling (a timespan of approximately 20 years);
- maintainable over the lifetime of the experiments.
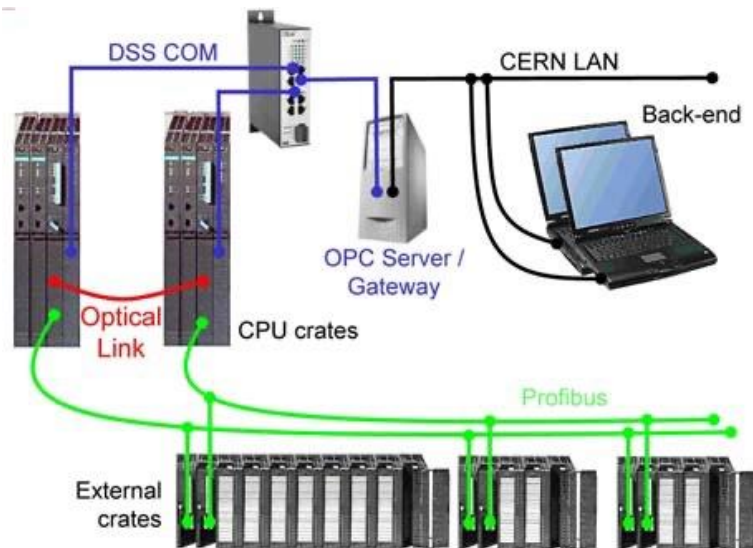
Figure 4.30: General DSS Hardware Layout [139].

The CMS DSS implementation distinguishes between a Front-end, to which the safety-critical part of the DSS task is delegated, and a Back end, which supervises the Front-end though a SCADA system. Their inter-communication is performed through a dedicated OPC6 server / gateway. The general layout for a typical experiment is shown Figure 4.30 [139]. The Front-end must be capable of running autonomously and of automatically taking predefined protective actions whenever required. Its design must be as simple and robust as possible, but at the same time highly reliable and available. The standard used for such applications in industry is "Programmable Logic Controllers" (PLCs). The DSS implementation follows this approach, using a redundant PLC system from Siemens7 which is certified for Safety Integrity Level (SIL) 2 applications. The status of the experiment's equipment is continually monitored by digital and analog sensors (e.g. PT100 for temperature measurement, humidity sensors, and status signals of sub-detectors). All values are filtered and checked. Required actions are determined automatically and immediately by the PLC and taken by DSS actuators (in this case, usually by cutting the electrical power). The sensors and actuators are dedicated to the DSS. Only hardwired sensors

Figure 4.31: a) Rack in Underground Service Cavern (USC); b) rack in Underground Experimental Cavern (UXC)

are considered to be safe, since networked information be guaranteed to be reliable. The FOS technology have been used for 10 years at CMS for the structural health monitoring of several subsection of the detector and also for the monitoring of the beryllium beam pipe [125], [140], [141] and it scored a great response, thanks to its intrinsic advantages,

substituting the electronic sensors before employed. Nowadays more than 1000 FBG sensors is used to monitor strain, temperature, humidity and electromagnetic dissipation phenomena [142].

The chance to use FOS also as DSS allows to take advantages of the well-known technology in one of the few environments left in which other kind of sensors are still considered more reliable. Since the proposed system has the task to interrogate one or more FOSs with a full analog modular conditioning circuit with a generated output signal in the range of 4-20mA ready to be acquired by a PLC, this chance can be exploited. The full analog interrogation technique was proposed at CMS for a trial arousing attention in order to propose a pilot project named FOS4DSS.

The pilot project begins in 01/02/2021 and consists in the installation of the proposed system for the interrogation of two FBG temperature sensors in one of the currently working DSS rack depicted in Figure 4.31. The aim is to demonstrate the on-field feasibility, validating the experimental results obtained with laboratory instrumentation and comparing it with the existing temperature read-out systems, without affecting them. The temperature deviation leading to the alarm switch is 40°C in respect of the room temperature of 20°C monitored with two FBG sensors within the rack glued at the positions with higher temperature sensitive. The experimental results shown in this chapter are with an FBG sensor at femtosecond technology of about 300pm FWHM which are the one already used at the CMS, hence, it is only needed to choose the right gain to match the 20mA value with the higher temperature value. Initially the system will be calibrated in a climate chamber to get the matching between current and temperature values, then a first trial will be done with a separated PLC and external bias. The second trial consists in a full integrated system, without the needs of external bias, in a box within the rack, connected to the pre-existent PLC comparing the results with the other safety systems. The target of the project is to install the proposed system as DSS of the whole CMS including also humidity and cryogenic measurements, further expanding the usage of FOS technology. It's worth to note that, from the work reported in this chapter, an Italian patent has been filed (number 102020000007243 in date 04-06-2020).

4.6   Conclusion

A purely analog fiber optic-based safety monitoring system has been designed and experimentally validated. The optical section is based on the Arrayed Waveguide Grating device which works as a passive filter with the aim to direct the output in one or more channel in function of the wavelength characterizing it. From the electrical point of view a full analog conditioning circuit produces in output a current in the range 4-20mA matching with PLC system. A full analog circuit with the capability to restore the output in case of source fluctuation or malfunction in optical devices has been designed as well. The optoelectronic system has been tested with some temperature measurement: a 50°C temperature deviation has been measured employing only one AWG channel obtaining an output spectrum which has been fitted with a 3rd degree polynomial curve, with a linear region of 20°C; a 130°C temperature deviation has been measured as well employing two AWG channels obtaining, as in the single channel case, an output with increasing monotone spectrum; a static temperature measurement has been done setting a constant value on the heat plate for over 5 hours detecting the oscillation produced by it and, to test the repeatability of the system, five times of heat-up and cool-down have been conducted obtaining a very well repetition of the measurement in which the spectrum variation is given by a systematic error produced by the heat plate (further experiment will be done in few weeks to test the long term stability in a climate chamber). Furthermore, the feasibility of the PFRC has been tested halving the SLED power and monitoring the appropriate gain signal which results doubled. The system has also the capability to improve the dynamic range of the system employing more AWG channels. In this latter version the last stage is in "adder" configuration to combine the signals coming from every conditioning stage. The output spectrum is increasing monotone and with a voltage value able to convert in current in the range of 4-20mA. With the same technique is possible to monitor physical quantity which needs more than one sensor as well. The proposed concept has been tested with a Fiber Bragg Grating as sensor test, but its functionality is not depending on the kind of optical sensor: the only constrain is given by the AWG spectrum. A pilot project with the CMS experiment at CERN has been agreed with the beginning from the 1st of

February 2021. The work consists in the monitoring of the temperature within a rack in which are contained the current safety systems. With this new kind of monitoring system, the key strength of fiber optic sensors technology can be led to that harsh environments (e.g., complex industrial infrastructures or other facilities which relies on the use of PLC monitoring system to guarantee the safety) in which digital signal processing is not allowed.

Conclusions and Future Works

The contents of this thesis regard two innovative applications of fiber optic interrogation systems based on the arrayed waveguide grating device.

The interrogation system is a fundamental element in a fiber optic measurement system since it has the aim to detect the wavelength shifting performed by the sensor. Characteristics as reliability, accuracy and resolution are key points for its design and are enhanced against the environments in which is installed.

Due to its intrinsic advantages, at the state of art many AWG-based interrogation systems have been investigated and designed: as reported in chapter 2, the AWG is a passive device working as an integrated prism, casting a polychromatic input spectrum in many monochromatic output channels due to constructive and destructive interference, making it a robust and reliable component in a compact package and with the possibility to produce it athermal (avoiding temperature dependence which may affect the output channels central wavelength). Furthermore, the AWG transmittance exhibits a Gaussian spectrum, easy to manipulate in convolution with other FOS presenting a Gaussian shape as well (FBG above all). To employ the device as optical demultiplexer and/or as optical filter, in substitution with other optical filters which needs control signal, gives the benefit to obtain an interrogation system without movable part and deprived of control signal, two features strongly limiting the measurement speed and the comprehensive reliability. Nowadays, the interrogators complexity and high cost exacerbate, in two different ways, the detection of high-speed phenomena, as well as the design of a safety monitoring system based on FOS technology. In the discussion of this thesis, the AWG has been employed as main device for the design, characterization and realization of an interrogation system for high-speed detection and a safety monitoring system for FOS technology.

- As concerns the high-speed detection interrogation system, a first theoretical approach has been conducted with the aim to manipulate the optical device spectrum and obtain a detection algorithm for wavelength measurement. With an FBG sensor

under test, the algorithm has also revealed that the Bragg wavelength is in linear dependance with the declared interrogation function which depends on the optical power of two adjacent AWG channels. The AWG bandwidth plays an important role in as much as the sensitivity is indirectly proportional. To overcome this problem, the detection algorithm exhibits a multichannel approach providing the chance to measure a Bragg wavelength shifting over more than two adjacent AWG channels. During the theoretical approach, the detection algorithm has been tested analytically with a linear Bragg wavelength shifting, to understand which parameters may affect the system accuracy: it has been demonstrated that not equal FWHM value and, more important, not first order Gaussian AWG spectrum, affects the wavelength measurements reducing the accuracy. With the purpose of simulating the optical devices with non-idealities as close as possible to the real ones, numerical simulations have been done and, on the basis of the optical power acquired, electrical simulations have been done as well to design a circuit to be realized for the experimental measurements. before to perform real measurements, the real devices have been characterized with an OSA. As result of this latter analysis, effectively, the AWG spectrum is not so close to the ideal model, inducing troubles during the wavelength detection. From a first experimental analysis, due to the bandwidth inequality and, particularly, the Gaussian spectrum closer to the second rather than the first order, a slope error has been detected exhibiting a Bragg wavelength shifting wider than the real. To mitigate the mentioned problem, the detection algorithm has been calibrated for the channel employed in such that the Bragg wavelength matches the AWG spectrum. To prove the feasibility of the interrogation system, three FBG sensors with different bandwidth have been employed for temperature monitoring among three AWG channels, obtaining an error in the sub picometer order, calculated in three points matching the central wavelength of each AWG output channel. A strain measurement has been done as well with an FBG glued on a metal sheet, hitting it with a reference load and analyzing the wavelength response with an FFT. Finally, to test the capability to detect a vibration in the order of MHz with the

ad-hoc circuitry, a measurement with an ultrasound piezoelectric probe has been managed. The probe has been biased with a rectangular pulse controlled by an FPGA, exhibiting the ultrasound vibration during the high level of the pulse. With the employment of an oscilloscope sampling at 2GSPS, the periodic vibration signal has been sensed on the FBG sensor.

- What about the safety detection system, the aim of the work has been to design a full analog electrical section in order to transduce the signal coming from the optical section of the system into a monotonic current variation in the range of 4-20mA. The circuitry is composed by a single Sensing Circuit, projected ad-hoc to convert the signal coming from the AWG output channel, propagating it towards an alarm switch or a PLC system. It is completely protected from any kind of leakage current due to an optoisolator which has also the aim to reduce noise if mounted in photovoltaic configuration. The electrical module has also the capability to restore the output if a source malfunction occurs or if a loss increment happens due to fiber bending or connector damaged. Has been proved with experimental measurement that the Sensing Circuit can be employed either alone to make a single channel measurement for the variation sensing of a physical quantity in the range of the AWG channel bandwidth or combined to other Sensing Circuit to increase the dynamic range of measurement (still exhibiting a monotonic spectrum), to make a compensated measurement merging more FOSs response to get one physical quantity matched to the 4-20mA range. It is also possible in a specific case, to use one sensing board with a TIA connected to each AWG channel compensating the different insertion loss, enabled with a periodic analog signal. The proposed concept is the core of a pilot project stipulated with the CMS experiment of the LHC located at the CERN, in Geneve since its peculiarities (robust, reliable and completely free from any digital processing section) allow it to be used as a safety monitoring system. The pilot project consists of two FBG sensors monitoring a temperature deviation of 40°C within a rack in which are contained the current safety system installed at CMS.

Thanks to the characteristics of the AWG device, it has been possible to design and validate two optoelectronic systems which can

be very competitive on the market for both high-speed detection and to be used as safety monitoring system, leading the FOS technology advantages in that few environments in which are not employed yet.

As future work, for the high-speed interrogator the aim is to integrate the whole circuitry into a PCB, connected to an ASIC (Application Specific Integrated Circuit) designed ad-hoc for the data acquisition and digital processing of the Bragg wavelength shifting under monitoring. The ASIC has to be designed with a firmware in order to select how many AWG output channels to employ for the single FBG interrogated, in order to have a modular dynamic range in function of the physical phenomena to monitor. What about the safety system explained within the chapter 4, the goal of the project is to demonstrate its feasibility into the framework of CMS in order to be used as main safety system of the whole experiment, also for the monitoring of physical phenomenon different from the temperature variation (humidity, strain, radiation and others).

Appendix

Here follows information about the AWG employed as optical filter in the solutions described in this thesis. The AWG is athermal, with 40 channel and was developed by OpLink (MOLEX). In the next table, data about central wavelength, maximum insertion loss, ripple and bandwidth (in terms of frequency) are reported.

Table 1: Information about the AWG employed.

Port	Wavelength	Max IL	Ripple	FWHM
Units	nm	dB	dB	GHz
60	1529.553	3.81	0.14	80.16
59	1530.334	3.82	0.19	80.20
58	1531.116	3.98	0.14	79.88
57	1531.898	3.92	0.19	79.99
56	1532.681	3.77	0.15	79.70
55	1533.465	3.89	0.19	79.76
54	1534.250	3.92	0.13	79.67
53	1535.036	3.84	0.19	79.67
52	1535.822	3.84	0.14	79.37
51	1536.609	3.95	0.20	79.48
50	1537.397	3.86	0.14	73.37
49	1538.186	3.82	0.18	79.29
48	1538.976	3.64	0.14	78.98
47	1539.766	3.69	0.19	79.20

46	1540.557	3.97	0.15	78.89
45	1541.349	3.73	0.18	79.16
44	1542.142	3.73	0.15	78.63
43	1542.936	3.75	0.16	79.25
42	1543.730	3.84	0.16	78.40
41	1544.526	3.71	0.16	78.86
40	1545.322	3.81	0.18	78.53
39	1546.119	3.77	0.17	79.58
38	1546.917	3.79	0.18	78.25
37	1547.715	3.93	0.17	79.34
36	1548.515	3.71	0.20	78.19
35	1549.315	3.78	0.14	79.22
34	1550.116	3.96	0.19	78.04
33	1550.918	3.94	0.14	78.96
32	1551.721	3.89	0.18	77.80
31	1552.524	3.72	0.12	79.06
30	1553.329	3.76	0.18	77.62
29	1554.134	3.77	0.15	78.73
28	1554.940	3.74	0.16	77.54
27	1555.747	3.74	0.18	78.21
26	1556.555	3.80	0.17	77.45
25	1557.363	3.80	0.20	77.92

24	1558.173	3.78	0.17	77.21
23	1558.983	3.82	0.23	77.63
22	1559.794	3.86	0.18	76.87
21	1560.606	3.84	0.20	77.40

References

[1]   R. Kashyap, "Fiber Grating Band-pass Filters," *Fiber Bragg Gratings*, pp. 227–309, 1999, doi: 10.1016/b978-012400560-0/50007-5.

[2]   J. M. L. H. Raman Kashyap, *Handbook of optical fiber sensing technology; Fiber Grating Technology: Theory, Photosensitivity, Fabrication and characterization.* 2002.

[3]   A. Othonos, "SClENTlFlC," vol. 68, no. 12, pp. 4309–4341, 1997.

[4]   K. O. Hill, Y. Fujii, D. C. Johnson, and B. S. Kawasaki, "Photosensitivity in optical fiber waveguides: Application to reflection filter fabrication," *Appl. Phys. Lett.*, vol. 32, no. 10, pp. 647–649, 1978, doi: 10.1063/1.89881.

[5]   B. S. Kawasaki, K. O. Hill, D. C. Johnson, and Y. Fujii, "Narrow-band Bragg reflectors in optical fibers," *Opt. Lett.*, vol. 3, no. 2, p. 66, 1978, doi: 10.1364/ol.3.000066.

[6]   G. Meltz, W. W. Morey, and W. H. Glenn, "Formation of Bragg gratings in optical fibers by a transverse holographic method," *Opt. Lett.*, vol. 14, no. 15, pp. 823–825, 1989, doi: 10.1364/OL.14.000823.

[7]   K. O. Hill, B. Malo, F. Bilodeau, D. C. Johnson, and J. Albert, "Bragg gratings fabricated in monomode photosensitive optical fiber by UV exposure through a phase mask," *Appl. Phys. Lett.*, vol. 62, no. 10, pp. 1035–1037, 1993, doi: 10.1063/1.108786.

[8]   K. O. Hill and G. Meltz, "Fiber Bragg grating technology fundamentals and overview," *J. Light. Technol.*, vol. 15, no. 8, pp. 1263–1276, 1997, doi: 10.1109/50.618320.

[9]   T. Erdogan, "Fiber grating spectra," *J. Light. Technol.*, vol. 15, no. 8, pp. 1277–1294, 1997, doi: 10.1109/50.618322.

[10]   D. K. W. Lam and B. K. Garside, "Characterization of single-mode optical fiber filters," *Appl. Opt.*, vol. 20, no. 3, pp. 440–445, Feb. 1981, doi: 10.1364/AO.20.000440.

[11]   R. P. Salathé, "Spectral characterisation of photoinduced high efficient Bragg gratings in standard telecommunication fibres," *Electron. Lett.*, vol. 29, no. 1, pp. 47-49(2), 1993, [Online].

Available: https://digital-library.theiet.org/content/journals/10.1049/el_19930031.

[12]   I. Bennion, J. A. R. Williams, L. Zhang, K. Sugden, and N. J. Doran, "Uv-written in-fibre Bragg gratings," *Opt. Quantum Electron.*, vol. 28, no. 2, pp. 93–135, 1996, doi: 10.1007/BF00278281.

[13]   P. S. J. Russell, J.-L. Archambault, and L. Reekie, "Fibre gratings," *Physics World*, vol. 6, no. 10. pp. 41–48, 1993, doi: 10.1088/2058-7058/6/10/25.

[14]   Y. J. Rao, "In-fibre Bragg grating sensors," *Meas. Sci. Technol.*, vol. 8, no. 4, pp. 355–375, 1997, doi: 10.1088/0957-0233/8/4/002.

[15]   Y. J. Rao and D. A. Jackson, "Recent progress in fibre optic low-coherence interferometry," *Meas. Sci. Technol.*, vol. 7, no. 7, pp. 981–999, 1996, doi: 10.1088/0957-0233/7/7/001.

[16]   A. D. Kersey *et al.*, "Fiber grating sensors," *J. Light. Technol.*, vol. 15, no. 8, pp. 1442–1462, 1997, doi: 10.1109/50.618377.

[17]   A. Bertholds and R. Dändliker, "Deterination of the Individual Strain-Optic Coefficients in Single-mode Optical Fibers," *J. Light. Technol.*, vol. 6, no. 1, pp. 17–20, 1988, doi: 10.1109/50.3956.

[18]   V. M. Murukeshan, P. Y. Chan, L. S. Ong, and A. Asundi, "Measurement in Embedded Composite Structures," vol. 40, no. 1, pp. 145–149, 2001.

[19]   S. Pal *et al.*, "Strain-independent temperature measurement using a type-l and type-IIA optical fiber Bragg grating combination," *Rev. Sci. Instrum.*, vol. 75, no. 5 PART 1, pp. 1327–1331, 2004, doi: 10.1063/1.1711155.

[20]   L. Ren, J. Chen, H. N. Li, G. Song, and X. Ji, "Design and application of a fiber Bragg grating strain sensor with enhanced sensitivity in the small-scale dam model," *Smart Mater. Struct.*, vol. 18, no. 3, pp. 3–10, 2009, doi: 10.1088/0964-1726/18/3/035015.

[21]   W. Schulz, E. Udd, J. Seim, H. Laylor, and G. McGill, "Single and multiaxis fiber grating based strain sensors for civil structure applications," *Proc. SPIE - Int. Soc. Opt. Eng.*, 1998, doi: 10.1117/12.323417.

[22]   E. Rivera and D. J. Thomson, "Accurate strain measurements

with fiber Bragg sensors and wavelength references," *Smart Mater. Struct.*, vol. 15, no. 2, pp. 325–330, 2006, doi: 10.1088/0964-1726/15/2/012.

[23] H. N. Li, D. S. Li, and G. B. Song, "Recent applications of fiber optic sensors to health monitoring in civil engineering," *Eng. Struct.*, vol. 26, no. 11, pp. 1647–1657, 2004, doi: 10.1016/j.engstruct.2004.05.018.

[24] Y.-L. Lo, Y.-C. Lin, and Y.-M. Chen, "Athermal fibre Bragg grating strain gauge with metal coating in measurement of thermal expansion coefficient," *Sensors Actuators A Phys.*, vol. 117, no. 1, pp. 103–109, 2005, doi: 10.1016/j.sna.2004.06.017.

[25] P. Moyo, J. M. W. Brownjohn, R. Suresh, and S. C. Tjin, "Development of fiber Bragg grating sensors for monitoring civil infrastructure," *Eng. Struct.*, vol. 27, no. 12 SPEC. ISS., pp. 1828–1834, 2005, doi: 10.1016/j.engstruct.2005.04.023.

[26] L. B. W. and J. P. O. X. F. Zhao, S. Z. Tian, Z. Zhou, "Experimental study on strain monitoring of concrete using a steel slice packaged fiber grating," *J. Optoelectron. Laser*, 2003.

[27] Y. Bin Lin, K. C. Chang, J. C. Chern, and L. A. Wang, "Packaging methods of fiber-Bragg grating sensors in civil structure applications," *IEEE Sens. J.*, vol. 5, no. 3, pp. 419–423, 2005, doi: 10.1109/JSEN.2005.844539.

[28] Y. Zhao and Y. Liao, "Discrimination methods and demodulation techniques for fiber Bragg grating sensors," *Opt. Lasers Eng.*, vol. 41, no. 1, pp. 1–18, 2004, doi: 10.1016/S0143-8166(02)00117-3.

[29] X. Shu *et al.*, "Fiber grating type dependence of temperature and strain coefficients and application to simultaneous temperature and strain measurement," *2002 15th Opt. Fiber Sensors Conf. Tech. Dig. OFS 2002*, vol. 27, no. 9, pp. 83–86, 2002, doi: 10.1109/OFS.2002.1000507.

[30] W. C. Du, "Fiber bragg grating cavity sensor for simultaneous measurement of strain and temperature," *IEEE Photonics Technol. Lett.*, vol. 11, no. 1, pp. 105–107, 1999, doi: 10.1109/68.736409.

[31] S. Kim, J. Kwon, S. Kim, and B. Lee, "Temperature-independent strain sensor using a chirped grating partially embedded in a glass tube," *IEEE Photonics Technol. Lett.*, vol. 12, no. 6, pp.

678–680, 2000, doi: 10.1109/68.849082.

[32]   M. G. Xu, L. Dong, L. Reekie, J. A. Tucknott, and J. L. Cruz, "Temperature-independent strain sensor using a chirped Bragg grating in a tapered optical fibre," *Electron. Lett.*, vol. 31, no. 10, pp. 823–825, 1995, doi: 10.1049/el:19950542.

[33]   S. E. Kanellopoulos, V. A. Handerek, and A. J. Rogers, "Simultaneous strain and temperature sensing with photogenerated in-fiber gratings," *Opt. Lett.*, vol. 20, no. 3, p. 333, 1995, doi: 10.1364/ol.20.000333.

[34]   Y.-J. Chiang, L. Wang, H.-S. Chen, C.-C. Yang, and W.-F. Liu, "Multipoint temperature-independent fiber-Bragg-grating strain-sensing system employing an optical-power-detection scheme," *Appl. Opt.*, vol. 41, no. 9, p. 1661, 2002, doi: 10.1364/ao.41.001661.

[35]   M. G. Xu, J. L. Archambault, L. Reekie, and J. P. Dakin, "Discrimination between strain and temperature effects using dual-wavelength fibre grating sensors," *Electron. Lett.*, vol. 30, no. 13, pp. 1085–1087, 1994, doi: 10.1049/el:19940746.

[36]   S. W. James, M. L. Dockney, and R. P. Tatam, "Simultaneous independent temperature and strain measurement using in-f ibre Bragg grating sensors," *Electron. Lett.*, vol. 32, no. 12, pp. 1133–1134, 1996, doi: 10.1049/el:19960732.

[37]   M. Song, B. Lee, S. B. Lee, and S. S. Choi, "Interferometric temperature-insensitive strain measurement with different-diameter fiber Bragg gratings," *Opt. Lett.*, vol. 22, no. 11, p. 790, 1997, doi: 10.1364/ol.22.000790.

[38]   J. L. S. and F. F. L. A. Ferreira, F. M. Araujo, *No TitleSimultaneous measurement of strain and temperature using interferometrically interrogated fiber Bragg grating sensors*. 2000.

[39]   J. Jung, H. Nam, J. H. Lee, N. Park, and B. Lee, "Simultaneous measurement of strain and temperature using a single fiber Bragg grating with erbium-doped fiber amplifier," *Conf. Proc. - Lasers Electro-Optics Soc. Annu. Meet.*, vol. 1, no. 13, pp. 403–404, 1998, doi: 10.1109/leos.1998.737900.

[40]   D. I. Forsyth, S. A. Wade, T. Sun, X. Chen, and K. T. V. Grattan, "Dual temperature and strain measurement with the combined fluorescence lifetime and Bragg wavelength shift approach in

doped optical fiber," *Appl. Opt.*, vol. 41, no. 31, p. 6585, 2002, doi: 10.1364/ao.41.006585.

[41]   M. N. Alahbabi, Y. T. Cho, and T. P. Newson, "Long-range distributed temperature and strain optical fibre sensor based on the coherent detection of spontaneous Brillouin scattering with in-line Raman amplification," *Meas. Sci. Technol.*, vol. 17, no. 5, pp. 1082–1090, 2006, doi: 10.1088/0957-0233/17/5/S24.

[42]   P. Lu, L. Men, and Q. Chen, "Resolving cross sensitivity of fiber Bragg gratings with different polymeric coatings," *Appl. Phys. Lett.*, vol. 92, no. 17, pp. 2006–2009, 2008, doi: 10.1063/1.2919796.

[43]   M. M. Werneck, B. A. R. R. C. S. B. Allil, and F. V. B. Nazaré, "A Guide to Fiber Bragg Grating Sensors," 2013.

[44]   A. Iadicicco, A. Cusano, S. Campopiano, A. Cutolo, and M. Giordano, "Thinned fiber Bragg gratings as refractive index sensors," *IEEE Sens. J.*, vol. 5, no. 6, pp. 1288–1294, 2005, doi: 10.1109/JSEN.2005.859288.

[45]   A. N. Chryssis, S. M. Lee, S. B. Lee, S. S. Saini, and M. Dagenais, "High sensitivity evanescent field fiber Bragg grating sensor," *IEEE Photonics Technol. Lett.*, vol. 17, no. 6, pp. 1253–1255, 2005, doi: 10.1109/LPT.2005.846953.

[46]   A. Cusano, A. Iadicicco, S. Campopiano, M. Giordano, and A. Cutolo, "Thinned and micro-structured fibre Bragg gratings: Towards new all-fibre high-sensitivity chemical sensors," *J. Opt. A Pure Appl. Opt.*, vol. 7, no. 12, pp. 734–741, 2005, doi: 10.1088/1464-4258/7/12/005.

[47]   A. Iadicicco, S. Campopiano, A. Cutolo, M. Giordano, and A. Cusano, "Self temperature referenced refractive index sensor by non-uniform thinned fiber Bragg gratings," *Sensors Actuators, B Chem.*, vol. 120, no. 1, pp. 231–237, 2006, doi: 10.1016/j.snb.2006.02.027.

[48]   X. F. Huang *et al.*, "Design and characteristics of refractive index sensor based on thinned and microstructure fiber Bragg grating," *Appl. Opt.*, vol. 47, no. 4, pp. 504–511, 2008, doi: 10.1364/AO.47.000504.

[49]   G. Tsigaridas, D. Polyzos, A. Ioannou, M. Fakis, and P. Persephonis, "Theoretical and experimental study of refractive index sensors based on etched fiber Bragg gratings," *Sensors*

Actuators, A Phys., vol. 209, pp. 9–15, 2014, doi: 10.1016/j.sna.2014.01.007.

[50] G. Ryu, M. Dagenais, M. T. Hurley, and P. DeShong, "High specificity binding of lectins to carbohydrate-functionalized fiber bragg gratings: A new model for biosensing applications," *IEEE J. Sel. Top. Quantum Electron.*, vol. 16, no. 3, pp. 647–653, 2010, doi: 10.1109/JSTQE.2009.2032427.

[51] A. Asseh, S. Sandgren, H. Åhlfeldt, B. Sahlgren, and R. Stubbe, "Fiber optical bragg grating refractometer," *Fiber Integr. Opt.*, vol. 17, no. 1, pp. 51–62, 1998, doi: 10.1080/014680398245055.

[52] A. Gusarov and S. K. Hoeffgen, "Radiation effects on fiber gratings," *IEEE Trans. Nucl. Sci.*, vol. 60, no. 3, pp. 2037–2053, 2013, doi: 10.1109/TNS.2013.2252366.

[53] A. Gusarov *et al.*, "Comparative study of the MGy dose level γ-radiation effect on FBGs written in different fibres," *Proc. SPIE - Int. Soc. Opt. Eng.*, vol. 1993740004, pp. 1–21386, 2AD.

[54] D. Grobnic, H. Henschel, S. Hoeffgen, J. Kuhnhenn, S. Mihailov, and U. Weinand, "Radiation sensitivity of Bragg gratings written with femtosecond IR lasers," *Fraunhofer INT*, vol. 7316, 2009, doi: 10.1117/12.818157.

[55] A. Morana, "Gamma-rays and neutrons effects on optical fibers and Bragg gratings for temperature sensors," Université Jean Monnet - Saint-Etienne ; Università degli studi di Palermo (Palerme, Italie), 2013.

[56] H. Henschel, S. K. Hoeffgen, K. Krebber, J. Kuhnhenn, and U. Weinand, "Influence of fiber composition and grating fabrication on the radiation sensitivity of fiber bragg gratings," *Proc. Eur. Conf. Radiat. its Eff. Components Syst. RADECS*, pp. 0–5, 2007, doi: 10.1109/RADECS.2007.5205461.

[57] V. B. Neustruev *et al.*, "Ultraviolet radiation- and γ radiation-induced color centers in germanium-doped silica glass and fibers," *Fiber Integr. Opt.*, vol. 8, no. 2, pp. 143–156, 1989, doi: 10.1080/01468038908202872.

[58] F. Berghmans *et al.*, "Radiation hardness of fiber-optic sensors for monitoring and remote handling applications in nuclear environments," *Photonics East*, vol. 3538, 1998, doi: 10.1117/12.335757.

[59] A. Gusarov, B. Brichard, and D. N. Nikogosyan, "Gamma-

radiation effects on Bragg gratings written by femtosecond UV laser in Ge-doped fibers," *IEEE Trans. Nucl. Sci.*, vol. 57, no. 4 PART 1, pp. 2024–2028, 2010, doi: 10.1109/TNS.2009.2039494.

[60] H. Henschel, S. K. Hoeffgen, J. Kuhnhenn, and U. Weinand, "Influence of manufacturing parameters and temperature on the radiation sensitivity of fiber Bragg gratings," *Proc. Eur. Conf. Radiat. its Eff. Components Syst. RADECS*, vol. 57, no. 4, pp. 382–387, 2009, doi: 10.1109/RADECS.2009.5994682.

[61] M. Song, S. Yin, and P. B. Ruffin, "Fiber Bragg grating strain sensor demodulation with quadrature sampling of a Mach–Zehnder interferometer," *Appl. Opt.*, vol. 39, no. 7, p. 1106, 2000, doi: 10.1364/ao.39.001106.

[62] J. Alves, J. L. Santos, A. Carvalho, and A. Lage, "Fiber Bragg Sensor Interrogation System Based on a CCD Spectrometer," *Proc. IEEE Sensors*, vol. 2, no. 2, pp. 909–913, 2003, doi: 10.1109/icsens.2003.1279075.

[63] K. Liu, S. Karr, T. Coroy, and R. M. Measure, "A Bragg Grating-Tuned Fiber Laser Strain Sensor System," *IEEE Photonics Technol. Lett.*, vol. 5, no. 2, pp. 263–266, 1993, doi: 10.1109/68.196025.

[64] Bayspec, "Bayspec FBGA." http://www.bayspec.com/telecom-fiber-sensing/fbgasystems/.

[65] Ibsens Photonic, "Ibsen Photonics. Interrogation Monitors.," [Online]. Available: http://www.ibsenphotonics.com.

[66] D. Tosi, M. Olivero, G. Perrone, and A. Vallan, "Improved Fibre Bragg Grating Interrogation for Dynamic Strain Measurement Daniele Tosi, Massimo Olivero, Guido Perrone, Alberto Vallan," no. January 2014, 2009.

[67] M. A. Davis, D. G. Bellemore, T. A. Berkoff, and A. D. Kersey, "Design and performance of a fiber Bragg grating distributed strain sensor system," in *Smart Structures and Materials 1995: Smart Systems for Bridges, Structures, and Highways*, 1995, vol. 2446, pp. 227–235, doi: 10.1117/12.207731.

[68] C. G. Askins et al., "Instrumentation for interrogating many-element fiber Bragg grating arrays embedded in fiber/resin composites," in *PIE Smart Sensing, Processing and Instrumentation,* 1995, p. vol. 2444, 257.

[69]   Electronicsonline,   "No   Title."
        https://www.electronicsonline.net.au/content/sensors/article/fun
        damentals-of-fbg-optical-sensing-662156261#axzz6jYthyVyS.

[70]   M. O. R Hui, *Fiber optic measurement techniques*. 2009.

[71]   J. B. M.-C. A. D. J. Blumenthal, *Tunable Laser Diodes and
        Related Optical Sources*. SPIE PRESS BOOK, 1998.

[72]   Ignis   Inc,   "No   Title."   http://http//ignis.com/
        products/tuneablelasers/%0As7500.

[73]   C. Maccone, "Advantages of Karhunen–Loève transform over
        fast Fourier transform for planetary radar and space debris
        detection," *Acta Astronaut.*, vol. 60, pp. 775–779, 2007, doi:
        10.1016/j.actaastro.2006.08.015.

[74]   C. Maccone, *Telecommunications, KLT and relativity*. Colorado
        Springs, CO : IPI Press, 1994. - 238 p.

[75]   D. Tosi, "Advanced interrogation of fiber-optic bragg grating
        and   fabry-perot   sensors   with   KLT   analysis," *Sensors
        (Switzerland)*, vol. 15, no. 11, pp. 27470–27492, 2015, doi:
        10.3390/s151127470.

[76]   E. Letters and D. Version, "New focusing and dispersive planar
        component based on an," vol. 24, no. 1988, pp. 385–386, 2021.

[77]   H. Takahashi, S. Suzuki, K. Kato, and I. Nishi, "Arrayed-
        waveguide grating for wavelength division multi/demultiplexer
        with nanometre resolution," *Electron. Lett.*, vol. 26, no. 2, pp.
        87–88, 1990.

[78]   C. Dragone, "An N* N optical multiplexer using a planar
        arrangement of two star couplers," *IEEE Photonics Technol.
        Lett.*, vol. 3, no. 9, pp. 812–815, 1991.

[79]   J. T. Ahn, S. Park, J. Y. Do, J. Lee, M. Lee, and K. H. Kim,
        "Polymer   Wavelength   Channel   Selector   Composed   of
        Electrooptic Polymer Switch Array and Two Polymer Arrayed
        Waveguide Gratings," vol. 16, no. 6, pp. 1567–1569, 2004.

[80]   H. Okayama and M. Kawahara, "Waveguide array grating
        wavelength demultiplexer on LiNbO3," in *Integrated Photonics
        Research*, 1995, p. ISaB3.

[81]   C. van Dam, "InP-based polarisation independent wavelength
        demultiplexers," 1997.

[82]   D. Version, *Arrayed waveguide gratings*. 2006.

[83]   M. K. Smit, A. Member, and C. Van Dam, "PHASAR-Based

WDM-Devices :," vol. 2, no. 2, pp. 236–250, 1996.

[84] A. Klekamp and R. Munzner, "Calculation of imaging errors of AWG," *J. Light. Technol.*, vol. 21, no. 9, pp. 1978–1986, 2003.

[85] E. Letters and D. Version, "Phased-array wavelength demultiplexer with flattened wavelength response," no. 1994, 2019.

[86] M. R. Amersfoort, J. B. D. Soole, H. P. LeBlanc, N. C. Andreadakis, A. Rajhel, and C. Caneau, "Passband broadening of integrated arrayed waveguide filters using multimode interference couplers," *Electron. Lett.*, vol. 32, no. 5, pp. 449–451, 1996.

[87] C. Dragone, "Frequency routing device having a wide and substantially flat passband." Google Patents, 1995.

[88] K. Okamoto and A. Sugita, "Flat spectral response arrayed-waveguide grating multiplexer with parabolic waveguide horns," *Electron. Lett.*, vol. 32, no. 18, pp. 1661–1662, 1996.

[89] K. Okamoto and H. Yamada, "Arrayed-waveguide grating multiplexer with flat spectral response," *Opt. Lett.*, vol. 20, no. 1, pp. 43–45, 1995, doi: 10.1364/OL.20.000043.

[90] C. Dragone, "Efficient techniques for widening the passband of a wavelength router," *J. Light. Technol.*, vol. 16, no. 10, p. 1895, 1998.

[91] A. Rigny, A. Bruno, and H. Sik, "Multigrating method for flattened spectral response wavelength multi/demultiplexer," *Electron. Lett.*, vol. 33, no. 20, pp. 1701–1702, 1997.

[92] J.-J. He, E. S. Koteles, and B. Humphreys, "Passband flattening in waveguide grating devices using phase-dithering," in *Integrated Photonics Research*, 2002, p. IFE2.

[93] G. H. B. Thompson, R. Epworth, C. Rogers, S. Day, and S. Ojha, "An original low-loss and pass-band flattened SiO2 on Si planar wavelength demultiplexer," in *Optical Fiber Communication Conference*, 1998, p. TuN1.

[94] C. R. Doerr, L. W. Stulz, and R. Pafchek, "Compact and low-loss integrated box-like passband multiplexer," *IEEE Photonics Technol. Lett.*, vol. 15, no. 7, pp. 918–920, 2003.

[95] H. Takahashi, K. Oda, H. Toba, and Y. Inoue, "Transmission characteristics of arrayed waveguide N x N wavelength multiplexer," *SPIE MILESTONE Ser. MS*, vol. 125, pp. 352–

360, 1996.

[96] K. Maru *et al.*, "Super-high-/spl Delta/athermal arrayed waveguide grating with resin-filled trenches in slab region," *Electron. Lett.*, vol. 40, no. 6, pp. 374–375, 2004.

[97] Y. Inoue, A. Kaneko, F. Hanawa, H. Takahashi, K. Hattori, and S. Sumida, "Athermal silica-based arrayed-waveguide grating multiplexer," *Electron. Lett.*, vol. 33, no. 23, pp. 1945–1947, 1997.

[98] A. Kaneko, S. Kamei, Y. Inoue, H. Takahashi, and A. Sugita, "Athermal silica-based arrayed-waveguide grating (AWG) multi/demultiplexers with new low loss groove design," *Electron. Lett.*, vol. 36, no. 4, pp. 318–319, 2000.

[99] D. Kim *et al.*, "Suppression of temperature and polarization dependence by polymer overcladding in silica-based AWG multiplexer," in *Optical Fiber Communication Conference*, 2003, p. MF50.

[100] G. Heise, H. W. Schneider, and P. C. Clemens, "Optical phased array filter module with passively compensated temperature dependence," in *24th European Conference on Optical Communication. ECOC'98 (IEEE Cat. No. 98TH8398)*, 1998, vol. 1, pp. 319–320.

[101] T. Saito, K. Nara, Y. Nekado, J. Hasegawa, and K. Kashihara, "100GHz-32ch athermal AWG with extremely low temperature dependency of center wavelength," in *Optical Fiber Communication Conference*, 2003, p. MF47.

[102] P. Niewczas *et al.*, "Interrogation of extrinsic Fabry-Perot interferometric sensors using arrayed waveguide grating devices," *Conf. Rec. - IEEE Instrum. Meas. Technol. Conf.*, vol. 2, no. May, pp. 1677–1681, 2002, doi: 10.1109/IMTC.2002.1007212.

[103] H. Guo, L. Shao, G. Xiao, N. Mrad, and J. Yao, "Wavelength interrogation of a tilted fiber Bragg grating sensor using space-to-wavelength mapping of an arrayed waveguide grating with closed-loop piezo-electrical control," *Proc. IEEE Sensors*, pp. 1152–1155, 2010, doi: 10.1109/ICSENS.2010.5690698.

[104] H. Guo, G. Xiao, N. Mrad, J. Albert, and J. Yao, "Wavelength interrogator based on closed-loop piezo-electrically scanned space-to-wavelength mapping of an arrayed waveguide grating,"

J. Light. Technol., vol. 28, no. 18, pp. 2654–2659, 2010, doi: 10.1109/JLT.2010.2056914.

[105] W. Wu and X. Liu, "Fiber bragg grating sensors interrogation system using arrayed waveguide gratings demultiplexer," *2009 Asia Commun. Photonics Conf. Exhib. ACP 2009*, vol. 7630, pp. 1–6, 2009, doi: 10.1117/12.850692.

[106] Y. Sano and T. Yoshino, "Fast optical wavelength interrogator employing arrayed waveguide grating for distributed fiber Bragg grating sensors," *J. Light. Technol.*, vol. 21, no. 1, pp. 132–139, 2003, doi: 10.1109/JLT.2003.808620.

[107] H. Su and X. G. Huang, "A novel fiber Bragg grating interrogating sensor system based on AWG demultiplexing," *Opt. Commun.*, vol. 275, no. 1, pp. 196–200, 2007, doi: 10.1016/j.optcom.2007.02.063.

[108] Z. Liu and J. Li, "Wavelength interrogator based on arrayed waveguide gratings," *CAR 2010 - 2010 2nd Int. Asia Conf. Informatics Control. Autom. Robot.*, vol. 3, pp. 335–338, 2010, doi: 10.1109/CAR.2010.5456701.

[109] G. Fusiek, P. Niewczas, A. J. Willshire, and J. R. McDonald, "Nonlinearity compensation of the fiber Bragg grating interrogation system based on an arrayed waveguide grating," *IEEE Trans. Instrum. Meas.*, vol. 57, no. 11, pp. 2528–2531, 2008, doi: 10.1109/TIM.2008.924899.

[110] V. R. Marrazzo, M. Riccio, L. Maresca, A. Irace, and G. Breglio, "Wide Range AWG-Based FBG Interrogation System With Improved Sensitivity," in *PRIME 2019 - 15th Conference on Ph.D. Research in Microelectronics and Electronics, Proceedings*, 2019, pp. 149–152, doi: 10.1109/PRIME.2019.8787793.

[111] V. R. Marrazzo, F. Fienga, M. Riccio, L. Maresca, A. Irace, and G. Breglio, "Simulation of an Optical-to-Digital Converter for High Frequency FBG Interrogator," *Lect. Notes Electr. Eng.*, vol. 627, pp. 259–265, 2020, doi: 10.1007/978-3-030-37277-4_30.

[112] P. Niewczas, A. J. Willshire, L. Dziuda, and J. R. McDonald, "Performance analysis of the fiber Bragg grating interrogation system based on an arrayed waveguide grating," *IEEE Trans. Instrum. Meas.*, vol. 53, no. 4, pp. 1192–1196, 2004, doi:

10.1109/TIM.2004.830780.

[113] A. J. Willshire, P. Niewczas, and J. R. Mcdonald, "A cyclic arrayed-waveguide-grating-based fiber-optic sensor interrogation system," *IEEE Photonics Technol. Lett.*, vol. 18, no. 18, pp. 1904–1906, 2006, doi: 10.1109/LPT.2006.881651.

[114] T. Libish, "Fiber Gratings : Basic Theory and Sensing Principle," *Fiber Gratings*, pp. 21–79, 2015.

[115] K. Loupos and A. Amditis, "Structural health monitoring fiber optic sensors," *Smart Sensors, Meas. Instrum.*, vol. 21, no. 4, pp. 185–206, 2017, doi: 10.1007/978-3-319-42625-9_9.

[116] K. Bremer *et al.*, "Fibre Optic Sensors for the Structural Health Monitoring of Building Structures," *Procedia Technol.*, vol. 26, pp. 524–529, 2016, doi: 10.1016/j.protcy.2016.08.065.

[117] J. M. López-Higuera, "Fiber optics in structural health monitoring," *2010 Conf. Opt. Fiber Commun. Collocated Natl. Fiber Opt. Eng. Conf. OFC/NFOEC 2010*, no. May 2014, 2010, doi: 10.1117/12.876192.

[118] H. Murayama, D. Wada, and H. Igawa, "Structural health monitoring by using fiber-optic distributed strain sensors with high spatial resolution," *Photonic Sensors*, vol. 3, no. 4, pp. 355–376, 2013, doi: 10.1007/s13320-013-0140-5.

[119] M. Selvaggio *et al.*, "The MUSHA underactuated hand for robot-aided minimally invasive surgery," *Int. J. Med. Robot. Comput. Assist. Surg.*, vol. 15, no. 3, 2019, doi: 10.1002/rcs.1981.

[120] M. Consales *et al.*, "Fiber optic humidity sensors for high-energy physics applications at CERN," *Sensors Actuators, B Chem.*, vol. 159, no. 1, pp. 66–74, 2011, doi: 10.1016/j.snb.2011.06.042.

[121] A. Makovec *et al.*, "Radiation hard polyimide-coated FBG optical sensors for relative humidity monitoring in the CMS experiment at CERN," *J. Instrum.*, vol. 9, no. 3, 2014, doi: 10.1088/1748-0221/9/03/C03040.

[122] A. Chiuchiolo *et al.*, "Cryogenic test facility instrumentation with fiber optic and fiber optic sensors for testing superconducting accelerator magnets," *IOP Conf. Ser. Mater. Sci. Eng.*, vol. 278, no. 1, 2017, doi: 10.1088/1757-899X/278/1/012082.

[123] F. Fienga *et al.*, "A fiber optic sensors monitoring system for the central beam pipe of the CMS experiment," *Opt. Laser Technol.*,

vol. 120, no. June, p. 105650, 2019, doi: 10.1016/j.optlastec.2019.105650.

[124] F. Fienga *et al.*, "Fiber optic sensors structural monitoring of the beam pipe in the CMS experiment at the CERN," *IET Conf. Publ.*, vol. 2015, no. CP667, pp. 6–9, 2015, doi: 10.1049/cp.2015.0153.

[125] F. Fienga *et al.*, "Fibre optic sensors structural health monitoring of the central beam pipe in the CMS experiment at the CERN laboratories," *8th Eur. Work. Struct. Heal. Monit. EWSHM 2016*, vol. 2, no. July, pp. 1018–1025, 2016.

[126] D. Tosi, "Improved KLT Algorithm for High-Precision Wavelength Tracking of Optical Fiber Bragg Grating Sensors," *J. Sensors*, vol. 2017, 2017, doi: 10.1155/2017/5412825.

[127] M. D. Todd, G. A. Johnson, and B. L. Althouse, "A novel Bragg grating sensor interrogation system utilizing a scanning filter, a Mach-Zehnder interferometer and a 3 x 3 coupler," *Meas. Sci. Technol.*, vol. 12, no. 7, pp. 771–777, 2001, doi: 10.1088/0957-0233/12/7/303.

[128] M. Perry, P. Orr, P. Niewczas, and M. Johnston, "High-Speed Interferometric FBG Interrogator Measurement Capability," *J. Light. Technol.*, vol. 31, no. 17, pp. 2897–2903, 2013.

[129] P. Tsai, F. Sun, G. Xiao, Z. Zhang, S. Rahimi, and D. Ban, "A new fiber-bragg-grating sensor interrogation system deploying free-spectral-range-matching scheme with high precision and fast detection rate," *IEEE Photonics Technol. Lett.*, vol. 20, no. 4, pp. 300–302, 2008, doi: 10.1109/LPT.2007.915638.

[130] V. Marrazzo, F. Fienga, M. Riccio, L. Maresca, A. Irace, and G. Breglio, "Simulation of an Optical-to-Digital Converter for High Frequency FBG Interrogator," 2020, pp. 259–265.

[131] V. R. Marrazzo, M. Riccio, L. Maresca, A. Irace, and G. Breglio, "Wide Range AWG-Based FBG Interrogation System With Improved Sensitivity," *2019 15th Conf. Ph.D Res. Microelectron. Electron.*, pp. 149–152, 2019, doi: 10.1109/PRIME.2019.8787793.

[132] G. Allwood, G. Wild, and S. Hinckley, "Fiber Bragg Grating Sensors for Mainstream Industrial Processes," *Electronics*, vol. 6, p. 92, 2017, doi: 10.3390/electronics6040092.

[133] G. Allwood, G. Wild, and S. Hinckley, "Universal Signal

Conditioning Technique for Fiber Bragg Grating Sensors in PLC and SCADA Applications," *Instruments*, vol. 1, p. 7, 2017, doi: 10.3390/instruments1010007.

[134] C. Zhou, L. Chen, D. Jiang, J. He, and Z. Shaoyun, "Research and application of highway tunnel fire alarm system based on fiber Bragg grating sensor technology," *Proc. SPIE - Int. Soc. Opt. Eng.*, 2007, doi: 10.1117/12.725901.

[135] Q. Jiang, Y.-J. Rao, and D.-H. Zeng, "A fiber-optical intrusion alarm system based on quasi-distributed fiber Bragg grating sensors," in *2008 1st Asia-Pacific Optical Fiber Sensors Conference, APOS 2008*, 2008, pp. 1–5, doi: 10.1109/APOS.2008.5226300.

[136] Datenblatt, "IL300 linear optocoupler," no. 83622, pp. 1–15.

[137] CMS Collaborations, "The CMS experiment at the CERN LHC," *Search Higgs Boson C.*, vol. 08004, pp. 15–58, 2013, doi: 10.1007/978-88-7642-482-3_2.

[138] L. Evans and P. Bryant, "LHC Machine," *J. Instrum.*, vol. 3, no. 8, 2008, doi: 10.1088/1748-0221/3/08/S08001.

[139] S. M. Schmeling, B. Flockhart, S. Luders, and G. Morpurgo, "The detector safety system for LHC experiments," *IEEE Trans. Nucl. Sci.*, vol. 51, no. 3, pp. 521–525, 2004, doi: 10.1109/TNS.2004.828631.

[140] S. Buontempo *et al.*, "SHM in CMS Underground Detector at CERN using FBG Sensors," 2017, doi: 10.12783/shm2017/14163.

[141] F. Fienga, "Innovative application of fiber optic sensors in high energy physics experiments," no. May, 2017.

[142] F. Fienga *et al.*, "Fiber Bragg Grating Sensors as innovative monitoring tool for Beam Induced RF Heating on LHC Beam Pipe," *J. Light. Technol.*, vol. under revi, pp. 1–6, 2021.